THE UNIVERSITY of EDINBURGH

Title	Computational models of developing neural systems
Author	Hely, Timothy Alasdair
Qualification	PhD
Year	1999

Computational Models of Developing Neural Systems

Timothy Alasdair Hely

Ph.D.
University of Edinburgh
1999

Declaration

I declare that this thesis has been composed by myself, and that the work is my own original research except where otherwise indicated.

Tim Hely
30th April 1999

Acknowledgements

I would like to thank everyone who has helped me during the course of the Ph.D. In particular my primary supervisor David Willshaw for help throughout the 3 years. I would also like to thank my second supervisor David Price in Physiology for his interest in the work. The thesis benefitted greatly from numerous helpful discussions with Arjen van Ooyen. I am also grateful to Bruce Graham for useful comments especially with reference to the dendritic branching model. I am especially indebted to the excellent computer support at the Centre for Neural Systems. In particular to Andrew Gillies, who also provided the LaTex style file for this thesis. I would also like to thank everyone at the Centre for Neural Systems with whom I have had many interesting discussions during my Ph.D.

Above all I would like to thank my wife Ishbel MacPherson, for providing continuous motivation, love, support and especially timekeeping ability.

This work was made possible through a Wellcome Trust Mathematical Biology studentship.

Publications

Material included in this thesis can also be found in the following publications.

Hely, T.A. & Willshaw, D.J. (1998) Short term interactions between microtubules and actin filaments underlie long term behaviour in neuronal growth cones. *Proceedings of the Royal Society of London Biological Sciences.* In Press.

Hely, T.A., van Ooyen, A. & Willshaw, D.J. (1998). A simulation of growth cone filopodia patterns based on Turing morphogenesis patterns. In *Information Processing in Cells and Tissues*. Pages 69-73. Editors: Holcombe and Paton. Plenum Press, New York and London.

Graham, B., Hely, T.A. & van Ooyen, A. (1998). An internal signalling model of the dendritic branching process. *European Journal of Neuroscience*, 10S. p274.

Abstract

The work of this thesis has focused on creating computational models of developing neurons. Three different but related areas of research have been studied - how cells make connections, what influences the shape of these connections and how neuronal network behaviour can be influenced by local interactions.

In order to understand how cells make connections I simulated the dynamics of the neuronal growth cone - a structure which guides the developing axon to its target cells. Results from the first models showed that small interaction effects between structural proteins in the axon called microtubules can significantly alter the rate of axonal elongation and turning. I also simulated the dynamics of growth cone filopodia. The filopodia act as antennae and explore the extracellular environment surrounding the growth cone. This model showed that a reaction-diffusion system based on Turing morphogenesis patterns could account for the dynamic behaviour of filopodia.

To find out what influences the shape of neuronal connections I simulated the branching patterns of neuronal dendrites. These are tree-like structures which receive input from other cells. Recent experiments indicate that dendrite branching is dependent on the phosphorylation status of microtubule associated protein 2 (MAP2) which affects the growth rate and spacing of microtubules. MAP2 phosphorylation can occur through calcium activation of the protein CaMKII. In the model the phosphorylation status and physical distribution of MAP2 within the cell can be varied to produce a wide range of biologically realistic dendritic patterns.

The final model simulates emergent synchronisation of neuronal spike firing which can occur in cultures of developing neurons. In the model the frequency and phase of cell firing is modified by the pattern of input signals received by the cell through local connections. This mechanism alone can lead to synchronous oscillation of the entire network of cells. The results of the model indicate that synchronization of firing in developing neurons in culture occurs through a passive spread of activity, rather through an active coupling mechanism.

Contents

List of Figures

Chapter 1

Introduction

> "It is evident that the total genetic information available to an animal – perhaps 10^5 genes in mammals – is not sufficient to specify the total number of neuronal interconnections that are made – perhaps as many as 10^{15}."

Principles of Neural Science: 1991 p.885: Kandel, Schwartz and Jessell.

1.1 From Growth Cones to Neuronal Networks

The motivation behind this thesis was to develop theoretical and computational models which would lead to an increased understanding of how the brain evolves from a few cells into a highly intricate and complex adult structure. The work in this thesis concentrates on three different stages of neuronal development:

- How neurons find their target cells.
- How neurons achieve their characteristic pattern of connections.
- How functioning neuronal networks are formed.

In order to achieve the engineering feat of wiring the brain together each developing neuron creates its own structure to assist in steering, elongation and general navigation - the growth cone. The growth cone forms at the tip of the neurite as it grows towards its target cells. It is the task of the growth cone to interpret the signals in the extracellular space such as adhesion channels, electric gradients and gradients of chemoattractants and repellants (Tanaka & Sabry, 1995). On arrival at the target area the growth cone branches to form multiple synaptic connections with the target neurons. These synapses are gradually refined by both activity-dependent and independent mechanisms throughout the lifetime of the organism.

In order to understand how neurons find their target cells the first three computational models simulate the dynamics of the developing axon (neurite) and growth cone. The first model deals with the properties of **microtubule** proteins. These display **dynamic instability** - a process in which the microtubule undergoes alternating periods of rapid growth and shrinkage (Mitchison & Kirschner, 1984a). The microtubules interact with the polymerised actin filaments (**F-actin**) which are created at the leading edge of the growth cone. Subseqently F-actin flows rearwards towards the neurite where it interacts with the extending microtubules (Forscher & Smith, 1988). In the first model the effect of shielding interactions between microtubules and F-actin on the rate of growth cone and axonal elongation is considered. The second model examines the effects of microtubule/F-actin interactions during growth cone turning. In the third model a possible mechanism underlying the dynamics of growth

cone **filopodia** is investigated. Filopodia are transient structures which rapidly emerge from, and shrink back, into the growth cone. Filopodia act as antennae at the tip of the growth cone and are crucial for normal axon guidance and turning (Davenport, Dou, Rehder, & Kater, 1993). In the model, calcium acts as a short range activator whilst cyclic-AMP acts as a long-range inhibitor. Under certain conditions transient and localised fluctuations of calcium occur. These could explain the formation of filopodia, their growth and subsequent shrinkage.

In order to understand how neurons achieve their characteristic shape a new computational model of cell dendritic branching was developed. Previous theoretical models have used abstract mathematical parameters to statistically characterize the shape of dendritic arbors e.g. (van Pelt, Dityatev, & Uylings, 1997). The aim of the new model was to simulate how these dendritic branching and elongation patterns might form using a biologically plausible intrinsic signalling mechanism. In contrast to the growth cone models which simulate cell dynamics over a period of seconds to minutes, the branching model simulates dendritic growth over several weeks. In the model, the dendritic elongation rate and branching probability are determined by the phosphorylation state of microtubule associated protein 2 (MAP2). Experimentally MAP2 plays a key role in controlling the functional state of microtubules within the axon (Brugg & Matus, 1991). Any modification of microtubule dynamics will affect both the rate of neurite elongation and the likelihood of dendritic branching. The model successfully reproduces the results from the statistical models whilst directly simulating the possible cellular mechanisms involved in the branching process.

The final model simulates the processes involved in the development of functional neuronal networks. Specifically, the model simulates the phenomenon

of emergent synchronized firing of cortical neurons in culture (Robinson, Kawahara, Jimbo, Torimitsu, Kuroda, & Kawana, 1993). Initially, the cells fire independently but gradually, over a few weeks of development, cells begin to fire synchronously. At the end of this period, the majority of the cells in the culture are firing with the same phase and frequency. The model extends a mechanism initially put forward to explain the synchronization of firefly flashing (Mirollo & Strogatz, 1990) to show how individual cell firing can drive the network to a state of synchronous oscillation. In the model, network synchronization is a stable solution which arises from the simple interactions of connected cells.

1.2 Relevant areas of research

The aim of each of the models is to show how complex biological behaviours which occur during the development of neuronal networks could result from the simple interactions of the underlying components. In addition to developmental biology, the work in this thesis may be relevant in the following areas of research.

- *Computational Neuroscience* To allow models of cell networks to be developed where realistic cell-cell connections are made.
- *Artificial Neural Networks* To abstract biological mechanisms of connection development for use in developing biologically inspired artificial neural networks.
- *Neural implants.* For degenerative disorders such as Parkinson's disease where fetal nerve tissue is implanted to create new dopamine producing cells to improve motor function. (See Lindvall (1994) for review.)

- *Nerve Regeneration.* Biologists interested in regeneration of nerves following injury, e.g. to the spinal cord following paralysis.

- *Controlling artificial limbs* Recent technology has allowed nerve signals to be processed by growing the regenerating nerves through a silicon electrode. The neural impulses can then be computationally processed to control the artificial limb (Bogdan, Babanine, Kaniecki, & Rosentiel, 1995). An increased understanding of this wiring process would lead to improvements in regrowing the nerves and developing new prostheses.

The work in this paper may be relevant to all of the above fields, although it lies primarily within the fields of developmental neurobiology and computational neuroscience.

1.3 Outline of the thesis

The layout of the thesis is as follows:

Chapter 2: **Forming Biological Neural Networks**. A brief biological introduction to the problems involved in the formation of neuronal networks including activity dependent and independent mechanisms of neuronal development.

Chapter 3: **The Biology of the Neuronal Growth Cone**. A more detailed account of the growth cone structure and its pivotal role in the developing neuron. This section introduces the subcellular systems involved in growth cone function including microtubule and F-actin dynamics.

Chapter 4: **Theoretical and Computational Models of Microtubules and Growth cones.** This section introduces ideas from previous theoretical models of microtubule and growth cone dynamics which have been revised or extended in the new models.

Chapter 5: **New Models of Growth Cone Dynamics.** This chapter introduces two models of microtubule and growth cone dynamics. The first model simulates the effect of microtubule-shielding interactions on the rate of axonal elongation. The second model analyses the conditions in which dynamically unstable microtubules invade the growth cone from the neurite shaft. This occurs following growth cone filopodial contact with a target cell. Results from the simulation suggest that microtubules specifically invade the growth cone in the direction of least F-actin flow (the direction of least resistance). Results from both models suggest that short term interactions between microtubules and F-actin can significantly affect long term axonal behaviour.

Chapter 6: **A New Reaction-Diffusion Model of Filopodia Dynamics.** This chapter introduces a new model to account for the mechanisms underlying growth cone filopodia dynamics. The simulation is based on the reaction diffusion model of "chemical morphogenesis" developed by Alan Turing (Turing, 1952). It is proposed that localised changes in calcium concentration in the growth cone could account for the creation of filopodia and their subsequent behaviour.

Chapter 7. **An Intrinsic Signalling Model of Neurite Branching.** This chapter introduces a new model of cell branching to explain what factors may cause cell dendritic arbors to assume their characteristic shape. The chapter also includes a biological description of the events underlying microtubule organisation and a discussion of previous theoretical approaches to the problem.

Chapter 8. **A Model of Synchronized Firing in Neuronal Network Development.** In contrast to the previous models of the dynamics of a single neuron, this chapter introduces the phenomena of emergent synchronization of spike firing during the development of neurons in culture. A new model based on firefly sychronization is introduced. In the model, the firing of one cell alters the phase of firing of neighbouring cells. This mechanism alone reliably results in synchronization of the entire network.

Chapter 9. **Discussion and Conclusions.**

Chapter 2

The formation of biological neuronal networks

> If a machine wired up every neuronal connection in the brain at the rate of 1 per second, it would take over 30 million years to complete the task. [1]

2.1 Introduction

The rate at which the embryonic brain forms neuronal connections is astonishing. In contrast to the 30 million years taken by the wiring machine above, the human brain completes the bulk of this task in a little under 9 months - the first neurons emerging from the developing neural tube after only 4 weeks. Furthermore the task of joining up the right connections seems relatively straightforward in comparison to the synaptic modifications that subsequently take

[1] Based on 10^{15} connections. See p1.

place. In order to carry out the transition from a population of unconnected cells to a fully functioning network each developing neuron is endowed with the ability to create a structure called the growth cone. The growth cone forms at the tip of the elongating axon and assists in the first two of the three main stages of making axonal connections:

- **Route finding**: The axons travel along a route that will lead them to a particular region of the embryo.
- **Target selection**: Once the axons have reached the correct area, they recognize and bind to a set of cells with which they may form stable connections. Growth cones also form at the tip of the developing dendrites to enable them to interact with growth cones of incoming axons.
- **Connection refinement**: The initial patterns of connections are often refined so that each axon may bind to a small subset (sometimes only one) of its possible targets. The connections that have formed are then modified primarily through electrical neural activity.

These three stages are described in more detail in the following sections.

2.2 Route finding

2.2.1 Contact Guidance

One of the first hypotheses to account for the specificity of axonal growth involves **contact guidance** or **stereotropism**. Here physical cues in the substrate

such as channels in the cell layers direct the growth of migrating axons. Cell layers may also act as a physical barrier to prevent the extension of growth cones until the cells in the target area are ready to receive incoming axons. The pathway of the tibial Ti1 pioneer neuron in the grasshopper has been fully mapped (O'Connor & Bentley, 1993). Along this route the growth cones migrate between the basal lamina and the basal sufaces of the epithelial cells which in addition express membrane-associated molecules. In some cases the route of the extending axon is marked by "guidepost cells" - pre-axonogenesis neurons which are derived from epithelial cells (Lefcort & Bentley, 1987). Interactions between the growth cone and guidepost cells can lead to a marked change in the direction of growth of the elongating axon. In the migration of the Ti1 pioneer neurons, guidepost cells in 3 different locations enable the growth cone to correctly navigate the complicated but stereotypical route to its target cells (O'Connor & Bentley, 1993).

2.2.2 Adhesion Gradients

In addition to providing directional guidance by relatively large channels and grooves, the extracellular matrix (**ECM**) can guide the growth cone by an adhesive gradient. This is known as **haptotaxis.** If the ECM is broad and allows the axon to grow in several directions an adhesive gradient would make one direction preferred over the others. On encountering a guidepost cell (Tr1 in the trochanter) the tibial axons in the grasshopper limb bud take a 90^0 degree right hand turn and grow along a channel of the adhesive molecule fasciclin IV[2] (Pini, 1994). The axons continue to grow along this channel by preferential adhesion and may also be inhibited from forming new branches until they leave the channel following contact with guidepost cell Cx1 in the coxa.

[2]This is a founder member of the semaphorin family now renamed G-Sema I.

Another ECM adhesion molecule is **laminin**. It has been shown *in vivo* that laminin provides a pathway through which trigeminal sensory axons grow to reach their peripheral targets (Letourneau, Madsen, Palm, & Furcht, 1988). Laminin has also been shown to influence the branching properties of hippocampal neurites *in vitro* (Lein, Banker, & Higgins, 1992).

2.2.3 Electrical Gradients

In vivo electric gradients fields have been observed in developing embryos (Hotary & Robinson, 1990) and it has been proposed that electric gradients act to define an invisible co-ordinate system for the establishment of the embryonic pattern (Shi & Borgens, 1995). Disruption of the natural electric fields may lead to developmental abnormalities such as skeletal and neural defects (Hotary & Robinson, 1994). These results suggest that electric gradients may induce the growth of functionally distinct regions in the early development of the embryo.

Electrical gradients can also be used to influence the direction of neurite outgrowth (McCaig & Rajnicek, 1991; Bedlack, Wei, & Loew, 1992). The mechanism for this appears to involve the redistribution of integral membrane proteins within the growth cone which migrate towards the negative cathode. This leads to an increase in the number of receptors, including the Acetylcholine receptor, at the membrane facing the cathode. This results in increased numbers of growth cone filopodia and subsequently turning of the neurite (Stewart, Erskine, & McCaig, 1995).

2.3 Target Selection

Chemical Gradients

Growth cones can be guided along the pathway to a target by gradients of diffusible chemicals that are secreted by certain cells within the target region. This is known as **chemotropism** and was first suggested as early as 1893 by Ramón y Cajal when studying embryonic chick neurons (Cajal, 1893)[3]. However the first compelling example that growth cones (from sensory neurons) can respond to a gradient of a soluble molecule was reported in 1979 (Gundersen & Barrett, 1979). In this case the soluble molecule was nerve growth factor (NGF) which was first purified by Cohen in 1960. The first diffusible chemotropic factors described in the vertebrate central nervous system (CNS) were members of the netrin family, netrin–1 and netrin–2, which are related to the ECM molecule laminin (Kennedy, Serafini, De la Torre, & Tessier-Lavigne, 1994). A large number of other growth factors has now been classified. These include brain derived neurotrophic factor (BDNF), fibroblast growth factor (FGF) and the rapidly expanding neurotrophin family NT1-5 (for a recent review of neurotrophins and their physiology see Lewin and Barde (1996)). Many of these growth factors act in concert to guide the incoming axons to their correct target area. For example, in addition to the guidepost cells and adhesion channels marking the pathway of Ti1 pioneer neurons there are also at least three distal-proximal chemical gradients (Norbeck & Denburg, 1992).

An important recent finding was that chemicals could also be used to repel growth cones. Repulsion may play as important a role as attraction in the formation of connections. (For a review see Keynes and Cook (1992).) In some

[3]as cited in (Kandel, Schwartz, & Jessell, 1991) p911.

cases the same molecule can have both attractive and repulsive effects. Netrin–1, which is expressed by floor plate cells of the developing spinal cord has a long–range chemoattractive (Kennedy et al., 1994) and chemorepulsive (Colamarino & Tessier-Lavigne, 1995) action on commmissural and trochlear motor axons respectively.

It was also recently discovered that the neurotransmitter acetylcholine could act as a diffusible chemoattractant to influence neurite outgrowth (Zheng, Buxbaum, & Heidemann, 1993). This suggests that the release of neurotransmitter by active target sites may be used to direct incoming axons towards their specific destination. This mechanism may bridge the gap between activity-independent, and activity-dependent mechanisms of connection formation which are discussed in the next section.

2.4 Connection Refinement

The selection of the correct pathway and target cells allows highly specific connections to be made without the presence of neural electrical activity. However once connections are made electrical activity is essential in refining synapses to create a functioning network. Electrical activity is known to play a key role in many systems including the following:

- **Formation of the neuromuscular junction** At the neuromuscular junction growth cones of motoneurons reach and synapse with their muscle target fibres by using activity-independent guidance and recognition cues (see Figure 2.1). The connection process results in the innervation of

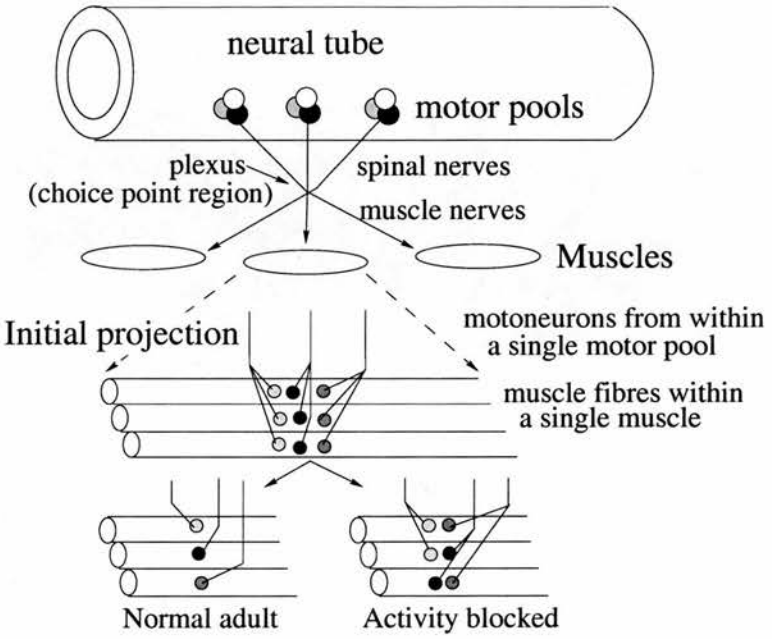

Figure 2.1: Activity dependency at the neuromuscular junction (adapted from Goodman and Shatz (1992).)

each muscle fibre by several different axons. Activity-dependent mechanisms are required to transform this state of multiple innervation into the normal adult pattern of innervation in which each muscle fibre receives input from only one motoneuron. Blockage of activity prevents or delays this process of synapse elimination. (Thompson.W.J., 1986; Goodman & Shatz, 1992).

- **The visual system:** In lower vertebrates, e.g. fish, amphibia, and birds, activity-independent mechanisms set up a coarse mapping of axons from the retina to the optic tectum. These patterns are then refined by neural activity. (Figure 2.2:A). In mammals axons from the lateral geniculate nucleus (LGN) form an initial coarse topographic map in the visual cortex using activity-independent pathway and target-selection mechanisms (Figure 2.2:B). However neural activity plays an essential role in refining neighbouring connections and synapses. As development pro-

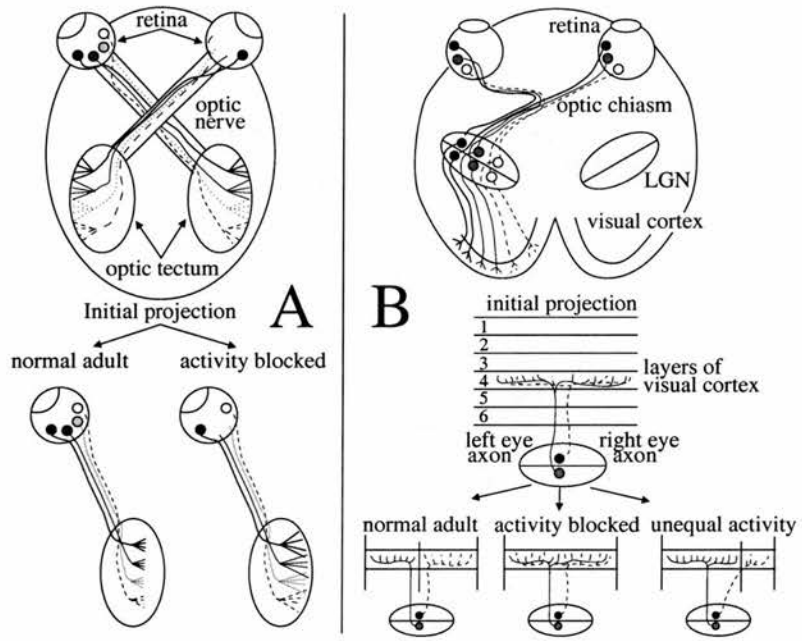

Figure 2.2: Activity dependency in frog (A), and mammal (B) visual systems (adapted from Goodman and Shatz (1993)).

ceeds, activity dependent mechanisms remodel LGN axons to form ocular dominance columns. Without this activity, the LGN axons from the two eyes remain intermixed. (Shatz, 1990; Goodman & Shatz, 1992).

- **Purkinje Cells in the Cerebellum:** In the cerebellar cortex, Purkinje cells are initially innervated by several climbing fibre axons from the inferior olivary nucleus. Over a period of a few weeks, competition between climbing fibres proceeds until each Purkinje cell is innervated by only one climbing fibre (Kandel et al., 1991).

2.5 Adult Plasticity

The mechanisms underlying routefinding, target-selection and synaptic refinement work together during development to establish highly complex net-

works of neural connections. In the adult organism however, the activity independent guidance mechanisms of the growth cone only remain functional in the peripheral nervous system (**PNS**). In the case of injury to muscle nerve in the adult, a new growth cone forms to guide the axon through a channel marked by Schwann cells and the disintegrating nerve end to reach the original target (Son & Thompson, 1995). At the same time, neighbouring cells sprout new axonal collaterals to innervate the muscle fibre previously occupied by the displaced injured nerve (Barry & Ribchester, 1995). This can occur many years after the original growth cones first guided developing axons to their targets indicating that the pathfinding ability of the growth cone is not lost following its transformation into a synapse. From these experiments it appears that the adult PNS is not static but maintained in a continuous state of dynamic equilibrium.

In contrast in the CNS most axons regenerate very poorly following injury. In the mammalian CNS, with the exception of the olfactory system, neurons are born and complete their differentiation in the embryo and during a brief period after birth. In the olfactory system, the growth and differentiation of sensory neurons continues throughout adult life. The newly born olfactory cells extend processes that grow into the olfactory bulb where they make direct connections with various glomeruli. In this system there is a continuous turnover of cells and connections (Graziadei & Monti-Graziadei, 1979).

Elsewhere it seems that any activity-independent mechanisms of regrowth are either not present or, if present in the adult, are functionally inhibited. The defect may not lie in the CNS neurons themselves. If a segment of peripheral nerve is inserted into the brain axons of central neurons will invade and grow vigorously along them (Richardson, McGuiness, & Aguayo, 1980). Embryonic neurons transplanted to an injured site in the brain can also reinnervate and

restore function to denervated target neurons (Bjorklund, Lundvall, Isacson, & Brundin, 1987). However this only happens if they are transplanted near to the target area. The ability of adult neurons to regrow may be restricted to specific cell types. The ongoing production of new cells in the olfactory system may occur partly as a consequence of the continued expression of the embryonic form of proteins such as microtubule-associated protein (MAP). In contrast the cortex switches to the adult form of these proteins shortly after birth (between 10 and 20 days in the rat) (Viereck, Tucker, & Matus, 1989). Embryonic retinal ganglion axons are also able to regrow successfully to the target whilst mature axons (only postnatal day 4 in the hamster) are unable to regrow (Chen, Jhaveri, & Schneider, 1995). In this specific case it seems that the failure to regrow is an intrinsic property of the mature cell. In other parts of the brain the failure of mature axons to regrow may not be due entirely to the failure of intrinsic regrowth mechanisms in the cell. Instead it may be due to an environment which is more hostile to the regrowth of nerves. Four possible mechanisms for this are (summarized from Brown, Hopkins, and Keynes (1991), Chapter 12)

- *Lack of endoneurial sheaths.* These exist only in the periphery, where they guide regenerating axons very successfully.
- *Lack of growth stimuli.* The oligodendroglia (the CNS equivalent of Schwann cells) which wrap themselves around the axon, may fail to provide either surface molecules needed for attachment, or soluble molecules needed both to maintain the cell body during regrowth, and to guide it back to its original target.
- *Production of growth inhibitors* These may be produced by neuroglial cells - astrocytes, oligodendroglia and associated myelin. Evidence for this comes from the observation that antibodies against a myelin–associated

inhibitory protein can allow some degree of long axon regrowth (Caroni & Schwab, 1988).

- *Formation of scar tissue.* This can occur at the site of injury and act as a physical barrier against regrowth.

Research in overcoming the problems of regrowth of connections in both the CNS and PNS, particularly at the neuromuscular junction, has led to an increased understanding of the mechanisms acting at the level of the growth cone. By manipulating these mechanisms, it is hoped that successful operations following nerve injury can be carried out. In this field, recent progress has been made in regenerating spinal cord segments in the neonatal rat (Iwashita, Kawaguchi, & Murata, 1984). In this experiment the lower thoracic segments of the spinal cord were resected and embryonic spinal cord segments were grafted into their place. The replaced segments united with the host spinal cord and promoted robust growth and regrowth of axons across the graft. The animals with replaced segments could walk, run and climb with almost normal hind-forelimb coordination. For a review of nerve regeneration enhancement see Woolford and Toriumi (1995).

In almost all aspects of neuronal network formation including nerve regeneration, the growth cone plays a fundamental role. This, coupled with the few theoretical models of growth cone dynamics or related systems (discussed in Chapter 4) motivated the development of the computational models introduced in Chapters 5 and 6. Before that, the following chapter discusses the biochemistry of the growth cone in more detail and looks at the mechanisms by which it is able to correctly guide the growing axon to its target.

Chapter 3

The biology of growth cones

3.1 Background

First identified by Ramon y Cajal in the 1890's (Cajal, 1893) the growth cone is a structure which develops at the tip of the neurite to guide the growing axon to its target (see Figure 3.1). The growth cone is involved in decision making, turning and elongation of the axon. Growth cones develop at the tips of developing dendrites. At the leading edge of the growth cone membrane, **filopodia** appear as long thin spikes of membrane and act as sensory antennas. These convert directional signals from the extracellular space into an internal signal that the growth cone can use to (re)direct its movement.

The forward movement of the developing axon and growth cone is characterised by three stages: exploration, orientation and consolidation. In the exploration phase, the growth cone filopodia sample the extracellular space for directional signals. In the orientation phase, a single filopodia may establish

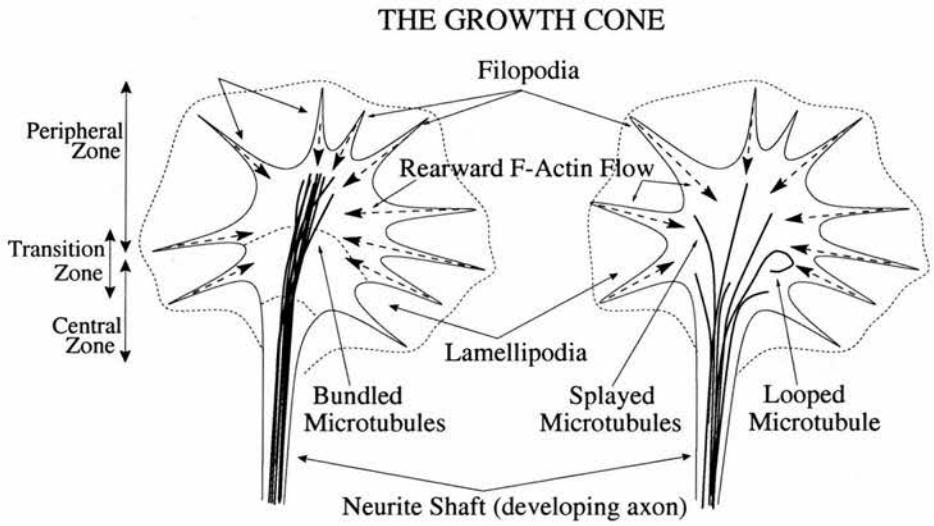

Figure 3.1: The diagram shows bundled, splayed and looped microtubules extending from the tip of the neurite shaft into the growth cone. At the transition zone they encounter F-actin flowing rearward from the peripheral zone where it is assembled. Dynamically unstable microtubules alternately grow out from the neurite shaft into the growth cone before experiencing a catastrophe (a switch from growth to shrinkage) and then shrink back into the neurite shaft where they are rescued (shrinkage to growth).

---

the future direction of growth leading to invasion of this branch of the growth cone by large numbers of axonal microtubules (see below). Finally, in the consolidation phase, a new growth cone forms at the tip of the leading filopodia. Over a period of about twenty minutes the old growth cone loses its adhesiveness to the substrate and is converted into new axon (Tanaka & Sabry, 1995). When a growth cone reaches its correct target, it halts, and remodels itself to form a synapse (Broadie, Sink, VanVactor, & Fambrough, 1993). Figure 3.1 shows the two major regions of the growth cone, the **central** and **peripheral zones**.

The central zone is characterized by the rapid directed transport of organelles, mainly neurosecretory granules and mitochondria. The cytoplasm in the central zone (axoplasm) has a high concentration of **microtubules (MTs)**, a polymerized protein made up of tubulin dimers. Microtubules are important in

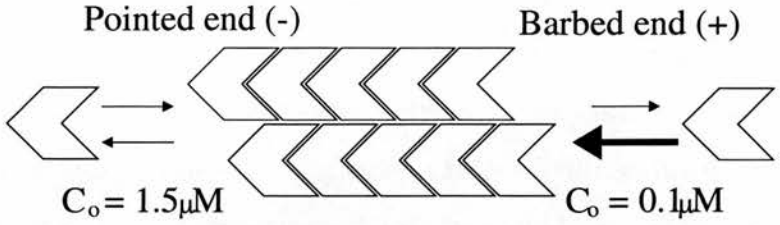

Figure 3.2: Schematic diagram showing F-actin (de) polymerization reactions. The critical actin monomer concentrations (C_o) above which polymerization will occur are 0.1 μM and 1.5 μM for the barbed and pointed ends respectively. Reproduced from Forscher (1988).

giving structural support to the axon. The peripheral regions are dominated by filopodia and lamellipodia, the membrane stretched between filopodia. In contrast to the central zone the cytoplasm in the peripheral regions (kinetoplasm) has a very low organelle density and a high concentration of the **F–Actin** polymer. The region of the growth cone comprising the central/peripheral interface is referred to as the **transition zone** (Forscher & Smith, 1988; Mitchison & Kirschner, 1988).

3.1.1 Growth Cone Dynamics: F–Actin

The peripheral region of the growth cone has a high concentration of the actin protein in both the monomer and polymer state. Actin monomers are polarized molecules that assemble into polarized filaments (**F–Actin**) that have so–called 'barbed' (+) and 'pointed'(-) ends (see Figure 3.2). Filament assembly is highly preferred at the barbed end due to a 5–10 fold higher on–rate constant here (Forscher, 1988).

Monomeric actin normally polymerizes into F-Actin at the leading edge of the growth cone and then flows rearward towards the central zone at a rate of 3–6

μm/min (Forscher & Smith, 1988). Treating the growth cone with Cytochalasin B inhibits F-actin polymerization primarily by capping the barbed end of actin filaments. When the growth cone is treated with Cytochalasin B for greater than 5 minutes, the F–actin network is completely eliminated and microtubules from the central zone invade the outer regions of the lamellae. The rearward flow of F-actin does not depend on distal actin polymerization at the leading edge for motive force. When F-actin polymerization was blocked by the application of Cytochalasin B the remaining polymer continued to flow centripetally at control rates (Forscher & Smith, 1988). Later experiments have indicated that the continuous rearward flow of F-actin is powered through F-actin interactions with the molecular motor **myosin** (Zot, Doberstein, & Pollard, 1992). The subsequent removal of Cytochalasin B from the medium allows rapid ($<$ 5 min) and complete recovery of growth cone motility and structure (Forscher & Smith, 1988). Thus F–actin has a vital role in maintaining motility of the growth cone and also in controlling the spatial distribution of microtubules.

Recently Lin and Forscher (1995) observed that growth cone advance is inversely proportional to retrograde F–actin flow. In Aplysia growth cones plated on a non-permissive substrate, the F-actin network flows rearwards at rates of up to 6μm/min (360 μm/hour). In contrast, in rapidly migrating fish keratocyte cells which extend at a rate of up to 300 μm/hour the F-actin network is almost stationary. During normal growth cone movement intermediate values of rearward F-actin flow varying between 0 and 6μm/min are obtserved. They proposed a clutch mechanism where a greater adhesion of the F-actin network to the substrate changes the default retrograde flow of polymer into a forward movement of the growth cone. (See Figure 3.3). This occurs through transmembrane coupling of the F-actin network to the substrate. Binding of extracellular matrix molecules to membrane receptors modifies the

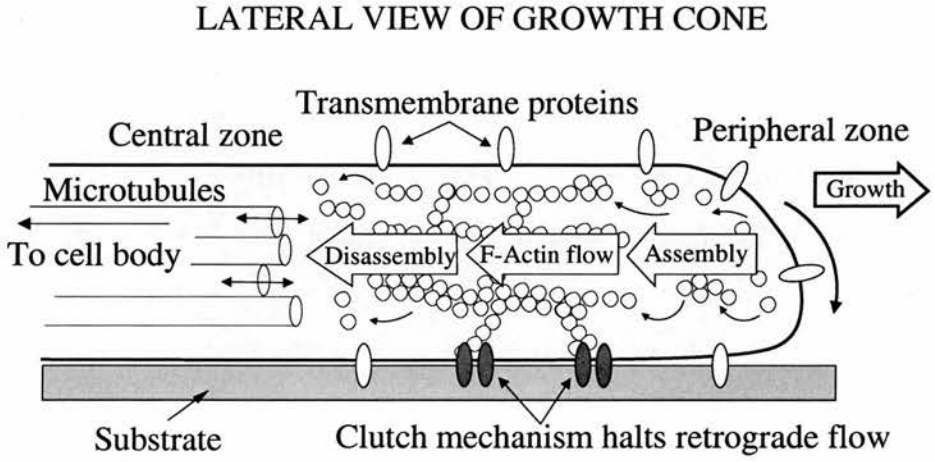

Figure 3.3: Retrograde flow of F–actin may be halted by coupling to substrate.

binding of molecules such as integrin which crosslink the F-actin with the membrane. When the F-actin network is not secured to the substrate it flows freely rearwards. However when the F–actin network is coupled through the lower membrane to the substrate, the continued action of myosin motors leads to the forward movement of the top membrane. Through this mechanism the growth cone crawls forward in a movement similar to the "caterpillar" treads of tanks. This mechanism is similar to a previous model of cortical flow in animal cells proposed by Bray (1988). Recent experimental results support the proposed clutch-mechanism. It was found that the Integrin superfamily cell adhesion molecule apCAM can mediate growth cone steering by substrate - cytoskeleton coupling (Suter, Errante, Belotserkovsky, & Forscher, 1998).

3.1.2 Microtubule Dynamics

Microtubules are cytoplasmic filaments that are important structural elements of the axon and also play a role in the transport of organelles. They are primarily concentrated in the central domain of the axon and can extend far out into

the peripheral zone, although they are not found in filopodia. Microtubules are the polymerized form of the tubulin dimer (made up of α and β subunit monomers). Microtubule polymers are helical proteins, with 13 tubulin dimers per helical revolution. One end of the microtubule (the minus (-) end) is usually stabilized in the neurite shaft. However the plus (+) end of the microtubule is free to "explore" the growth cone by the addition or subtraction of tubulin dimers in a process which is called **dynamic instability** (Mitchison & Kirschner, 1984b).

The dynamically unstable microtubules found in the growth cone and the tip of the neurite shaft exist in either a growing or shrinking state. These microtubules cannot be treated as simple equilibrium polymers as these would require a large change in tubulin concentration to shift from rapid elongation to rapid shrinking. In contrast dynamically unstable microtubules are highly sensitive to small changes in the tubulin concentration (Kirschner & Mitchison, 1986). The transition from a growing to a shrinking state is called a "catastrophe" and the opposite transition from shrinking to growing is called a "rescue". Dynamically unstable microtubules can be characterised by 4 parameters: **rate of growing, rate of shrinking, frequency of catastrophe** and **frequency of rescue**. Table 3.1 gives biological values of these parameters. The frequency parameters determine the probability that a microtubule will undergo a state transition in a given period of time. Individual microtubules at the tip of growing *Xenopus* neurites undergo on average 0.72 catastrophes and 1.74 rescues in one minute (Tanaka & Kirschner, 1991)

The dynamic instability characteristics of microtubules gives them a unique role in the developing neurite. Conditions in which microtubule polymerization is favourable lead to the rapid extension of microtubules from the central zone of the neurite shaft into the leading edge of the growth cone. Much

		Xenopus neurons[1]	Xenopus extract[2]
Growth in μm/min	V_g	10.5 ± 1.9	9.3 ± 4
Shrinkage in μm/min	V_s	9.7 ± 2.2	12.8 ± 6
Rescue frequency/min	F_{res}	1.74	0.6→1.86
Catastrophe freq./min	F_{cat}	0.72	0.54→0.96

Table 3.1: Values of parameters characterising microtubule dynamics (mean±s.d.). [1]Tanaka and Kirschner 1991, [2]Belmont *et al.* (1990).

---

of the structural support for newly generated axon in the developing neurite comes from the invasion of microtubules from the central domain into the periphery of the growth cone. When pioneer growth cones in the embryonic grasshopper limb encounter "guidepost" cells, microtubules selectively invade those filopodia that have contacted the guidepost cell (Sabry, O'Connor, Evans, Toroian-Raymond, Kirschner, & Bentley, 1991). The absence of microtubules from filopodia indicates that microtubules are unlikely to play a large role in exploration of the extracellular space. However microtubules can assist in steering the growth cone in the following ways:

- **Selective Invasion**: Microtubules invade only those branches that are found in the future direction of neurite extension.
- **Selective Retention**: Microtubules randomly invade all branches, and are subsequently stabilized in those extending in the preferred direction.

Where selective invasion occurs it seems likely that certain regions of the growth cone are more receptive to microtubule invasion or assembly. This may be due to a local decrease in the strength of the rearward F–actin flow which under normal conditions physically prevents the microtubules from expanding. This is suggested by ultrastructural observations (Letourneau, 1983), experimental perturbations of F-actin using Cytochalasin B (Forscher

& Smith, 1988) and physically restricting F-actin flow using restrained beads (Suter et al., 1998). In the clutch model (Lin & Forscher, 1995) growth cone contact with the cell results in a greater attachment of the F–actin network to the substrate and reduces the rearward F-actin flow. The tension imposed on the microtubules by the F–actin network is reduced with the result that the microtubules will invade the growth cone in the target direction.

During microtubule invasion of the growth cone, fluorescently marked axonal microtubules have been observed to move distally into the growth cone even in the absence of axonal elongation (Reinsch, Mitchison, & Kirschner, 1991). This suggests that microtubule translocation may contribute to the movement of microtubules into the growth cone. In most cases however, the microtubule invasion into the growth cone represents new microtubule growth using the cell's large pool of unassembled tubulin (Baas & Black, 1990; Bamburg, Bray, & Chapman, 1986). Neurites can be artificially induced by tension in a manner similar to the pulling of the axon by the growth cone. In neurites created in this way, the microtubule array formed reflects primarily new microtubule assembly rather than existing microtubules that were reorganized to invade the neurite (Zheng et al., 1993). Growth cone elongation is also severely restricted following application of the microtubule-assembly inhibitor nocodazole. In the new computational models presented in Chapter 5 microtubule extension is by new assembly of tubulin rather than translocation.

Following on from exploration and orientation come consolidation and stabilization. As long as both F-actin and microtubules are in their dynamic state, any pathfinding decisions will be transient. To make any forward advance of the growth cone permanent, the kinetoplasm of the peripheral growth cone must be converted into the axoplasm of the central zone. During this consolidation phase, both F-actin and microtubules are stabilized to some extent. The

F-actin cortex which is stabilized in the target direction continues to flow rearward in the off-axis direction to growth. This exerts a lateral force on splayed microtubules in the growth cone and may assist in the process of bundling the microtubules together into the densely packed array typical of axoplasm. During the bundling process microtubule associated proteins **MAPs**, e.g. MAP2 in dendrites and tau in the axon, also play a large role in stabilizing the microtubules against shrinkage (Maccioni & Cambiazo, 1995). Finally the old growth cone loses its adhesiveness for the substratum. A new segment of axon has formed and a new growth cone will develop at the tip of the leading filopodia (Mitchison & Kirschner, 1988).

New axon can also be formed "artificially". Dennis Bray (Bray, 1984) developed a machine called the "Cell Puller" which allowed a microelectrode to be inserted into the neurite. When the microelectrode was slowly pulled it dragged along the neurite membrane. It was found that new axon which formed behind the electrode was structurally identical to normal axon. Subsequent experiments on embryonic chick sensory neurons confirmed that pulling the cell margin induces neurite formation *de novo* (Zheng et al., 1993). The neurites created in this way contained microtubules within minutes after the application of tension and apparently normal microtubule arrays within 10-20 minutes. However this experiment may reflect the behaviour of the axon during its passive growth phase rather than during dynamic elongation by the growth cone. From Bray (1984):

> "Although most axons have a growth cone during their initial development, this is not the only way they can grow. For many axons there is a second phase in which having formed stable synaptic connections at their termini, they increase in length coordinate with the surrounding tissue. This second phase of growth, termed "passive

> stretching" by Harrison (1935) and "towing" by Weiss (1941) can be extensive and rapid. For example, a human motor neuron innervating a muscle in the lower leg may be 1m long in an adult but only 1 cm in a 7–8 week embryo, at the time at which it is forming its synaptic connections. The extent of passive growth that occurs while the axon is attached to its muscle is consequently some 100 times that taking place behind a growth cone. Furthermore, at the peak rate of growth of a human foetus (about 11 cm/month at the fifth month, (His, 1874)) the motor axon in question will be increasing in length at a rate of about 50 μm/hour. This is as fast as growth cones advance either in an embryo or in tissue culture (Hughes, 1953)."

Although the tension created by pulling the neurite leads to normal axonal development it may stimulate mechanisms involved in the "towing" phase of the axon, rather than its elongating behaviour when lead by the growth cone. During the towing phase of growth, tension is produced as a consequence of the growth of surrounding tissues. In the initial formation of the axon behind a growth cone, tension is controlled by modifying the strength of the interaction between F-actin and the substrate (Dennerll, Joshi, Steel, Buxbaum, & Heidemann, 1988). These results suggest that one of the major functions of the growth cone is to manipulate the rearward flow of F-actin so as to produce a directed stabilizing force at the tips of the elongating microtubules.

It has been suggested that F–actin and microtubules are in a complementary force interaction (Joshi, Chu, Buxbaum, & Heidemann, 1985): the actin network is under a tension that is partly supported by microtubule compression

and partly supported by the underlying substrate.[1] Such a mechanism provides a means for integrating microtubule assembly with the advance of the growth cone. Growth cone advance shifts a small amount of tension onto the environment, relieving some of the compressive force on microtubules and thus lowering their critical concentration for assembly (Dennerll et al., 1988). The change from a small to a large compressive F-actin force against the microtubules affects microtubule polymerization dynamics in the growth cone. During growth, the polymerized:soluble tubulin ratio is 4:1 compared to only 1:4 whilst shrinking (Dennerll et al., 1988). Changes in the rate of rearward F-actin flow can change the polymerized:soluble tubulin ratio by approximately 13:1. This experiment showed that the rate of microtubule growth in the neurite shaft is not directly linked to free tubulin concentration as this is in fact lowest during rapid elongation.

Although microtubule elongation depletes tubulin resources, a large pool of soluble tubulin remains. The concentration of soluble tubulin in the growth cone has been estimated at 5-10 μM and the cell is able to sustain this resource in order to support rapid and extensive microtubule polymerization (Mitchison & Kirschner, 1987). Any momentary decline in tubulin–subunit concentration due to polymerization is compensated for by increased synthesis. It has been shown that several eukaryotic cells control tubulin synthesis by a feedback mechanism of rapid kinetics based on free tubulin concentration (Cleveland, Pittenger, & Lopata, 1983). There is no evidence to suggest that the effective tubulin monomer concentration is different in different parts of cells as is the case for actin. There is thus no evidence that tubulin polymeriza-

[1]This complementary force interaction has been compared to the interaction of structural elements in the "tensegrity" architecture. This architecture describes how Buckminster Fullerene Carbon-60 molecules ("bucky balls") are stabilized through compressive interactions between the carbon atoms (Fuller, 1961).

tion is regulated at the level of monomer sequestration (Mitchison & Kirschner, 1987). These findings account for the results of the "cell pulling" experiments (Bray, 1984) where it was found that new axon could be artificially induced by pulling on the membrane at any part of the cell. Normal axon could be created in this way by towing the cell at high speeds of up to 100 μm/hr and for increases in length of up to 960μm (Bray, 1984). These experiments show that in normal conditions rapid microtubule polymerization is only restricted through tension imposed on the microtubule tip by the rearward flow of the F-actin array.

Any changes in tension on the microtubule tip will have an important effect on microtubule behaviour as dynamic instability allows the microtubule population to switch between growing and shrinking states. In this way microtubules can play a vital supporting role in the pathfinding of the developing neurite through their interactions with the F-actin network. These interactions are simulated in the new model of growth cone dynamics introduced in Chapter 5. Before that the following chapter discusses previous theoretical and computer models of growth cones and developing neurites.

Chapter 4

Theoretical and Computer Models of Microtubules and Growth Cones

4.1 Introduction

Since the original paper by Mitchison and Kirschner (1984a) on dynamic instability of microtubules a number of theoretical models have been put forward to make sense of microtubule dynamics and neurite elongation. This section discusses some of these models which provide the background to the new computational models introduced in Chapter 5.

4.2 Biophysical models

4.2.1 Theoretical treatment of microtubules in solution.

The first theoretical models set out to explain the differing behaviour of dynamically unstable microtubules from normal equilibrium polymers. Hill and Chen used Monte Carlo kinetic simulations to show dynamically how the growing and shrinking phases of dyamic instability could take place at the tip of a microtubule (Hill & Chen, 1984; Hill, 1984; Chen & Hill, 1985). They first modelled an equilibrium polymer, and then extended their analysis to incorporate the two-phase growth and shrinkage dynamics of microtubules.

The equilibrium model simulated the increase or decrease in microtubule length by one tubulin unit. The current state of the microtubule was represented by P_0 (see Figure 4.1A). The future growth or shrinkage states P_1, P_2 etc, depended on the ratio of the first order on/off rate constants λ and λ' which were related to the concentration of free tubulin. At steady state the equilibrium polymer system was described by the following equations:

$$P_1 = (\lambda/\lambda')P_0, \qquad P_2 = (\lambda/\lambda')P_1, = (\lambda/\lambda')^2 P_0 \tag{4.1}$$

The microtubule grows from state P_0 to state P_1 if $\lambda > \lambda'$ and shrinks if $\lambda < \lambda'$. When $\lambda = \lambda'$ then $P_1 = P_0$. In this case there is no net polymer growth or shrinkage and the end of the polymer is static.

In contrast, even at steady state a dynamically unstable microtubule is either growing or shrinking. The determining factor in this behavior is the state of the microtubule cap. During growth, the microtubule is capped with a "T unit"

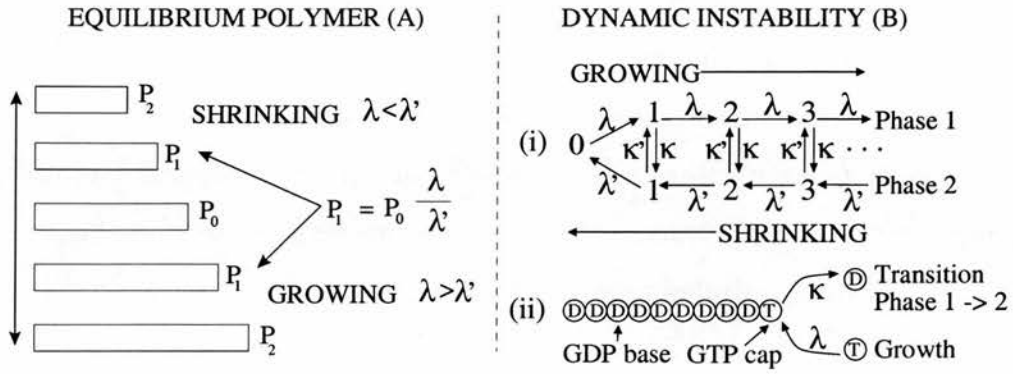

Figure 4.1: A. Dynamics of equilibrium polymer B(i) The 2–phase model allows growth, shrinkage and transition states. (ii) Growth of the GTP capped polymer.

(tubulin monomer bound with GTP, or T-GTP), rather than with a "D unit" (tubulin bound with GDP, or T-GDP). During growth, T-GTP units are added to the microtubule already capped with T-GTP. It was hypothesized that if this GTP cap was somehow lost due to external causes then the remaining polymer capped by GDP would be unstable and rapidly shrink. The polymer continues to shrink until it is once again capped with T-GTP units.

Chen and Hill extended the equilibrium model to include rate constants for rescue and catastrophe transitions κ, κ'. These allow transitions from phase 1 (growing) to phase 2 (shrinking) and vice versa. The phase diagram for their (simplified) two–phase model is shown in Figure 4.1B(i). In this two–phase model the microtubule end has a GTP cap that fluctuates in size. In the first phase the microtubule grows slowly whilst in the second phase the microtubule shrinks rapidly and may disappear completely. Their two phase model showed qualitatively how microtubules can grow well below the critical concentration of tubulin monomer for the steady state and how microtubules can rapidly disappear by shrinkage following a phase change. In *in vitro* experiments of microtubules in solution the average number of microtubules decreases with time and the average length of the remaining micro-

tubules increases (Mitchison & Kirschner, 1984a). In the microtubule population longer microtubules are more likely to undergo a rescue before they shrink to zero length. Shorter microtubules are more likeley to depolymerize completely releasing free tubulin into solution which then drives the assembly of the longer microtubules which remain. The computer simulations of numbers and lengths of microtubules remaining after a given length of time (Chen & Hill, 1985) were in general agreement with those found experimentally from the above *in vitro* work of Mitchison and Kirschner.

4.2.2 The Lateral Cap Model

The theoretical analysis of Chen and Hill was known as the GTP–cap model as it postulated that the key element of dynamic instability was the presence or absence of a GTP based cap. In the model there was no direct link between the addition of a T-GTP molecule and GTP hydrolysis. The assembly rate of tubulin-GTP monomers was independent of the rate of tubulin hydrolysis within the microtubule from the GTP to the GDP state. If monomer T-GTP addition during rapid growth exceeded hydrolysis then the growing microtubule would contain a significant amount of non–hydrolysed GTP. This principle is known as the GTP-Cap model. Random fluctuations in the size of this cap from several hundred tubulin molecules down to zero were implicated as responsible for the conversion from a stable, growing microtubule into a rapidly shrinking one.

As a result of continued experiments the GTP cap model was found to be unsatisfactory in a number of ways. Firstly experimental results failed to detect a significant T-GTP cap. Secondly evidence was obtained which linked T-GTP

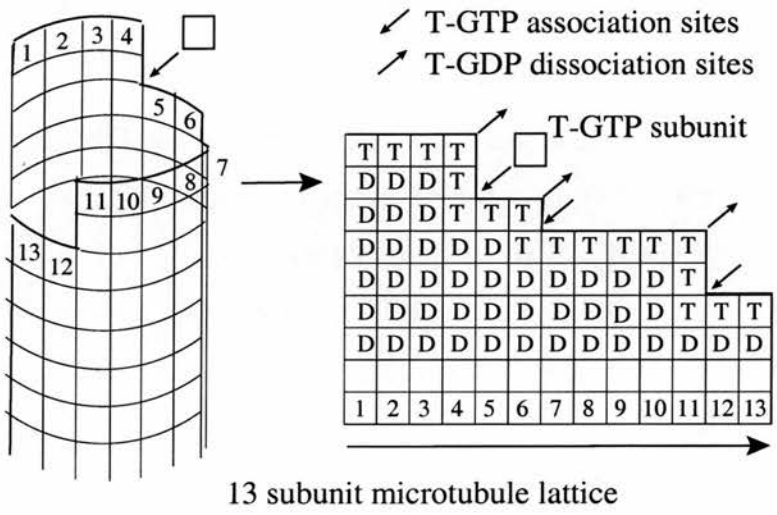

Figure 4.2: Dynamics of The Lateral Cap Microtubule Model. New tubulin dimers can only be added at a limited number of sites in the microtubule lattice

addition directly to T-GTP → T-GDP hydrolysis. This lead to the development of the Lateral Cap model (Bayley, Schilstra, & Martin, 1990).

A normal microtubule is made up of a helix of 13 tubulin dimers in each rotation. In the Lateral Cap model the end of a microtubule is simulated as a lattice with 13 filaments (Figure 4.2). The addition and loss of subunits occurs with rate constants that depend on the GTP/GDP state of neighbouring subunits in the lattice. Not all sites are available for the addition or subtraction of tubulin units as the binding step involves interaction with at least one lateral and one longitudinal tubulin molecule. During growth or shrinkage there are on average only 3 or 4 sites available where tubulin binding/disassociation can take place (Figure 4.2). Each of the tubulin units is in either a GTP or a GDP state. As GTP hydrolysis is directly coupled to subunit addition the GTP cap is at most only one layer deep. This model was able to account for the switching of individual microtubules between a growing and a shrinking state in terms of the experimentally validated tubulin make up of the tip of the microtubule.

4.3 Probability analysis of microtubule dynamics

Both the GTP cap model and lateral cap model simulated the addition and loss of individual tubulin dimers at the tip of the microtubule. These models show how the characteristic dynamic instability properties of the microtubule lattice can arise. However this level of complexity is not required in order to simulate more general microtubule behaviour. A simplified model of microtubule dynamics was developed by Holy and Leibler (1994) and based on the four global parameters that characterise microtubule dynamic instability.

1. Speed of growing v_g
2. Speed of shrinking v_s
3. Frequency of catastrophe (growing to shrinking) f_{cat}
4. Frequency of rescue (shrinking to growing) f_{res}

In contrast to the work of Hill and Chen on dynamics at the tip of the microtubule, this model did not take into account the concentration of either monomer or polymer tubulin or the probabilities of single tubulin units being either added or subtracted. These are approximated by the four global variables above.

The model was used to analyse the formation of the mitotic spindle. During mitosis microtubules nucleate in the centrosome and extend out into the surrounding environment in search of chromosomes. Holy and Leibler (1994) modelled dynamically unstable microtubules as a two–state polymer (**TSP**) to test whether they found targets corresponding to chromosomes quicker than a normal equilibrium polymer (a single state polymer, **SSP**).

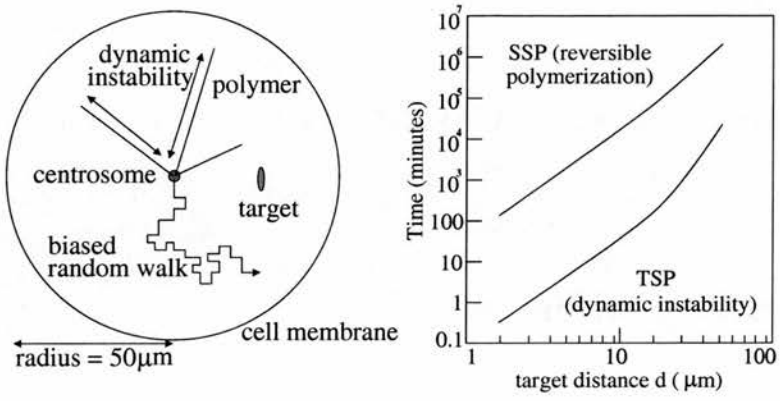

Figure 4.3: Microtubules searching for chromosome targets during mitosis. (a) The model set up of Holy and Leibler. (b) Time taken for microtubules to find target chromosomes using either dynamic instability (TSP) or reversible polymerization (SSP). (Sketched from (Holy & Leibler, 1994)).

In the model individual microtubules grow out in random directions from the centrosome until they encounter a target of cross–sectional area 1 μm^2 at a distance d. The distance d was varied from 2 to 50 μm. This is shown in Figure 4.3a. The average microtubule excursion length l of a dynamic microtubule was given as:

$$l = \frac{v_g v_s}{f_{cat} v_s - f_{res} v_g} \tag{4.2}$$

They found that the global minimum search time occurred when:

1. The microtubule excursion length l was approximately equal to the distance d.

2. The rescue frequency f_{res} was set to 0.

In the simulations the polymer grew out until either it encountered the target or a catastrophe occurred. It would then shrink back to zero length (without rescue) and start growing in a different, random direction. The equilibrium

polymer was modelled using a biased random walk with the same overall reaction rate as the dynamically unstable microtubules (the average number of tubulin units added per minute was the same in both cases).

4.3.1 Results of the model

Figure 4.3b shows how the average search time depends on the target distance d. When the average length l was 9.4 μm, dynamically unstable microtubules were up to 1000 times faster at finding close targets ($d = 2\mu m$) than the biased random walk with the same reaction rate (< 1 minute compared to > 100 minutes). However for both the equilibrium and dynamic instability polymers the time taken to find the target increased by a factor of 1000 when the target distance was significantly greater than the average polymer length. When the target was at its maximum distance of 50 μm, dynamic instability was still 15 times faster than the random walk. These results are similar to experimental values for capturing chromosomes. In newt cells when chromosomes are less than 30 μm from the centrosome the average time for capture is 10 minutes. However if the target is at 50 μm, the capture can take as long as 5 hours (Rieder & Alexander, 1990).

There seems to be a problem with this model as I found that the simulation results shown for 250 microtubules in Figure 2 of this paper do not correspond to the values derived from the theoretical analysis for 1 microtubule discussed in their Appendix 2. I extended the theoretical analysis for 1 microtubule to N microtubules as follows. The probability of 1 microtubule finding the target on any given excursion is p (and failing is q=1-p). The probability of N=250 microtubules failing is $q^{N=250}$, so the probability that at least 1 microtubule will

find the target is $p_{target} = 1 - q^{250}$. If t_s is the time required to grow the target distance d, and t_u is the average time spent in an unsuccessful excursion then the expected time to find the target is: $t_{target} = t_s + t_u/p_{target}$. The values in Figure 2 are approximately 60 times greater than would be expected from our analysis. This could be resolved if the time axis was in seconds, not minutes. However if this is the case, the simulation time to find the target at short distances is below the theoretical minimum.

Even though there was a discrepancy between their theoretical and simulation results, this model showed that dynamic instability is an efficient way for microtubules to search for chromosomes during mitosis. This finding is particularly appropriate to the growth cone where the dynamic population of microtubules continually grow into, and shrink from the growth cone in search of the future direction of growth. The new computational model presented in Chapter 5 is based on this 4 parameter probabilistic model of microtubule dynamics.

4.4 Extensions to the 4 parameter dynamic instability model

In a recent analysis of microtubule dynamics *in vitro* it was suggested that an additional parameter should be included in the above model in order to account for the observed behaviour of microtubules. Odde and Buettner (1995) analysed the dynamics of individual microtubules and the distribution of their growth times. They found that while the slower growing (-) ends obeyed first order catastrophe kinetics (the 4 parameter approach above) the faster growing

(+) microtubule ends may have an effective frequency of catastrophe that depends on how long the microtubules have been growing. Their results suggest that an extra parameter in addition to the four parameters typically used to describe dynamic instability is needed to account for the observed behaviour. They proposed that a microtubule may have built into its mechanism of assembly some form of dependence on its past which will influence its present and future behavior.

The first order (4 parameter) approach results in an exponential probability distribution of microtubule growth times before a catastrophe occurs. If the transitions are not first order the distribution will be non–exponential. The observed distribution of microtubule growth times *in vitro* had a gamma shape (similar to a Gaussian curve skewed to the left), i.e. non-exponential. Physically this means that the lifetime of the microtubule is less likely to be either very short or very long.

To account for this difference it was suggested that the transition from growing to shrinking does not occur in a single step but as a series of three first order transitions. Each of these transitions could potentially represent key chemical or physical events occurring in the microtubule.

The presence of a "memory" within the state of the tubulin in the microtubule cap or of multiple transitions from growing to shrinking has yet to be confirmed. For this reason the computational models presented in Chapter 5 use the traditional 4 parameter model. However the results obtained for the new model are robust to a wide variation in parameter settings and they are unlikely to be significantly affected by the inclusion of this extra transition parameter.

4.5 Thermodynamic models of neurite elongation

The final model discussed in this section is a thermodynamic model for neurite elongation (Buxbaum & Heidemann, 1988) which was later extended (Buxbaum & Heidemann, 1992). In both models axonal elongation is described in terms of the tension exerted on the substrate by the elongating axon. It is assumed that axonal growth occurs at the same rate as microtubule assembly when averaged over time scales of 10–15 minutes (Mitchison & Kirschner, 1988; Gordon-Weeks, 1989). In both models microtubule dynamic instability is ignored as they are simulating axonal microtubules which are stabilized against depolymerization. Microtubule assembly can then be treated as an equilibrium–like process which occurs over longer time scales (Mitchison & Kirschner, 1984a).

In the first model (Buxbaum & Heidemann, 1988) the mechanical axonal tension supported by the substrate is defined as the sum of 3 quantities and surface interactions.

$$Tension = A_a\sigma_a + A_m\sigma_m + A_m\Delta G_m + \text{surface interactions} \qquad (4.3)$$

Where:

- $A_a\sigma_a$is the external force on actin.
- $A_m\sigma_m$ is the external force on microtubules.
- $A_m\Delta G_m$ is the assembly energy of microtubules.

A_a and A_m are the total cross–sectional areas of actin and of microtubules, σ_a and σ_m are the stresses (force/unit area) in actin and in microtubules. ΔG_m is

the energy difference between tubulin in solution and in polymer form. This term could provide extensional energy in axons where no growth–cone motility occurs (Marsh & Letourneau, 1984). However if tubulin and microtubules are in equilibrium, ΔG_m equals zero and the microtubule assembly energy term can be removed. Results from the following biological experiments were then analyzed in terms of the above force–balance equation.

- The treatment of drugs that disrupt actin networks stabilizes neurites to retraction (Joshi et al., 1985). In this case the stress σ_a and cross–sectional area A_a in the actin network is decreased so the overall neurite tension also decreases (Dennerll et al., 1988).

- The chemical phalloidin stimulates actin polymerization with a resulting retraction of the neurite (Joshi et al., 1985). Here neurite tension increases due to the increase in the cross–sectional area of actin A_a.

- Microtubule depolymerization causes retraction of growing neurites (Joshi et al., 1985). Although the microtubule cross–sectional area A_m decreases, the mechanical tension increases as $A_m\sigma_m + A_m\Delta G_m$ are negative quantities (force is positive for tension and negative for compression).

- Taxol–stimulated microtubule assembly causes neurite extension (Joshi et al., 1985; Letourneau, Shattuck, & Ressler, 1987). In this case the total microtubule cross-sectional area A_m increases leading to a decrease in the mechanical tension in the neurite.

The conclusions of the model are that growth cone advance shifts a small amount of tension onto the substratum which relieves some of the compressive force on the microtubules. The critical concentration for microtubule assembly

is thus lowered and tubulin subunits which had previously been in equilibrium with the polymer while supporting the previous tension now add into the polymer until equilibrium compression is again reached (the tensegrity architecture). Experimental results support this theoretical treatment. Under conditions of increased neurite compression an increase in the soluble tubulin pool at the expense of polymerized tubulin is observed (Dennerll et al., 1988).

The later model (Buxbaum & Heidemann, 1992) also simulates how tension controls axonal elongation. Microtubules at the distal end of axons were modelled under compression due to an actin force acting at the microtubule tip (see Figure 4.4). It uses the same complementary force interaction as the previous model, however it assumes that some of the force involved in the forward movement of the growth cone comes from compression of the assembling microtubules. This is consistent with the observations that microtubule assembly alone can drive neurite outgrowth in the absence of a pulling growth cone (Joshi et al., 1985; Letourneau et al., 1987). Again it assumes microtubule assembly can be regarded as an equilibrium–like process at longer time scales (Mitchison & Kirschner, 1984a; Walker, O'Brien, Pryer, Soboeiro, Voter, Erickson, & Salmon, 1988).

The free energy required for microtubule polymerization to take place is greater when a compressive force is applied to the tip of the polymer than when there is no external force. Under compression extra mechanical energy is required both to lift the compressive cap to allow a tubulin dimer to be inserted, and to compress the tubulin dimer once inside the microtubule. These additional mechanical energy terms suppress the assembly reaction. The model predicts that increasing the local concentration of tubulin by tubulin micoinjection or by depolymerizing microtubules in a nearby neurite should strongly favour growth in the remaining neurites. Conversely any

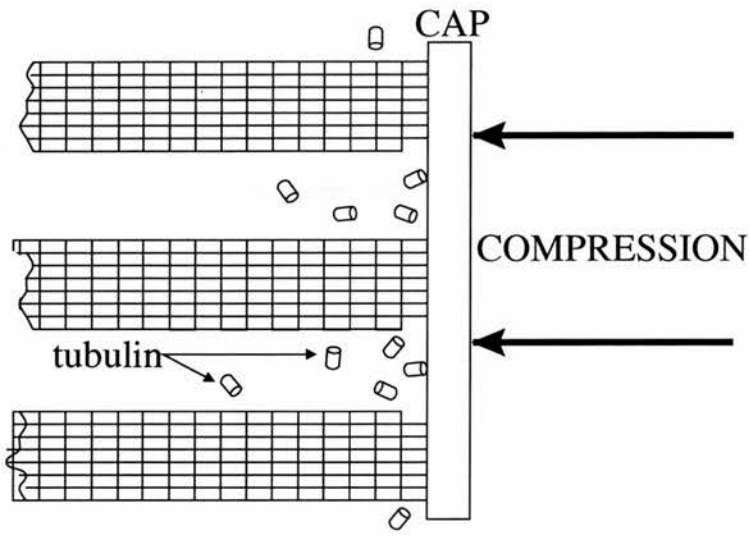

Figure 4.4: Microtubules under compression due to rearward flowing F-actin.

phenomenon that removes tubulin, for example by the addition of a tubulin "getter" such as colchicine, vinblastine or other anti–microtubule drugs is predicted to stop neurite growth or to cause neurite collapse. The results they obtained for elongation of neurites under a varying external force were similar to those achieved experimentally in (Dennerll et al., 1988).

4.6 Summary

The models described in this chapter consider a number of different aspects of microtubule and axonal dynamics over varying time scales. The GTP and Lateral cap models of microtubule lattice dynamics showed theoretically how dynamic instability could occur. The key features of these models were encapsulated by the probabilistic 4 parameter approach used by Holy and Leibler in modelling microtubule dynamics during cell mitosis. In contrast to the chromosomes found by dynamic microtubules during mitosis there is no obvious target for dynamic microtubules in the neuronal growth cone. Furthermore in

the model of mitosis the microtubule rescue frequency was set equal to zero as this resulted in the minimum search time to find the chromosomes. In the growth cone the rescue frequency f_{res} is not equal to 0 (Tanaka & Kirschner, 1991). Dynamic microtubules at the tip of the neurite shaft repeatedly grow into, and shrink from the growth cone where they interact with the rearward flowing F-actin polymer. The values of the dynamic instability parameters will vary throughout the neurite shaft and growth cone depending on the compressive force imposed on the microtubule tip by the rearward flowing F-actin. These tension-compression interactions were included in the models of neurite elongation developed by Buxbaum and Heidemann, however these models ignored the effects of dynamic instability over longer timescales. The effect of both microtubule–F-actin interactions and dynamic instability on neurite elongation are simulated in the new computational models of growth cone dynamics which are discussed in the next chapter.

Chapter 5

The new growth cone simulations

5.1 Introduction

This chapter introduces two new computer models of microtubule dynamics in the growth cone. These extend previous models of microtubule dynamics which neglect the effect of microtubule interactions with one another and with F-actin in the growth cone. The first model presented simulates the effect of microtubule bundling on the rate of axonal elongation. The model shows that small interaction effects between individual microtubules can be amplified within the microtubule bundle to significantly alter the rate of axonal growth. The second model simulates "splayed" behaviour of microtubules (Tanaka & Kirschner, 1991) and the rapid invasion of microtubules into the growth cone following contact with a target cell (Sabry et al., 1991; Lin & Forscher, 1995). The results from analyzing this model suggest that microtubules do not randomly invade the growth cone, supporting the recent view that microtubules play a more active role in pathfinding than previously expected. In both computer models, parameters relating to the dynamics of microtubules that would

be difficult to alter and measure experimentally can be varied easily over a wide range of values. Overall the results suggest that microtubule interactions with F-actin and with other microtubules play a fundamental role in axonal elongation and growth cone turning. Ultimately these interactions determine whether or not the nerve cell ends up making the right target connections.

The new models draw on the previous experimental and theoretical models of growth cone dynamics discussed in Chapter 4. Both models simulate the dynamic properties of microtubules using the four global properties of microtubule dynamic instability (Holy & Leibler, 1994). In the model of Holy and Leibler (1994), the properties of the microtubule dynamics were static for the course of a simulation. The new models extend the dynamic instability model to include interactions between microtubules themselves, and with F-actin. These interactions were not included in the biophysical models of microtubule dynamics which concentrated on reaction mechanisms occurring at the tip of the individual microtubule polymer lattice (e.g. (Hill & Chen, 1984; Bayley et al., 1990)). In the growth cone, the frequency of microtubule catastrophe and rescue transitions exhibit a wide range of continuously changing values. The exact values will depend on the compression of the rearward F–Actin flow at the tips of the microtubules. In the models of Buxbaum and Heidemann (1988,1992) it was assumed that the effect of dynamic instability on axon elongation is negligible for time periods of the order of 15 minutes or greater. In contrast the new models specifically investigate the effect of microtubule dynamic instability on the overall rate of axonal elongation.

The microtubule bundling model predicts that shielding of the compressive rearward F-actin flow rapidly rescues depolymerizing microtubules within the neurite shaft and assists their re-polymerization back into the growth cone. This would ensure that the time that dynamic microtubules spend at the

neurite/growth-cone boundary is maximised. This would allow microtubules undergoing dynamic instability to respond rapidly to subtle changes within the rate of rearward F-actin flow in the growth cone.

In the growth cone turning model it is predicted that in order for microtubules to invade the growth cone in the direction of the target axis, they must preferentially polymerize in the direction of least rearward F-actin flow. It is predicted that random invasion of microtubules into the growth cone is unable to produce the observed microtubule invasion. This model suggests that microtubule dynamic instability behaviour plays a key role in reinforcing growth cone turning behaviour and is not limited to controlling the rate of axonal elongation.

5.2 The New Models

5.2.1 Simulating bundled microtubule behaviour

There are between approximately 10 and 40 microtubules in the average neurite shaft (Tanaka & Kirschner, 1991). Interactions between microtubules mean that the dynamic properties of e.g. 20 tightly bundled microtubules (see Figure 3.1) may be very different from the dynamics of a single microtubule. Figure 5.1(a,b) illustrates two reasons why this is this case.

1. As the tips of leading microtubules share the compressive F-actin load (Buxbaum & Heidemann, 1992), leading microtubules will shield all rearward microtubules by successively reducing the F-actin flow against them (Figure 5.1a).

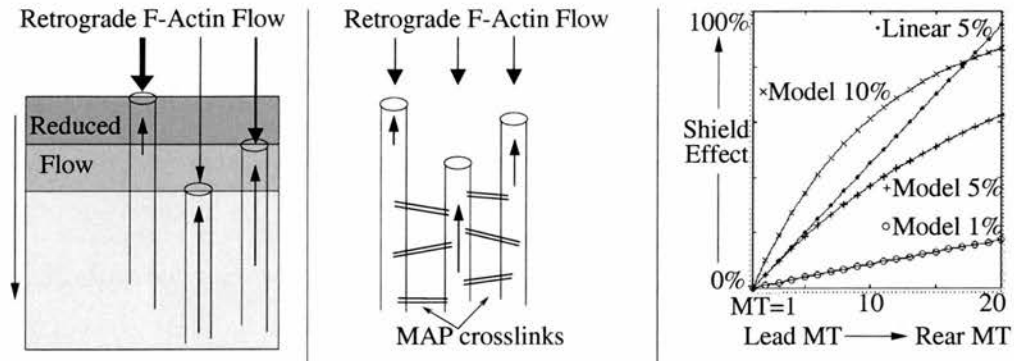

(a) MTs successively reduce F-actin flow

(b) MT Associated Proteins (MAPs) stabilise MTs

(c) Shield effect v MT posn for a bundle of 20 MTs

Figure 5.1: Growth cone interactions which generate microtubule shield effects. (a) Leading microtubules succesively reduce the strength of the opposing flow of F-actin polymer on rearward microtubules. (b) Microtubule associated proteins (MAPs) stabilise rearward microtubules in the bundle from shrinkage by providing crosslinks between neighbouring microtubules. (c) The simulated shield effect for any given MT plotted against its relative position in a bundle of 20 MTs. Values for model shield interactions of 1,5, and 10% are shown alongside a 5% linear shielding interaction.

2. Bundled microtubules are stabilised against shrinkage due to crosslinks formed by microtubule associated proteins (MAPs) (Takemura *et al.*, 1990). MAPs modulate dynamic instability by increasing the rescue frequency, and decreasing the catastrophe frequency of microtubules (Pryer *et al.*, 1992). As a result, microtubules in close proximity are stabilised from shrinking further back into the bundle (Figure 5.1b).

Both interactions generate a successive *shielding effect* on rearward microtubules in the bundle. The strength of this shielding effect will be constantly changing as microtubule dynamic instability results in a terminal tip position which fluctuates rapidly over a period of seconds to minutes. Under these conditions the growth dynamics of the microtubule bundle and consequently the elongation of the axon is not equivalent to the average behaviour of the same number of individual microtubules.

Calculating microtubule velocity

The average velocity V of growth or shrinkage of a microtubule can be calculated as follows. Subtract the average amount lost during shrinkage before a rescue occurs ($V_s T_{res}$) from the average amount gained during growth before a catastrophe ($V_g T_{cat}$), and divide by the total time taken ($T_{cat} + T_{res}$). V_g and V_s are the growth and shrinkage speeds of the microtubule. $T_{cat} = 1/F_{cat}$, and $T_{res} = 1/F_{res}$ are the average lengths of time that a microtubule grows or shrinks before it undergoes a catastrophe or rescue. The average speed of the microtubule is then equal to:

$$V = \frac{V_g T_{cat} - V_s T_{res}}{T_{cat} + T_{res}} \tag{5.1}$$

Using the biological values of microtubule dynamics (Table 3.1 col. 1) gives an elongation rate of 4.66 μm/min. This provides an average value for microtubule outgrowth in a growing neurite. However the analysis which follows is valid under all values of microtubule growth/shrinkage. The new model extends the standard four parameter dynamic instability model to include the favourable dynamics of rearward microtubules due to reductions in F-actin compression and MAP interactions. Starting from the front of the microtubule bundle, the frequency of catastophe/rescue is successively reduced/increased at each rearward microtubule by a *shielding interaction* S. This generates a progressive *shield effect* from the front to the back of the MT bundle. In the simulations the shielding interaction was varied from 0% to 20%. Figure 5.1c shows how the shield effect varies for shielding interaction values of 1, 5 and 10% for a bundle of 20 microtubules. The effect of a linear (step) increase of 5% at each microtubule is also shown. As can be seen from Figure 5.1c the dynamics of the leading microtubule are unchanged whilst rearward microtubules receive the largest shield effect. The average velocity V_{bundle} of a bundle of N microtubules

with shielding interaction S is then given by:

$$V_{bundle} = \sum_{i=1}^{N} \frac{V_g T_{cat}^{(i)} - V_s T_{res}^{(i)}}{T_{cat}^{(i)} + T_{res}^{(i)}} \tag{5.2}$$

This has the same form as the growth of a single microtubule given in equation 5.1. However the average time before a catastrophe or rescue occurs at microtubule i ($T_{cat}^{(i)}, T_{res}^{(i)}$) are now modified by the shield effect S so that:

$$T_{cat}^{(i)} = T_{cat} \div (1-S)^{i-1}, \quad T_{res}^{(i)} = T_{res} \times (1-S)^{i-1} \tag{5.3}$$

For the front microtubule ($i = 1$) the average times before a catastrophe or rescue occurs are the same as before. e.g.

$$T_{cat}^{i=1} = T_{cat} \div (1-S)^{1-1} = T_{cat} \div (1-S)^{0} = T_{cat}$$

For the 2nd lead microtubule ($i = 2$) the time taken before a catastrophe occurs is increased, and the time taken for a rescue is shortened, by a factor of $1 - S$, e.g.

$$T_{res}^{i=2} = T_{res} \times (1-S)^{2-1} = T_{res} \times (1-S)$$

If the shield interaction is 5%, the new time for rescue is 95% of the rescue time of the front microtubule. This shield effect is then propagated from the front to the back of the microtubule array. The effect of including these shielding interactions on the average growth velocity of the microtubule bundle is given in the Results section.

5.3 Computational Details

The code for the simulation was written in C++ on a DEC Alpha UNIX workstation running at 233MHz. Output was written to a data file which was later plotted using Matlab.

The model simulates a 1-dimensional neurite containing N=20 microtubules which are restricted to either grow or shrink along the neurite axis. The number of microtubules was constant throughout the simulation period of 10 minutes. There was no disappearance of existing microtubules or creation of new microtubules. For the purposes of the simulation each microtubule was treated as a single point. The physical location of each microtubule in the bundle was characterised by a single number in an array $x[i]$, i=1 to 20. This represented the net amount of growth/shrinkage that had occurred since the start of the simulation. Initially $x[i] = 0$. If $x[i] > 0$ during the simulation, the microtubule has undergone net polymerization (growth), otherwise it has undergone net depolymerization (shrinkage).

At the start of the simulation the position of each microtubule was randomised by a small amount ($< \pm 0.001 \mu m$) to ensure that no two microtubule positions were identical. This allowed the relative order of each microtubule within the bundle to be calculated from first to last without encountering the problem of microtubules with identical positions.

At the start of the simulation the probability that an individual microtubule is growing was $P_{growth} = \frac{T_{cat}}{T_{cat}+T_{res}}$ = the average time spent growing divided by the average time for 1 complete growth/shrinkage cycle. A random number $R(0:1)$ was chosen. If $R > P_{growth}$ the microtubule grows initially, otherwise

it shrinks. This helps to eliminate any start up effects caused by growing the microtubules from the same start position.

At each 1s timestep the position of each microtubule in the bundle was calculated. The microtubule with the highest position value at any given time during the simulation was labelled as the lead microtubule (MT_1). The shielding effect on each rearward microtubule was then calculated according to equation 5.3 , e.g for a 5% shield effect the dynamic instability characteristics of the 2nd lead microtubule (MT_2) were modified in the following way:
$F_{cat(MT_2)} = 105\%$ of $F_{cat(MT_1)}$ $F_{res(MT_2)} = 95\%$ of $F_{res(MT1)}$
This was then repeated for each rearward microtubule in the bundle such that
$F_{cat(MT_{n+1})} = 105\%$ of $F_{cat(MT_n)}$ $F_{res(MT_{n+1})} = 95\%$ of $F_{res(MT_n)}$

At each timestep a random number R(0:1) was chosen for each individual microtubule within the bundle to determine whether the microtubule would continue to grow, shrink or undergo a transition between the two states. For F_{cat}=0.72, the probability that a growing microtubule undergoes a catastrophe in a 1s timestep is $P_{cat} = \frac{0.72}{60} = 0.012$, and $P_{res} = \frac{1.74}{60} = 0.029$. If $R > P_{cat}$ then the microtubule continues to grow. The length grown by a microtubule in 1s ($\frac{10.5\mu m}{60}$) is then added to the microtubule's position. Otherwise the microtubule would start to shrink. In a similar manner, a shrinking microtubule would either continue to shrink or undergo a rescue transition. The model simulated 10 minutes of microtubule growth.

Summary

The following sequence summarizes the computational process for the bundling simulation.

1. At t=0 initialise microtubule positions and direction of growth.
2. At each 1s timestep calculate order of microtubules within the bundle from front to back.
3. Calculate shield effect for each individual microtubule.
4. Adjust F_{cat},F_{res} for each microtubule according to shielding effect.
5. Calculate probability of catastrophe/rescue within next timestep.
6. Choose random number R(0:1). If $R > P_{transition}$, microtubule continues to grow/shrink. Increase/decrease microtubule length. Otherwise if $R < P_{transition}$ reverse direction of growth/shrinkage.
7. Update time (t=t+1) and go to 2. Stop if t=600s.

The position of individual microtubules are plotted in Figure 5.3(a)-(c) for no shielding (0%), 1% and 5% shielding. Due to the random nature of microtubule dynamic instability, the microtubules undergo transitions at different times. This alters the order of the microtubules within the bundle which determines the amount of shielding received by each microtubule. This accounts for the spread of positions observed in Figure 5.3(a)-(c). The effect of shielding on overall growth is plotted in Figure 5.4.

5.3.1 Simulating microtubule branch invasion and growth cone turning.

This section analyses the effect of interactions between microtubules and F-actin on growth cone turning. The model simulates microtubule invasion of

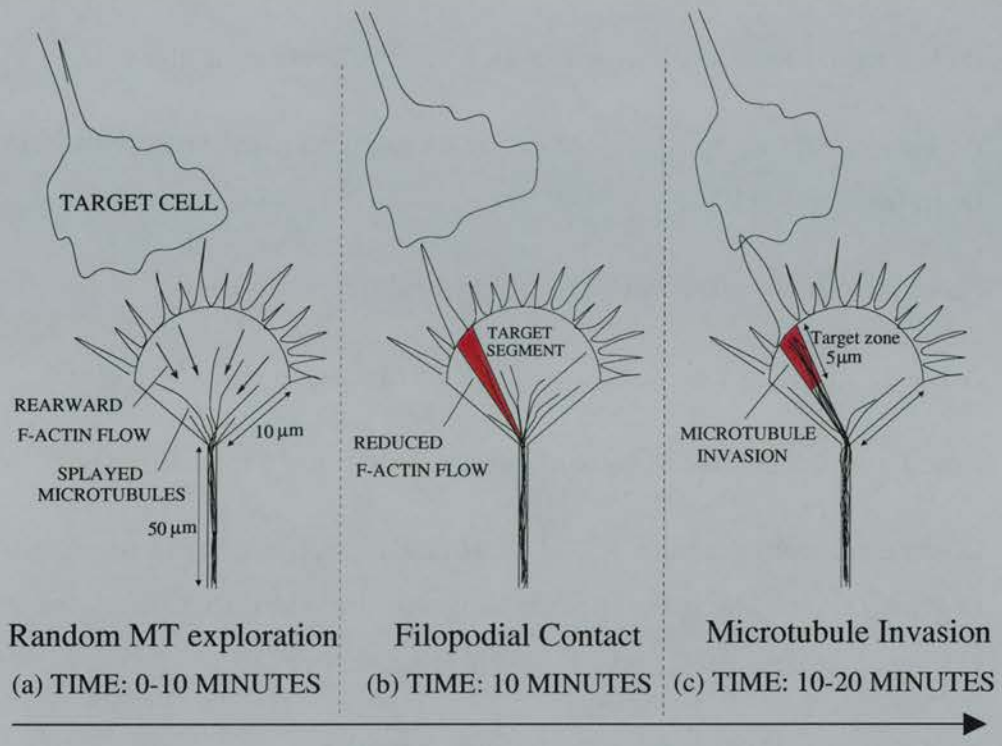

Figure 5.2: The sequence of events simulated by the growth cone model. (a) Random filopodial and microtubule behaviour. (b) Contact with target cell leads to reduced F-actin flow in target segment. (c) Rapid microtubule invasion of target segment.

a growth cone segment following contact with a target cell (Lin & Forscher, 1995).

The sequence of events simulated by the model is shown in Figure 5.2(a-c). The growth cone model consists of a 1-dimensional axon of length 50μm ending in a 10μm growth cone of angular width 100 degrees. At the start of the simulation, 20 microtubules each 50μm long grow from the base of the growth cone. Initially filopodia undergo random excursions with microtubules displaying random "splayed" behaviour (Figure 5.2a). The filopodia projections are not modelled explicitly in the simulation. The rearward F-actin flow has a uniform value throughout the growth cone (Lin & Forscher, 1995) which affects the microtubule dynamics. At each 1 second time step, the microtubule may undergo a random transition based on its current catastrophe and rescue

frequencies. All microtubules grow straight forward in the axon and are given a fixed random direction each time they enter the growth cone. Shrinking microtubules are rescued if their length falls below 1μm. Initially the simulation runs for 10 minutes to eliminate start up effects.

After 10 minutes a filopodia encounter with a target cell is simulated (Figure 5.2b). In the model, the value of the rearward F-actin flow in a 5 degree target segment is reduced by 30% of its original value (giving a microtubule a 5% chance of entering the segment randomly). This was the smallest reduction in value seen to occur in growth cone - target cell encounters (Lin & Forscher, 1995) and provides the most difficult conditions for microtubules to enter the segment. The reduction in F–actin flow reduces the compressive load at the tip of a growing or shrinking microtubule in this region. As a result, microtubules already present in this segment, or which subsequently enter it have dynamic properties enhanced by 30% from the rest of the growth cone. After 20 minutes the number of microtubules further than 5μm into the target segment (the *target zone*) is counted (Figure 5.2c).

In the first set of simulations, microtubules entered the growth cone from the neurite shaft in a random direction. This modelled splayed microtubule behaviour where the microtubules appear randomly spread throughout the growth cone (Tanaka & Kirschner, 1991). The aim of these simulations was to test whether the random exploration of microtubules into the growth cone was sufficient to allow large numbers of microtubules to invade the target zone.

The second set of simulations investigated how the number of microtubules invading the target zone is altered when the microtubules specifically enter the growth cone in the direction of the least rearward F-actin flow (in this case into the target segment itself). This modelled the behaviour seen following contact

with a target cell (Lin & Forscher, 1995). This behaviour may also occur during growth cone turning as microtubules have been seen to invade the growth cone branch which later becomes the axon before any visible signs of turning (Tanaka & Kirschner, 1991).

Both sets of simulations investigated how the numbers of microtubules invading the target zone changed when:

1. The probability of microtubule rescue in the neurite shaft was double the value in the growth cone and that for the catastrophe rescue was halved. This simulated the lack of rearward F-actin flow in the neurite shaft.

2. The rearward flow of F-actin in the target segment was reduced by 90% instead of 30%. In some growth cone - target cell encounters, the rearward F-actin flow is almost stationary (Lin & Forscher, 1995).

3. Shielding interactions of 1% or 10% were applied (the default was 0%). This simulates the stabilizing effects of MAP crosslinking between microtubules discussed above. As the crosslinks are short range, shielding was limited to the shorter of 2 microtubules which grew with less than 1 degree separating their directions. This included all microtubules in the neurite shaft.

The first condition favors a rapid turnaround of shrinking microtubules in the neurite shaft. This enables the microtubules to sample the growth cone more frequently and they are thus more likely to end up in the target segment. In the second condition there is a greater probability that microtubules which have entered the target segment are able to remain there without shrinking back into the neurite shaft. As a result it is more likely that there are microtubules within

this segment than elsewhere in the growth cone. The inclusion of shielding interactions increases the probability that rearward microtubules will grow into the target segment if other microtubules have already invaded this segment. With these three conditions on, the microtubules are more likely to invade the target segment and be located in the target zone at the end of the simulation.

5.4 Computational Details

The model simulates a 1-dimensional neurite of length $50\mu m$ and a 2-dimensional growth cone of length $10\mu m$ and angular width 100^o. Initially 20 microtubules of length $50\mu m$ grow out from the tip of the neurite shaft. The treatment of microtubules in the branch invasion model is similar to that of the bundling model with the following differences.

- The boundary between the neurite shaft and growth cone has a position value of 0. Initially the base of the microtubule is at position -50μm, and the tip at position 0. If a microtubule grows from the neurite shaft into the growth cone it is given a random direction between $\pm 100^o$. This direction remains fixed for the duration of time that the microtubule remains in the growth cone.
- Microtubules within the neurite shaft have a growth direction of 0^o.
- Microtubules which grew $> 10\mu m$ within the growth cone were limited by the edge of the growth cone membrane until they underwent a catastrophe.
- Microtubules which shrunk to a length of $< 1\mu m$ (below a position of -49μm) underwent a transition from shrinkage to growth.

- The simulation is run for 10 minutes to eliminate start up effects. After 10 minutes the value of the rearward flow in the target segment is decreased by either 30% or 90%. This increases/decreases the time until a catastrophe/rescue occurs by 30% or 90%.
- Microtubule shielding was as described in the bundling model with the addition that shielding was limited to microtubules whose direction of growth was separated by less than 1^o. All rearward microtubules in the neurite shaft were shielded by forward microtubules.
- The position and dynamic instability parameters of the microtubules were calculated at every 1s time interval.
- With the neurite shielding condition on, the probability of catastrophe/rescue within the neurite shaft was halved/doubled. The values of T_{cat}, F_{cat} were adjusted accordingly.
- After 20 minutes of simulation the number of microtubules in the target zone were counted.

The results from the various simulations are plotted in Figures 5.5-5.7. The results were plotted over a wide range of catastrophe and rescue parameters to test the sensitivity of the model to a range of possible biological values.

5.5 Results

5.5.1 Effect of microtubule interactions on axonal growth.

The characteristic "sawtooth" plots of the position of the microtubule tips during 10 minutes of simulated growth are plotted in Figure 5.3(a-c). The mi-

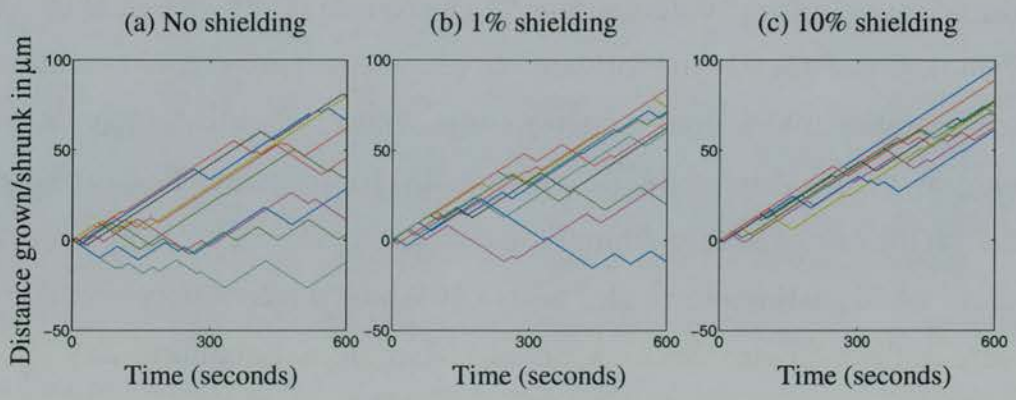

Figure 5.3: The figures show the characteristic sawtooth plots of microtubule tip position with time obtained with 10 bundled microtubules. Each individual microtubule in the bundle is plotted with a different colour. (a) No shielding (b) 1% Shielding (c) 10% Shielding

crotubules have the dynamics shown in column 1 of Table 3.1 and grow on average $46\mu m$ in this time. Figure 5.3a shows the growth of individual microtubules with no shielding. There is a large variation in the distance between the leading microtubule which has elongated by $80\mu m$ and the most rearward microtubule which has shrunk by $20\mu m$. Only 4/10 microtubules have elongated more than 50μm. Figure 5.3b plots the position of 10 bundled microtubules which now have 1% shield interactions. The final positions are still spread out although due to the shielding interactions 7/10 microtubules have now extended more than $50\mu m$. The effect of 10% shielding is more apparent in Figure 5.3c. All microtubules have now grown over $50\mu m$. It can also be seen that when the leading microtubules undergo a catastrophe they are rescued more quickly than before due to the greater effects of shielding at the rear of the bundle. As a result the microtubules move forward as a single bundle.

Figure 5.4 shows that for a bundle of 20 microtubules a shielding interaction of only 1% at each microtubule leads to an increase of 16% in the forward movement of the bundle compared to the rate of growth of individual microtubules ($4.66 \rightarrow 5.41\mu$m/min). With a 10% shielding interaction, 20 bun-

dled microtubules nearly double their forward rate of movement (4.66→8.81 μm/min). Consequently the forward movement of an axon could result from the co-operative interaction of microtubules which individually have a much lower growth rate. A microtubule with growth characteristics T_{cat}=1.0, T_{res}=2.3 shrinks at the rate of 3.55μm/min (Equation 5.1). However an axon containing a bundle of 20 such microtubules with a 10% shield interaction would move forward at the biological average rate of 4.66μm/min (Equation 5.2).

The validity of these results is not dependent on the precise form of the shielding model presented here. For small interaction values the shield effect increases linearly from the front to the rear of the MT bundle (see the 1% interaction curve in Figure 5.1). For larger interaction values a linear increase generates a greater shield effect (and thus a higher growth rate) than the curve generated by the model (e.g. the 5% linear plot in Figure 5.1). The results seen in Figure 5.4 would be qualitatively similar for any mechanism which results in increased shielding for rearward MTs. Thus small changes in the strength of interactions between individual microtubules may have a large effect on the behaviour of the growth cone as a whole. The shielding mechanism effectively increases the forward rate of microtubule and axonal growth. It also results in energy efficiency savings for the cell as a lower concentration of non-polymerized tubulin is able to produce the same overall growth rate. A further advantage of the microtubule shielding effect on growth cone motility is discussed below.

5.5.2 Effect of interactions on microtubule branch invasion.

Figures 5.5, 5.6 and 5.7 show the results obtained for random microtubule invasion of the growth cone, flow directed invasion and with shielding interactions

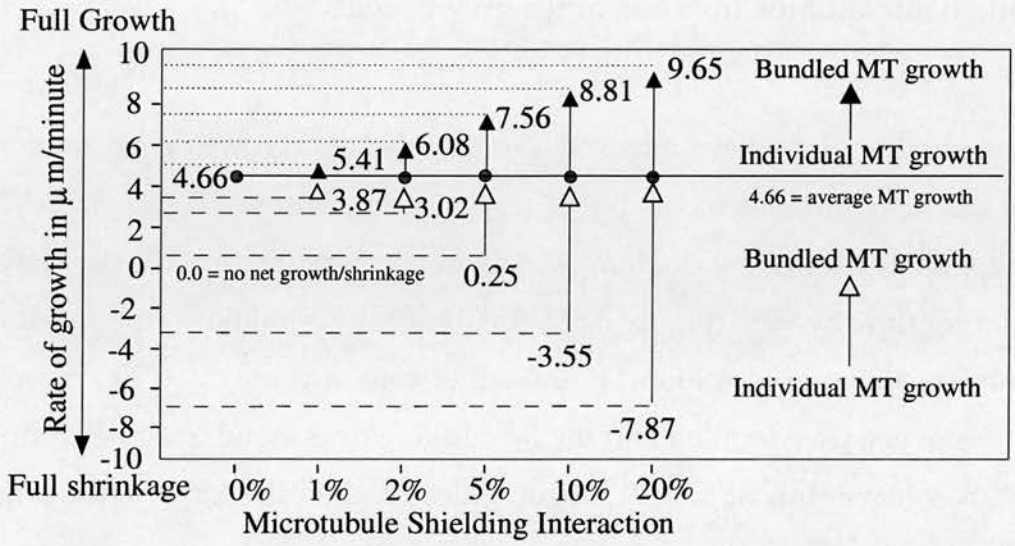

Figure 5.4: Effects of microtubule shielding interactions on growth. Filled arrows: a single microtubule with the dynamic instability parameters given in Table 3.1 moves forward at the average rate of 4.66 μm/min (Equation 5.1). With a shield interaction of only 1% the growth of a bundle of 20 of these microtubules would be increased by over 16% from 4.66 to 5.41 μm/min (Equation 5.2). The unfilled arrows show what shield interaction is required for the **bundle** to grow forward at 4.66 μm: e.g. with a 10% shield interaction a bundle of 20 microtubules moves forward at the rate of 4.66μm/min although the microtubules would individually shrink at a rate of 3.55 μm/min.

---

respectively. Each graph plots the number of microtubules in the target zone 10 minutes after the target was encountered. In each simulation the catastrophe and rescue frequencies are varied from 0.1 to 5.0 transitions/min in steps of 0.1. Each point is the average of 50 trials. Unless otherwise specified, the default settings in each simulation are: 20 microtubules with normal axon recovery, and a 30% reduction in F-actin flow in the target zone. In the graphs, the cross (+) shows the average microtubule catastrophe/rescue frequency in the growth cone (0.72,1.74 transitions/min) (Tanaka & Kirschner, 1991). The rectangle (▭) includes the range of microtubule rates obtained from cell extracts during interphase (Belmont, Hyman, Sawin, & Mitchison, 1990).

Random microtubule invasion of the growth cone.

In the simulations where microtubules invaded the growth cone randomly very few microtubules were able to reach the target zone (Figure 5.5a). This result was unaffected by doubling the axon recovery (Figure 5.5b) or slowing the target flow by 90% (Figure 5.5c). In all of these situations, the maximum number of microtubules found in the target zone was only 2.9/20. When the axon recovery was doubled and the F-actin flow was simultaneously reduced by 90% a maximum of 6.4/20 microtubules reached the target zone (Figure 5.5d).

Flow directed microtubule invasion of the growth cone.

In contrast flow directed microtubules invaded the target segment in large numbers with a maximum of 12.2/20 microtubules reaching the target zone 10 minutes after the target was encountered (Figure 5.6a). Reducing the F-actin flow in the target segment by 90% or doubling the axon recovery increased the maximum number of microtubules reaching the target zone to over 15/20 (Figures 5.6 b,c). Simultaneously reducing the target F-actin flow and increasing axon recovery allowed all 20 microtubules to reach the target zone for certain pairings of catastrophe/rescue parameter values (Figure 5.6d).

Simulations including shield interactions.

The results for the random simulations with default parameters changed little when shielding interactions of either 1% or 10% were applied (Figures 5.7 a,b).

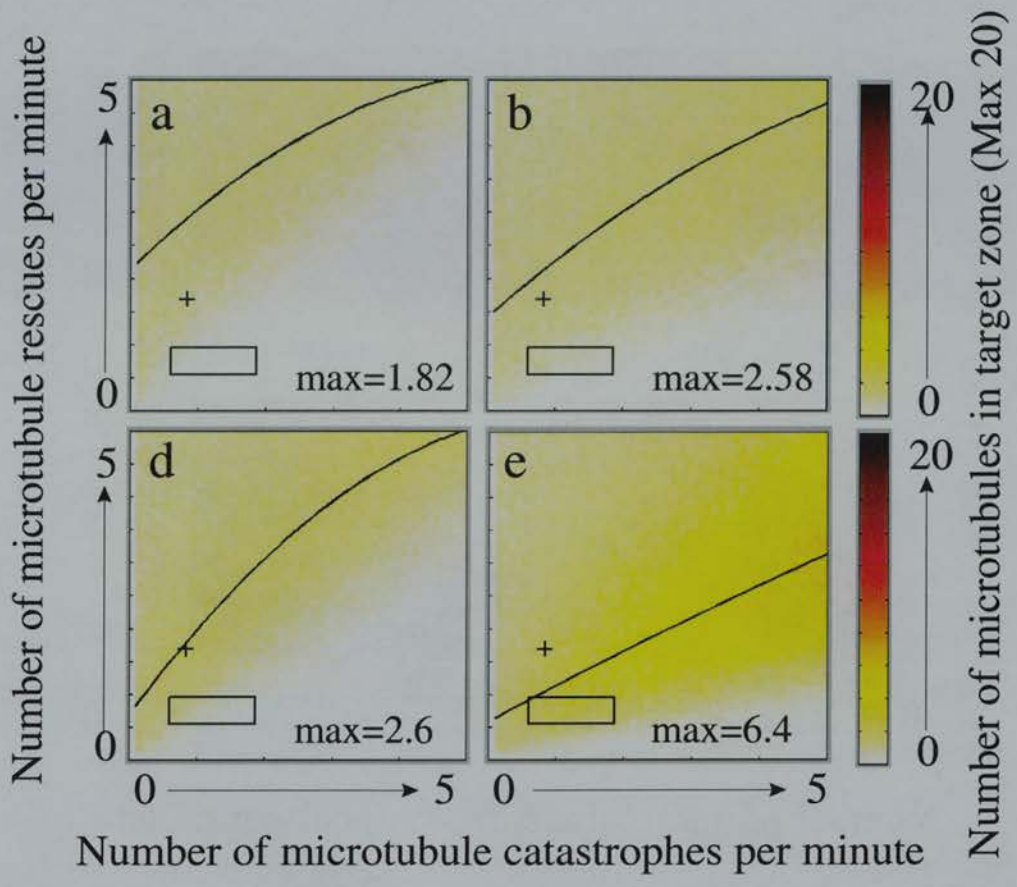

Figure 5.5: Simulation results of randomly directed microtubule invasion of growth cone. Type of Simulation: Random (a) default, (b) axon recovery on, (c) reduced target flow, (d) axon recovery on and reduced target flow. The plots show how many of the 20 microtubules reach the target zone 10 minutes after simulated growth cone contact with a target cell. Each graph point represents a single pair of catastrophe/rescue frequencies averaged over 50 trials. Experimental values of microtubule catastrophe/frequency transitions are plotted from (Tanaka & Kirschner, 1991) (+) and (Belmont et al., 1990) (▭). The curve shows the maximum number of microtubules reaching the target zone at each catastrophe frequency.

This only increased the number of microtubules entering the target zone from 1.8/20 to a maximum of 2.9/20.

In contrast, applying a 1% shield interaction in the flow directed simulations increased the maximum number of microtubules in the target zone by over 24% (from 12.3/20 to 15.2/20) (Figure 5.7c). Finally a 10% shield interaction

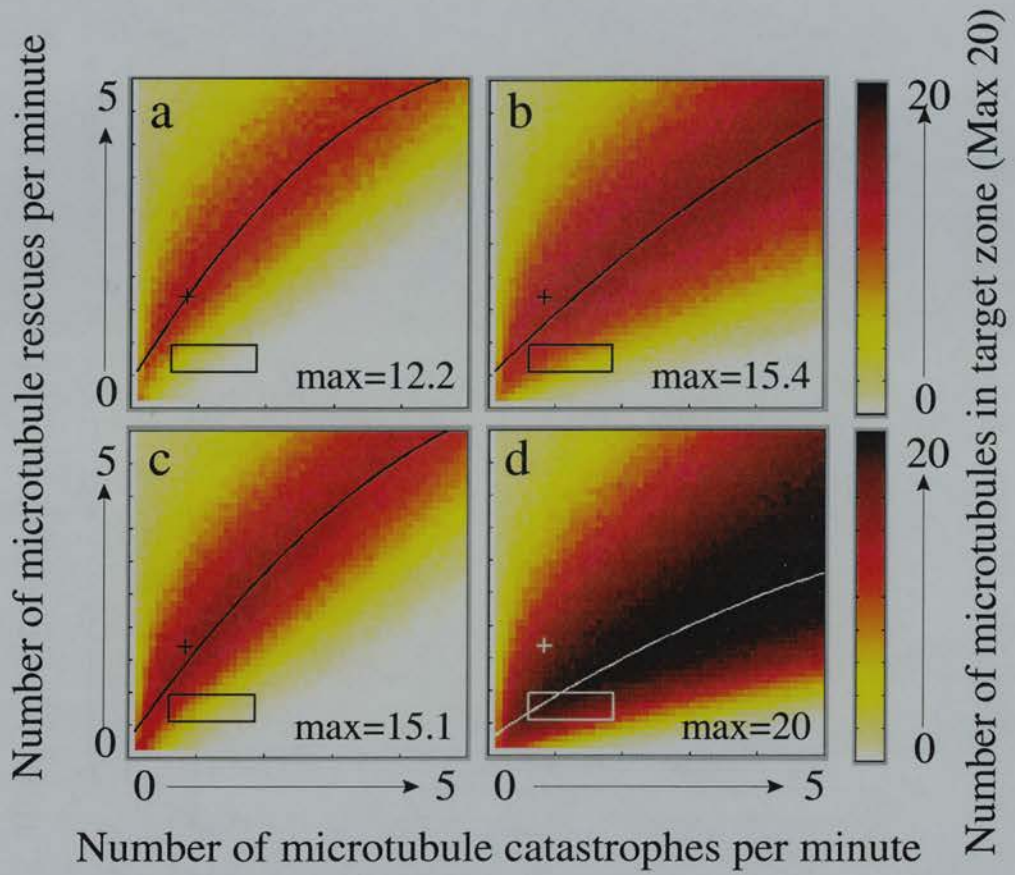

Figure 5.6: Simulation results of flow directed microtubule invasion of growth cone. Type of Simulation: Flow Directed: (a) default. (b) axon recovery on. (c) reduced target flow. (d) axon recovery on and reduced target flow.

allowed all 20 microtubules to reach the target zone for some values of the catastophe/rescue pairings (Figure 5.7d).

Holy and Leibler (1994) showed that dynamic instability provides a better mechanism for searching the environment than other polymer kinetics. For flow-directed microtubules, shielding interaction effects improve the efficiency of this search by increasing the frequency of microtubule invasions into the growth cone. This reduces the numbers of very short and very long microtubules which are unable to reach the target zone.

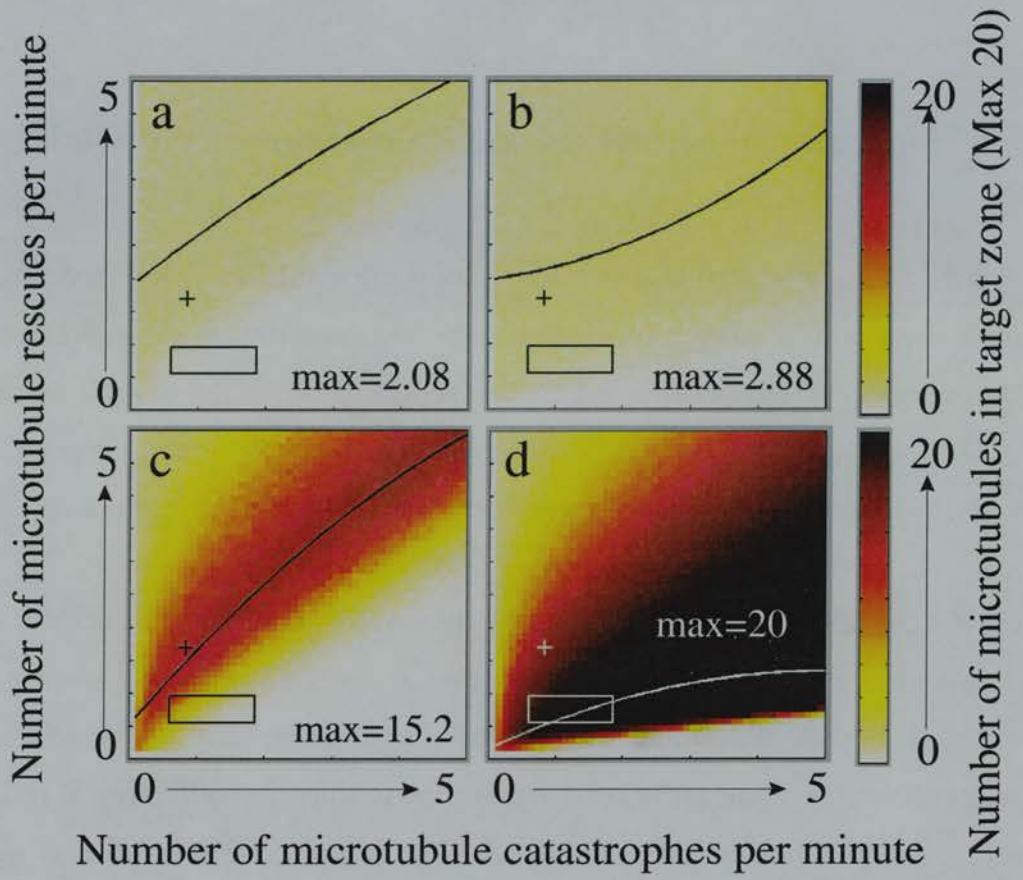

Figure 5.7: Results of microtubule invasion of growth cone including shielding interactions. Type of Simulation: (a) Random: 1% shielding. (b) Random: 10% shielding. (c) Flow Directed: 1% shielding (d) Flow Directed: 10% shielding.

It can be seen from the flow directed graphs that a wide range of pairs of catastrophe/rescue values allow a high number of microtubules to reach the target zone. Also the curve showing the maximum number of microtubules found in the target zone for each value of the catastrophe frequency does not vary greatly throughout the tests. The important characteristic is the ratio of the catastrophe:rescue frequencies and not their absolute values.

5.6 Discussion and Analysis

5.6.1 Strengths, Weaknesses and Predictions of the Models

Both models suggest that interactions among microtubules and F-actin in the growth cone play a more important role in neuronal pathfinding than previously expected (Yamada, Spooner, & Wessells, 1970). As the overall assumptions behind the two models are similar, the general analysis will refer to both models. When individual differences occur these will be highlighted.

These are the first models to simulate the dynamic interactions of microtubules with F-actin and other microtubules within the neurite shaft and growth cone. The models highlight possible interactions affecting microtubules which could significantly alter their individual dynamics within the cell. The bundling model predicts that the rate of recovery of dynamic microtubules is faster within the neurite shaft where there are less compressive forces due to F-actin and an increased probability of stabilizing MAP crosslinks. The model also predicts that bundled microtubules in the neurite shaft and the central zone of the growth cone will have more favourable dynamic properties (faster recovery and longer catastrophe times) than in the peripheral zone. Due to the imaging difficulties of tracking microtubules within the bundle, this has not yet been verified. However this may well be feasible within the near future. The model also predicts that larger neurites with a greater number of microtubules may be able to grow faster than smaller neurites under the same experimental conditions due to an increased shielding effect.

The model of microtubule bundling shows that interactions between microtubules may allow forward growth of the axon when individual microtubules

would shrink. This prediction could be confirmed by analysis of the individual microtubule dynamics within the neurite shaft and growth cone during axonal extension. The proposed shielding interactions may be either mechanical, as a result of a decrease in the compressive rearward F-actin flow, or chemical as a result of MAP interactions between nearby microtubules, or both. Such interactions may ensure that an axon containing bundled microtubules continues to elongate through regions which the growth cone would be unable to cross if the microtubules did not act co-operatively. Individual microtubules would only be able to elongate in off-axis directions if they were dynamically favourable, e.g. due to reduced F-actin flow in that region.

One assumption of the bundling model is that it assumes that microtubule shielding is uniform throughout both the lateral and vertical (Y and Z-dimensions) and that shielding only varies with the length co-ordinate (X-dimension) of the microtubule. It is likely that the neurite shaft will not necessarily be homogenous within the Y- and Z- dimensions. At present it is not clear what effect interactions between microtubules and the membrane/substrate will have on microtubule outgrowth. It is also not clear whether pockets exist within the growth cone which favor microtubule outgrowth compared to other areas of the neurite shaft. The answers to these questions may be resolved with improvements in imaging *in vivo* microtubules. I am not currently aware that any such domains have been found although it is possible that they have not been looked for.

During the bundling simulation it was assumed that the microtubles were of sufficient length that they would not depolymerize to zero length. As the maximum distance shrunk by any microtubule in the simulations was $\approx 30\mu m$ this assumes a starting length, L $\geq$ 30 μm. Small changes to the numbers of microtubules within the neurite shaft due to either complete depolymerization of

existing microtubules or creation of new microtubules should not significantly alter the overall shielding effect. It is possible that shielding does not have an effect only on existing microtubules, but may also increase the number of new microtubules which are created from seed sites. The model predicts that the highest number of newly created microtubules would be found further back within the neurite shaft where the shielding effect is highest.

Both models do not simulate the concentration of tubulin as it is assumed that there is a large pool of unpolymerised tubulin which is available to dynamic microtubules both within the neurite shaft and growth cone (Mitchison & Kirschner, 1987). This assumption may be invalid at the extreme peripheries of the growth cone, or deep within the neurite shaft where there may be a decrease in the amount of available tubulin (no localized variations in tubulin concentration have been observed within the growth cone itself (Mitchison & Kirschner, 1987). In model simulations using biologically plausible values of the catastrophe and rescue frequencies the microtubules were generally confined within the boundaries of the model space and away from the edges. Any edge effect for either leading or rearward microtubules due to a decrease/increase in tubulin availability is unlikely to significantly affect the results of the models which were stable over a wide range of different transition frequencies.

5.6.2 Analysis of the branch invasion model

The branch invasion model predicts that microtubule invasion into the growth cone following contact with a target cell cannot occur unless microtubules actively interact with F-actin to extend in the direction of least rearward F-actin flow. Neither a 90% reduction in the F-actin flow in the target, increased axon

recovery, nor shielding interactions enabled the majority of microtubules to reach the target zone if they invaded the growth cone randomly. Intuitively it can be seen why this will be the case for dynamic microtubules in the biological growth cone. The position of the microtubule tip fluctuates around the central zone with zero net growth or shrinkage. Microtubules with these characteristics are unlikely to reach the target zone before they undergo a catastrophe. Combined with the small probability of growing in the target direction, microtubules randomly sampling the growth cone are unable to reach the target zone. The model predicts that in order to maximise growth cone motility, microtubules do not explore the growth cone randomly. Instead as a result of interactions with F-actin, microtubules invade the growth cone in the direction of least F-actin flow. In order to test this prediction the dynamics of individual microtubules would need to be monitored during growth cone encounters with a target cell. Microtubules may simply extend in the direction of least F-actin flow due to physical constraints imposed at the microtubule tip when it extends into the growth cone. Alternatively some as yet unknown microtubule/F-actin interaction mediated by MAPs may guide the microtubules in the direction of least F-actin flow.

The branch invasion model has primarily the same assumptions and weaknesses as the bundling model. Both models ignore the effect of calcium on the polymerization state of the microtubules. Localized increases in calcium concentration within the growth cone (see Chapter 6) will affect the dynamic instability characteristics of the microtubules. It is known that secondary messengers such as cAMP affect the turning behaviour of the growth cone towards the same external signal, e.g. BDNF can have either an attractive or repulsive effect on the growth cone (Song, Ming, & Poo, 1997). In order to model this it would be necessary to include the effect of BDNF on both calcium dynamics and secondary calcium pathways. A simulation of this type would require a

greater level of complexity than is present in the current model.

An additional assumption of the branch invasion model is that there is only one target direction within the growth cone which is favoured. This simulates the change in the rearward flow of F-actin which is seen during growth-cone target encounters (Lin & Forscher, 1995). However it does not predict how microtubule behaviour would be affected if there was more than one favourable direction of growth, e.g. during growth cone contact with more than one target cell, or during growth up a gradient of neurotrophic factor. In these instances multiple directions of growth may be favourable due to reduced F-actin flow throughout the growth cone. The following proposed experiment may be able to answer this question. The rearward flow of F-actin should be monitored during a growth cone encounter with two (or more) target cells. In such an encounter it is possible that the rearward flow of F-actin is reduced by 60% in one direction and only 30% in a different direction. Under these conditions it is not clear which of the following outcomes is more likely to occur.

1. All microtubules invade the direction with the 60% reduction in rearward F-actin flow as this is the most energetically favorable.
2. Microtubules invade the 60% and 30% directions in a ratio of 2:1 as the 60% segment is able to capture the majority of the microtubules but not all of them.
3. Microtubules simply invade the nearest segment which has a reduced F-actin flow as both segments are energetically favorable.
4. None of the above.

It is likely that the results from this experiment would be able to answer many of the questions regarding the nature of the interaction between microtubules

and F-actin which are not solved by this model. The experiment could also provide clues as to how the growth cone is able to grow in the maximal direction of a broad extracellular signal, such as a gradient of neurotrophin, without splitting into multiple branches.

In the simulation of microtubule invasion of the growth cone, the filopodia encounter with the target cell was not explicitly modelled. Instead the effect on the microtubules was simulated by providing more favourable growth dynamics due to the reduction in F-actin flow that would result on contacting the target cell. Filopodial contact with target cells, or extracellular signals such as neurotrophins, may also result in a stabilization of the microtubule within the growth cone. This could provide a scaffold which would guide the invasion of rearward microtubules along the direction of the target axis. In the simulations, this would increase the number of microtubules which are found in the target zone. It is unlikely that this would significantly affect the predictions made by the model. The simulations in which rearward F-actin flow was reduced by 90% within the target zone has a similar effect to a complete stabilization of the microtubules within this area. Even with this condition on, microtubules wre unable to invade along the target-axis if they entered the growth cone randomly. The prediction that microtubules preferentially enter the target segment is not affected by the way in which microtubules enter this zone. Either a shielding mechanism which favours dynamic instability conditions at the tip of the microtubule, or a scaffold mechanism which stabilizes microtubules aligned along the target axis are possible candidates for the observed microtubule invasion into the growth cone.

5.6.3 Conclusion

The combined results of both models suggest that short-term microtubule shielding interactions between neighbouring microtubules and with F-actin have a significant long term effect on growth cone behaviour. Although such shielding interactions may exist for only a few seconds, they would result in both energy efficient axonal elongation and an increased growth cone motility.

The next chapter introduces a new model which simulates the dynamics of growth cone filopodia. The model provides an explanation for how filopodia might be created at the edge of the growth cone membrane, and what could cause them to undergo periods of growth and shrinkage.

Chapter 6

A Simulation of Growth Cone Filopodia Dynamics

6.1 Introduction

The models of the previous section concentrated on the dynamics of microtubules which are important in axonal elongation and in supporting growth cone turning. The present chapter introduces a model of the dynamics of growth cone **filopodia**. Filopodia are long, thin structures which are created at the tip of the growth cone membrane (Figure 6.1). The filopodia act as antennae and are able to transduce signals in the external environment due to e.g. adhesion channels or neurotrophin gradients, into internal signals which alter the stability of the F-actin and microtubule network. This in turn will alter the speed and direction of neurite outgrowth. When a filopodia makes contact with an external guidepost cell, it remodels itself to become the leading tip of the developing neurite and a new growth cone will form around it

(Broadie et al., 1993). Thus filopodia are essential in the proper functioning of growth cone navigation. However the exact causes of filopodial excursions are unknown . Experimental work by Davenport and Kater (1992) has linked filopodial outgrowth to the local concentration of calcium. Calcium has previously been proposed as a morphogen regulating neuronal dendrite growth in a computational model of cell development (Hentschel, 1994).

In this chapter I describe a model based on the hypothesis that calcium could act as a morphogen to directly regulate the pattern of filopodial outgrowth and subsequent retraction. This is the first model to simulate the causes of the "random and spontaneous" excursions of neurite growth cone filopodia directly rather than to generate them stochastically. The model uses a reaction-diffusion system of equations similar to the one developed by Alan Turing (Turing, 1952). Turing was the first person to formulate a mathematical basis for "**morphogenesis**" - a model describing pattern formation. He showed how two diffusing chemicals (often called an activator and an inhibitor) could react to form distinctive patterns. In the new model of filopodia dynamics, calcium acts as an activator whilst cyclic AMP (cAMP) acts as an inhibitor. This system creates an intracellular distribution of calcium which can vary both spatially and temporally. Under certain conditions the reaction-diffuson system can generate hotspots of increased activity in localised areas. Changes in the local concentration of calcium will affect the local adhesion of the F-actin network to the substrate and could result in both filopodial outgrowth and shrinkage. In principle this mechanism could account for both the spontaneous creation of filopodia and their subsequent behaviour. The Turing reaction-diffusion system used in the simulations can also generate a wide variety of other spatial and temporal patterns which could control other growth cone behaviours . The aim of the simulations was to show that a Turing like reaction-diffusion system with calcium as an activator, and cAMP as an inhibitor, could produce

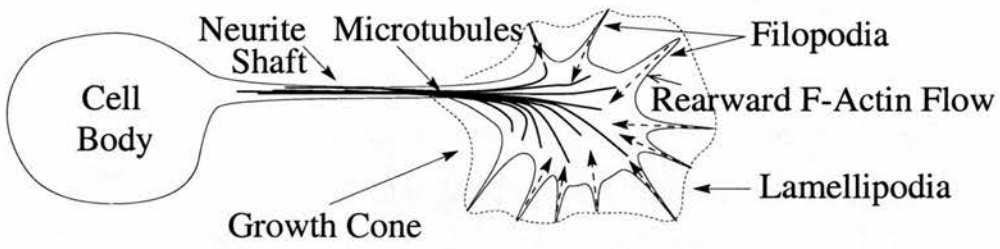

Figure 6.1: The growth cone including filopodia.

spatial and temporal patterns which might underly filopodial extension and retraction.

Recent experimental work by Song et al. (1997) has confirmed that cAMP has an important role in modifying the behaviour of the growth cone towards extracellular stimuli. In their experiment, the behaviour of the growth cone did not simply depend on the extracellular signal, but on the state of cAMP activity within the growth cone. The current model predicts that cAMP exerts its action by modifying the levels of intracellular calcium which will have a direct affect on F-actin and microtubule dynamics.

The results of the model suggest that a Turing-like system *could* underly the observed dynamical behaviour of filopodia and the growth cone in response to environmental stimuli. However the overall conclusion from the model is that this reaction system is only one of a number of possible schemes which could generate filopodia-like behaviour. With hindsight, a Turing-like dynamical system may not be the most appropriate framework with which to model growth cone dynamics. However analysis of the model is still able to give insights into the nature of the underlying cellular dynamics governing filopodial dynamics and growth cone behaviour. These are discussed in more detail after the next section which introduces reaction-diffusion systems and Turing patterns.

6.2 Turing Patterns

The mathematics of patterns due to two or more diffusive chemicals were made explicit by Alan Turing (Turing, 1952). He stated:

> It is suggested that a system of chemical substances, called morphogens, reacting together and diffusing through a tissue, is adequate to account for the main phenomena of morphogenesis.

Turing patterns can occur when two (or more) chemicals diffuse and interact . The two chemicals are normally an activator A and inhibitor B. A activates itself and B, whilst B inhibits both itself and A. When diffusion is included this can be written in the following form:

$$\frac{\delta A}{\delta t} = D_A \nabla^2 A + k_1 A - k_2 B \qquad \frac{\delta B}{\delta t} = D_B \nabla^2 B + k_3 A - k_4 B \qquad (6.1)$$

D_A and D_B are the diffusion constants and k_1,k_2,k_3,k_4 are constants. For pattern formation to occur in the original Turing system it is an essential prerequisite that the activator A must diffuse more slowly than the inhibitor B (see Figure 6.2). An extended mathematical discussion of why this is the case can be found in Edelstein-Keshet (1988), pages 509-520.

Under certain conditions related to parameters such as the production rate of the two substances and their respective diffusion values, a small increase in the activator, or a small decrease in the inhibitor concentration can lead to an acceleration in the size of the perturbation. The events leading up to this process are shown in Figure 6.3 and summarized below.

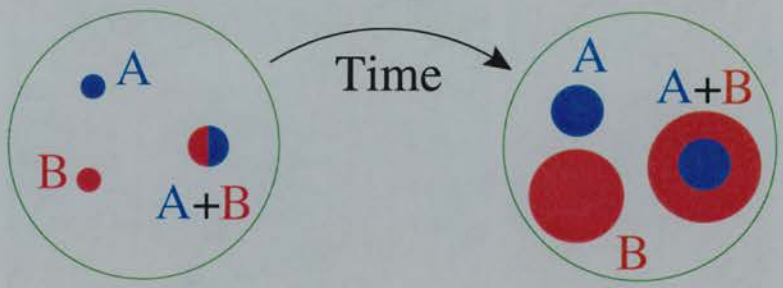

Figure 6.2: For Turing patterns to occur the activator A must diffuse slower than the inhibitor B.

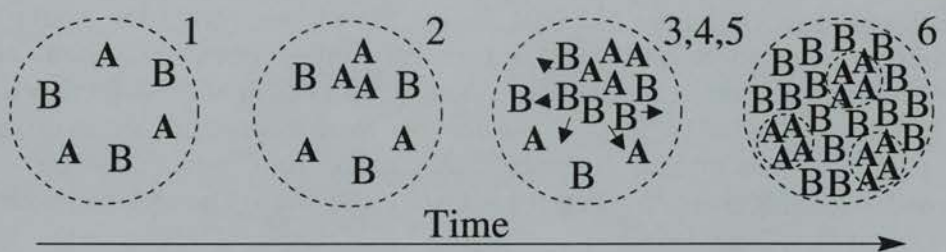

Figure 6.3: Reaction-diffusion events leading to pattern formation.

1. The system is in a homogeneous steady state.
2. A random perturbation leads to an increase in activator A.
3. Inhibitor B increases. If there is no diffusion this would halt the process.
4. The inhibitor diffuses faster than the activator.
5. The activator peak grows.
6. Surround inhibition leads to a characteristic pattern width.

The size of the patterns generated is dependent on the geometry of the surface or domain in which the reaction-diffusion system is found, and the ratio of the size of the domain to the range of the inhibitor. The size of the patterns can be changed simply by altering the value of one of the parameters in the Turing equations or by altering the size of the physical domain. The Turing

Figure 6.4: Reaction-diffusion systems have been used to explain animal markings and shell patterns. The tiger-like patterns on the left are cited from Young (1984). The mollusc shell pattern on the left is a digitised image from a real shell. The pattern on the right is from a model developed by Meinhardt and Klinger (see (Meinhardt & Klinger, 1987a, 1987b)). These images were taken from the excellent web site - "Visual Models of Morphogenesis: A Guided Tour" which can be found at http:www.cpsc.ucalgary.ca/projects/bmv/vmm/title.html. The web pages are based on (Prusinkiewicz, 1993, 1994).

equations are able to generate a large number of different behaviours - stripes, blobs, oscillations, moving waves - with only a small change needed in any one of the parameters. A large number of animal coat patterns such as tiger and zebra markings, seashell stripes, and drosophila wing prepatterns have all been explained in terms of a reaction-diffusion system (Figure 6.4). In the model presented here, the Turing patterns are used to explain the location of growth cone filopodia and their subsequent behaviour.

6.3 Filopodia Dynamics

As described in Chapter 3, the binding of F-actin to the substrate (through intermediary proteins such as integrin) converts the normal retrograde flow of polymer into a forward movement of the growth cone (Figure 3.3). A similar

mechanism is suggested for filopodial outgrowth and retraction. Outgrowth occurs through localised binding of the F-actin network to the substrate. The filopodia will extend as long as these links are maintained. However if the F-actin/substrate binding is removed, then the default retrograde flow of F-actin will cause the filopodia to shrink back into the growth cone. In this way localised variations in the binding of the F-actin network to the substrate are responsible for filopodia creation and subsequent behaviour.

Filopodia are essential to the normal navigational function of the growth cone. Contact by a single filopodia is able to induce outgrowth towards the guidance cue (O'Connor, Duerr, & Bentley, 1990), turning of the whole growth cone (Lin & Forscher, 1995) and complete collapse of the growth cone away from the stimulus (Bandtlow, Zachleder, & Schwab, 1990; Bastmeyer & Stuermer, 1993). Filopodia are also able to guide the growth cone by responding to diffusible gradients of external substances. Recently it was found that filopodia are essential in the chemotropic turning of the growth cone induced by a glutamate gradient (Zheng, Wan, & Poo, 1996).

Although the cytoskeleton of the filopodia is intimately involved with the growth cone proper it is also able to act in isolation. Filopodia cut off from the growth cone are able to respond to a variety of different environmental stimuli (Davenport et al., 1993). Functionally the properties of the filopodia are similar to those of the growth cone, however due to their large surface to volume ratio the influx of very small amounts of chemicals (e.g. a few calcium ions) will result in a large concentration increase in the filopodia. Weak signals can be amplified by the filopodia in this way and then passed onto the growth cone proper. The following section discusses the role of calcium in filopodial function.

6.4 Calcium as a morphogen

Calcium has previously been proposed as a morphogen regulating neuronal dendrite growth in a computational model of cell development (Hentschel, 1994). In this model, dendritic outgrowth was dependent on the concentration of calcium. The model showed how perturbations in the local cell membrane geometry resulted in a feedback loop which lead to an increase in calcium concentration. This in turn resulted in increased outgrowth of the cell membrane. The model was based on the "calcium-setpoint hypothesis" (Mattson & Kater, 1987). It was found in some cells that an increase in calcium lead to neurite outgrowth whilst in others shrinkage was observed. The calcium-setpoint hypothesis was put forward to account for this seemingly contradictory data. The hypothesis suggests that neurite outgrowth has a bell shaped dependency on calcium. Figure 6.5 shows how an influx of calcium can lead to either outgrowth or shrinkage depending on the calcium rest level for the particular neuron. For sensory neurons the resting concentration of calcium is greater than the peak level for outgrowth and an increase in calcium concentration above rest values results in neurite shrinkage. However the opposite is true for the Helisoma neuron whose resting calcium level lies below the peak level for outgrowth (Al-Mohanna, Cave, & Bolsover, 1992).

An increase in calcium (calcium hotspots) due to either calcium influx across the membrane or calcium induced calcium release (CICR) from internal stores has also been linked to filopodia outgrowth (Davenport & Kater, 1992; Davenport, Dou, Mills, & Kater, 1996). In cultured astrocytes and hippocampal neurons, application of glutamate induces a rise in $[Ca^{2+}]_i$ which is followed by a rapid elaboration of filopodia from the membrane surface (Cornell-Bell & Thomas, 1992). In a glutamate gradient, the projection of filopodia from the

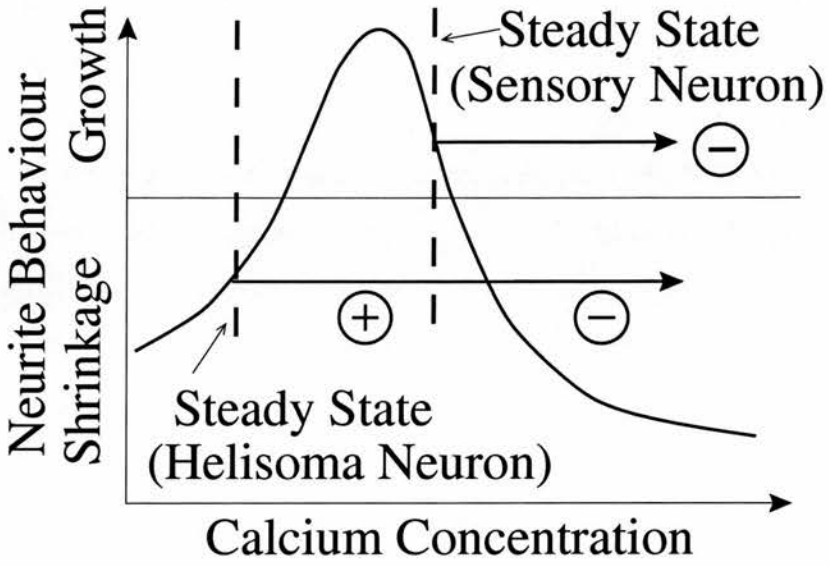

Figure 6.5: The calcium-dependent outgrowth hypothesis.

membrane surface is assymmetric and increasing up the concentration gradient (Zheng et al., 1996). The number and length of filopodia can also be increased by local depolarization resulting in calcium influx (Rehder & Kater, 1996). This increase in filopodia activity depends on the increase in $[Ca^{2+}]_i$ and is not a product of the depolarization alone.

The dynamics of the intracellular calcium signalling pathway are shown in Figure 6.6. If the calcium level rises above a certain threshold it activates the ryanodine receptors on the membrane of the endoplasmic reticulum (ER). The calcium concentration inside the ER (10^{-4}M) is over 1000-fold greater than the concentration of calcium in the surrounding cytoplasm ($10^{-7}M$). Activation of the ryanodine receptors causes the opening of calcium channels in the ER which releases a large amount of calcium ions into the cytoplasm.

CICR may not always be involved in the build up of calcium. Zimprich and Bolsover (1996) found that depolarization of neuroblastoma cell growth cones

results in a calcium gradient which is probably due to a higher density of L-type channels at the distal tip of the growth cone than at the base. A local release of calcium at the tip as a cause of the gradient was ruled out as agents that disrupted CICR did not affect growth cone calcium dynamics (Zimprich & Bolsover, 1996). In contrast CICR is a main component of the rise in $[Ca^{2+}]_i$ following dopamine application to the growth cone and attached filopodia (Davenport et al., 1996). In the dopamine experiments CICR was prevented using thapsigargin, a potent inhibitor of the calcium ATPase present on ER. Thapsigargin prevents calcium reuptake into calcium stores and as a result of continuous leakage can lead to their eventual emptying. It was found that the internal rise in calcium following application of dopamine was significantly reduced in the presence of thapsigargin. In the absence of thapsigargin, dopamine application evoked a significant rise in $[Ca^{2+}]_i$ in the growth cone proper and attached filopodia even when bathed in a calcium-free medium. However calcium levels in filopodia isolated from their parent growth cones did not rise. In these experiments organelles were found in the base of over 21% of filopodia but not in their tips. The majority of organelles were located deep in the center of the growth cone (Davenport et al., 1996). These results suggest the presence of intracellular calcium stores within growth cones, but not in the distal extensions of the filopodia.

The effect of calcium on neurite and filopodial outgrowth occurs through many calcium-regulated proteins which alter the structural integrity of the F-actin network. A number of these proteins are affected by variations in the concentration of internal calcium. These include α-actinin, an actin bundling protein, and gelsolin, a protein which severs the F-actin crosslinks. A transient rise in intracellular calcium due to calcium influx through ion channels activates gelsolin causing a 200 times increase in its affinity for actin. This leads to rapid filament side binding, then severing and capping of any free barbed filament

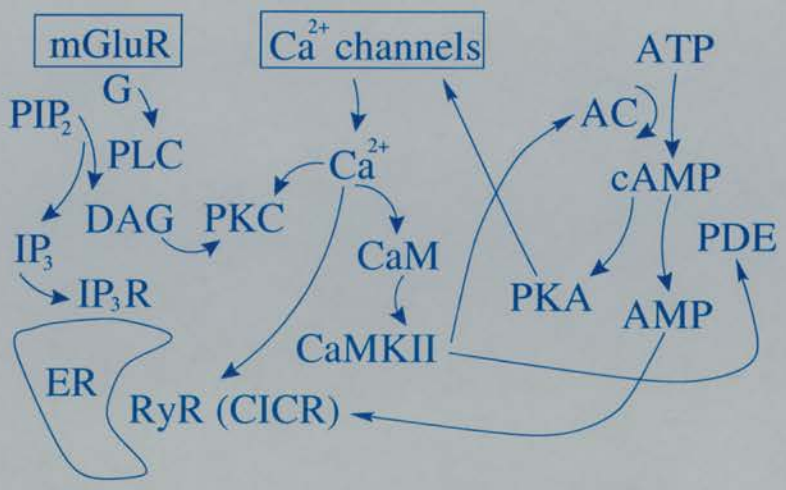

Figure 6.6: Cell calcium dynamics. Abbreviations: mGluR: metabotropic glutamate receptors, G: G-proteins, PIP_2 phosphatidyl-inositol-biphosphate,PLC: phospholipid C, DAG: diaclyglycerol, IP_3(R) inositol triphosphate (receptor), ER: endoplasmic reticulum, RyR(CICR): ryanodine receptor (calcium induced calcium release), Ca^{2+} internal free calcium, PKC: protein kinase C, CaM: calmodulin, CaMKII: calcium/calmodulin protein kinase II, AC: adenylcyclase, cAMP:cyclic AMP, PKA: protein kinase A, ATP: adenosine triphosphate, AMP: adenosine monophosphate, PDE: phosphodiesterase.

ends. The end result is the efficient shutdown of filament assembly and a dramatic disruption of existing actin network structure in the vicinity of calcium elevation. This does not necessarily result in F-actin network disintegration as the severed sections can act as new seed sites for F-actin assembly once calcium levels recover (Forscher, 1988). The F-actin network is closely linked to transmembrane proteins such as the integrins which determine the stability of the filopodia and consequently filopodial "lifetime"(Rehder & Kater, 1996). Therefore any alterations in the F-actin network due to localised changes in growth cone calcium concentration will also affect filopodial behaviour (Figure 6.8).

In the model, calcium influx and CICR promotes filopodial outgrowth and therefore calcium is viewed as an activator in the reaction-diffusion system. A candidate molecule for an inhibitor is cAMP as the diffuson constant of cAMP

$\approx 10^{-7} cm^2 s^{-1}$ is faster [1] than that of calcium $\approx 4.6 \times 10^{-8} cm^2 s^{-1}$ (Safford & Bassingthwaite, 1977; Goodwin & Trainor, 1985). The value of the diffusion constant of calcium used in the simulations (10^{-8}) was taken as a more recent value (Pelce, 1993). The ratio $\frac{D_{cAMP}}{D_{Ca}} = \frac{10^{-7}}{10^{-8}} \approx 10 > 1$. Thus calcium could act as a short range activator and cAMP as a long range inhibitor in the growth cone. Previously it has been suggested that cAMP and calcium act as a possible reaction-diffusion pair in the marine algae Acetabularia (Goodwin & Trainor, 1985). This is an order of green algae which inhabits warm seas. In Acetabularia single cells grow into cylindrical structures of enormous size - up to 4 cm long and 400 μm in diameter. The appearance of multiple calcium "whorls" in the single end tip precludes the development of multiple tips which takes place over the order of one to several days (Harrison & Hillier, 1985; Harrison, Graham, & Lakowski, 1988). The sequence of morphogenesis is shown in Figure 6.7).

In contrast to growth cone filopodia, in Acetabularia the end tips generated by the calcium whorls remain stable and fixed. The width of the spacings are dependent upon temperature and upon calcium concentration in the artificial sea water medium in which they are cultured. This is what would be expected if the spacing is kinetically controlled, especially in the way described by reaction-diffusion theories (Harrison & Hillier, 1985). However it

[1] The diffusion constant of calcium in the cytoplasm ($\approx 4.6 \times 10^{-8} cm^2 s^{-1}$) is over 100 times lower than the diffusion constant of calcium in water ($\approx 6 \times 10^{-6} cm^2 s^{-1}$). The calcium ion diffuses much more slowly in the cytoplasm than in an ordinary liquid phase because of the presence of fixed negative charges. Calcium preferentially binds to these ligands which considerably decreases its diffusive properties (Pelce, 1993). Another reason for the low diffusion constant of calcium in the cytoplasm is due to the large buffering effect of mitochondria and endplasmic reticulum. These contain calcium channels on their membrane surface which extract free calcium from the cytoplasm. As a result of this, the free calcium concentration in the cell ($\approx 10^{-7} M$) is over 1000 times less than the overall calcium concentration ($\approx 10^{-4} M$).

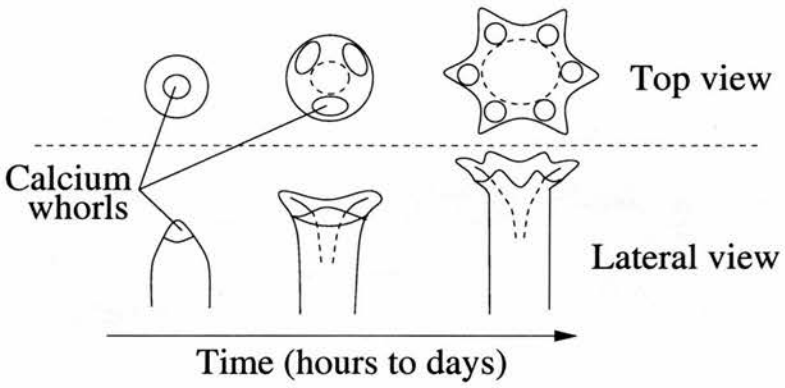

Figure 6.7: Calcium whorl patterns precede tip formation during morphogenesis in the marina algae Acetabularia.

has been suggested that cytoplasmic streaming in Acetabularia may destabilize any concentration differences, reducing the likelihood that Acetabularia uses a simple reaction-diffusion system to grow multiple tips (Goodwin & Trainor, 1985). In contrast any such streaming in the growth cone could serve to eliminate small, random concentration differences and only generate stable filopodia protrusions in the presence of a strong external signal. This may not be a significant problem as the large filopodia surface to volume ratio amplifies the external signal. This amplification gives filopodia a low threshold response to external stimuli, e.g. dopamine. The resulting localised influx of calcium may also lead to large scale CICR at the base of the filopodia and involve the growth cone proper.

6.5 The Simulation

The model chosen to simulate calcium and cAMP concentrations uses simplified equations based on a standard pattern generator developed by Gierer and Meinhardt ((Edelstein-Keshet, 1988) p. 531), with similar properties to equation 6.1.

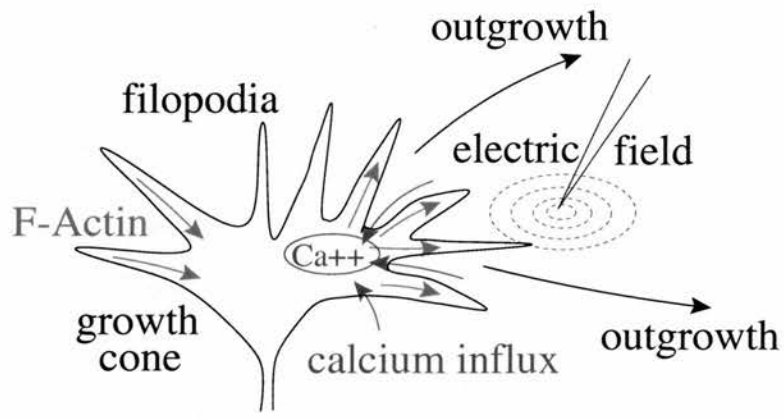

Figure 6.8: Effect of calcium influx on outgrowth.

$$\frac{\delta A}{\delta t} = \frac{k_1 A^2}{B} - k_2 A + D_A \nabla^2 A \qquad \frac{\delta B}{\delta t} = k_3 A^2 - k_4 B + D_B \nabla^2 B \tag{6.2}$$

In the equations, A represents calcium whilst B represents cAMP. Calcium activates itself and cAMP with rate constants k_1 and k_3. A rise in calcium levels due to CICR leads to a rise in cAMP levels, which inhibit further calcium increase. Both equations have inhibitory decay terms, with constants k_2 and k_4. (For calcium this can also be viewed as a term describing the net effect of membrane influx and pumping). The equations are implemented on a finite element grid with e.g. 100×100 pixels, representing a square of side 10 to 100 μm (Figure 6.9).

6.5.1 Stability of the reaction-diffusion patterns.

In the above system, stable Turing patterns occur when $\epsilon\delta > 1 + \sqrt{2}$ where $\epsilon = (\frac{k_2}{k_4})^{\frac{1}{2}}$ and $\delta = (\frac{D_{cAMP}}{D_{Ca}})^{\frac{1}{2}}$ (Edelstein-Keshet, 1988) pp531-532. In this system,

the greater the ratio $\frac{D_{cAMP}}{D_{Ca}}$ the more likely it is that stable patterns will be generated. As these are fixed quantities in the biological system, any changes in the behaviour of the system would have to occur through modifications to the decay parameters k_2 and k_4.

6.5.2 Overview of the model

At the start of the simulation the growth cone is circular, with diameter half the grid size. Initially, all pixels within the growth cone have steady state concentration values for calcium and cAMP with $\pm 1\%$ random noise added. Changes in the values of calcium and cAMP are calculated and updated at each time step.

Pixels outside the growth cone represent the substrate and are initially empty. Pixels on the growth cone membrane have a moveable position co-ordinate which allows them to expand radially into the empty pixels. Calcium and cAMP can then diffuse into the new space. Outgrowth and shrinkage is loosely modelled on the calcium-setpoint hypothesis and occurs as a function of calcium. In the model, maximum outgrowth of 6 μm/minute occurs at a concentration of 200 μM calcium. At very low and very high calcium concentrations, the flow is negative, representing lack of F-actin coupling to the substrate. Under these conditions the filopodia will shrink. In the present simulation, outgrowth and shrinkage only occurs from a fixed number of membrane pixels, while the remainder are static.

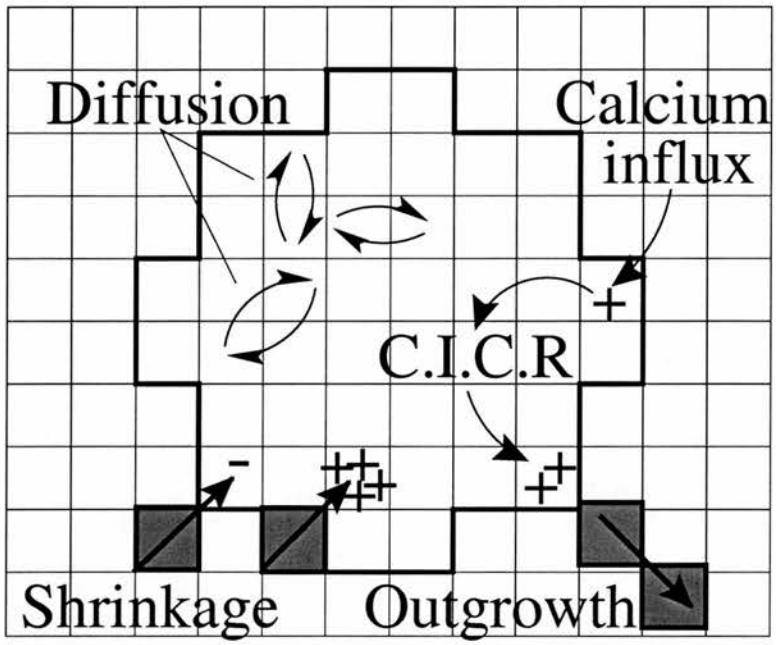

Figure 6.9: The filopodia model simulation grid. Outgrowth occurs within an optimum range of calcium concentration. Very low or very high concentrations cause the filopodia to shrink. N.B. It should be noted that calcium influx occurs at all points on the grid and not just points on the edge of the growth cone (as indicated by the arrow). Although the model is in 2-dimensions, the majority of the calcium influx will occur through the top surface. In Equation 6.2 there is no distinction between internal grid points, and points which lie on the membrane.

6.6 Computational Details

Simulations were written in Java 1.0. The model simulates a discrete square NxN grid representing a growth cone surrounded by extracellular space, e.g. N=100x100 pixels representing a physical space of 20x20μm. Each pixel has a state variable which takes one of two possible values: intracellular or extracellular. The growth cone is initially circular of $radius = \frac{N}{4}$ (The neurite shaft is not modelled.) All pixels within a distance of $\frac{N}{4}$ of the centre of the grid are considered to be part of the growth cone and intracellular. All other pixels are initially extracellular. Pixels within the growth cone have an initial starting value of calcium (100nM) and cAMP (100 dimensionless units). These values

are then perturbed by a small random amount ($\pm 1\%$) as Turing patterns do not form in a perfectly homogenous system. The amount of calcium/cAMP which is created, decays and diffuses into/out of each pixel is calculated at each 0.01s timestep. The net inlux/efflux is calculated for each intracellular pixel according to equations 6.2 and placed in a buffer for that pixel. Once this procedure has been repeated for all growth cone pixels at time t, the new concentrations at time $t + \delta t$ are updated in parallel from the buffers. Any outgrowth and shrinkage of the filopodia is then calculated.

6.6.1 Calculating outgrowth

In the current model, outgrowth is restricted to a limited number of pixels representing sites of filopodia on the outer membrane. (There were 32 outgrowth pixels in the simulations described in the results section. This limitation was purely due to the inherent difficulties in modelling a continuous outer membrane surrounding a discretized growth cone.) Each of the filopodia pixels contains a point, FP_{tip}, which represented the 2-dimensional (x,y) co-ordinates of the tip of the filopodia. At the start of the simulation FP_{tip} was located at the centre of the filopodia pixels. Outgrowth/shrinkage was limited to the axis radially outwards from the centre of the grid. Each FP_{tip} point was not allowed to shrink closer to the centre of the growth cone than its initial starting position.

The movement of the pixel depended directly on the calcium concentration and was calculated using the following outgrowth function:

$$outgrowth(\mu m/min) = he^{k(Ca-Ca_{peak})^2} - offset \tag{6.3}$$

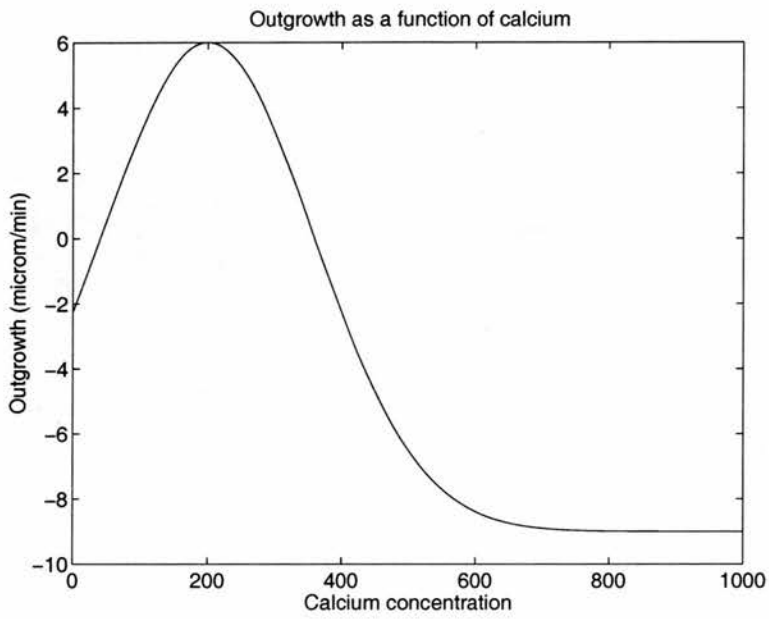

Figure 6.10: The curve shows how filopodial outgrowth (in $\mu m/min$) was calculated as function of the calcium concentration in the model. In the simulation optimal outgrowth occurred at a peak of 200nM. Shrinkage occurs at low and high levels of calcium.

The shape of this curve over the range $0 < Ca < 1000$ is shown in Figure 6.10 below. Maximum outgrowth ($6\mu m/min$) occurs at a calcium concentration $Ca_{peak} = 200nM$; $h = 15\mu$m controls the maximum height of the curve (the maximum outgrowth velocity); $k = 2 \times 10^{-5}$ controls the width of the curve and $offset = 9\mu$m/min determines where the zero crossings occur.

Each FP_{tip} grew radially outwards, or shrank radially inwards with a velocity that was dependent on the calcium concentration in the outgrowth pixel. If an FP_{tip} moved out of its current pixel into an extracellular pixel, a new intracellular pixel was created. If it shrank into a different intracellular pixel, the outer pixel was removed. In this way the local spatial concentration of calcium directly affected the outgrowth of the filopodia and the shape of the growth cone. Characteristic filopodia outgrowth patterns generated by the model are shown below.

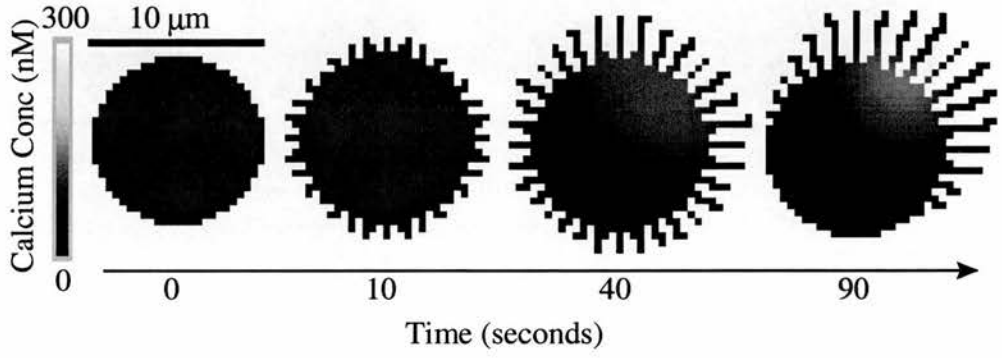

Figure 6.11: Time sequence of calcium concentration leading to stable pattern formation.

6.7 Results

Figure 6.11 shows the results of a simulation with k_1=k_2=k_4=1, k_3=0.01, $D_A = 10^{-8}cm^2s^{-1}$, $D_B = 10^{-7}cm^2s^{-1}$. Initially the growth cone has a calcium concentration of 100nM and filopodia sprout in all directions. After 40 seconds, a hot spot begins to develop, leading to extended growth in this area, and after 90s filopodia have retracted at the opposite pole. Stable filopodia are created where the calcium concentration results in no net growth or shrinkage at the tip of the filopodia.

The pattern of calcium within the growth cone can be altered by increasing the size of the cell (as shown in Figure 6.12) or by altering the decay parameters k_2,k_4, and keeping the size fixed. In the present model, the width of the calcium hotspots determines both where the filopodia sprout, and their maximum extension. As the calcium pattern extends across the filopodia themselves, growth is halted when the filopodia tip reaches the other side of the hotspot which caused the filopodia to grow out. Explicitly modelling the cal-

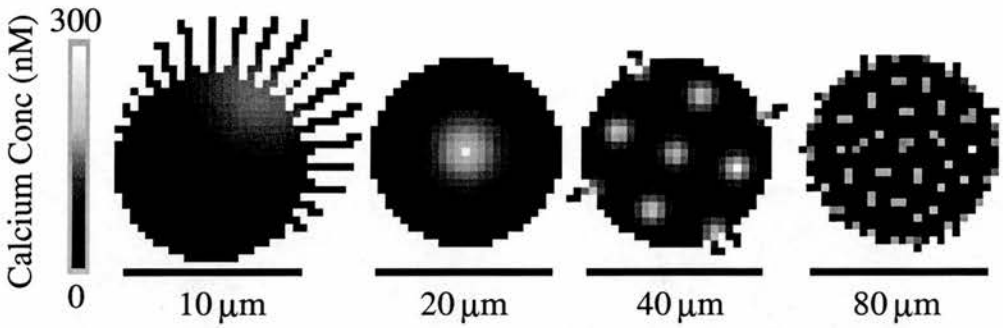

Figure 6.12: Stable patterns obtained at increasing length scales.

cium influx from the external medium would alter the maximum filopodia extension. As filopodia have a large surface membrane to volume ratio, a small calcium influx significantly affects the calcium concentration. Including this influx in the model may lead to narrow spacing of filopodia in the growth cone with long extensions.

In both Figures 6.11 and 6.12, the patterns are stable once the hotspots are established, and existing filopodia remain extended. Continuous extension and retraction of the filopodia would require an underlying calcium concentration with temporal and spatial variations. Unstable oscillations generated by the system are shown in Figure 6.13 (k_1=k_2=150,k_3=1, k_4=100,D_A=2.5 $\times$ $10^{-8}cm^2s^{-1}$). These oscillations are too rapid for stable outgrowth to occur but similar variations over a timescale of minutes would lead to filopodial extension and retraction.

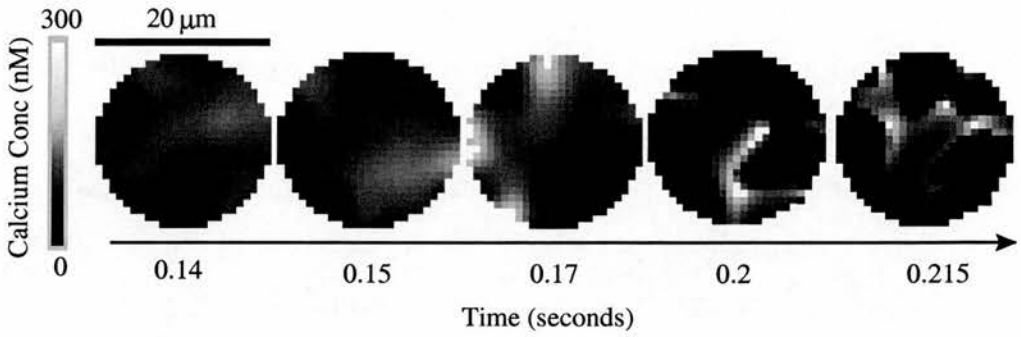

Figure 6.13: Time sequence of rapid, unstable patterns.

6.8 Discussion and Analysis

6.8.1 Strengths, weaknesses, predictions

The results of the simulations suggest that a wide range of growth cone and filopodial dynamic behaviours could be controlled by a Turing system which generates precise spatial patterns of calcium . Traditionally Turing equations have been used in models which generate fixed patterns that are stable in time. In the present model the requirement is for time varying/oscillating patterns which would define not only the point of creation of the filopodia, but also their subsequent growth and shrinkage dynamics. External stimuli received by the filopodia could then allow these local fluctuations to have a permanent effect on the structure of the growth cone. Previously the effects of cytoplasmic streaming have been put forward as a reason why simple Turing patterns may not underly whorl pattern formation in the marine algae Acetabularia. Although this is not implememented in the current simulations, this effect could have the advantage of only allowing localised hotspots to form and thus limiting the spread of the diffusion pattern.

There are a number of predictions that can be made by the model. It would be expected that a calcium hotspot in one part of the growth cone could lead to

hotspots being created in nearby parts of the growth cone separated by local minima of calcium. An increase in calcium would also be expected to narrow the spacing between such hotspots. It would also be expected that the behaviour of filopodia could be directly linked to the underlying spatial patterns of calcium. Such correlations have not yet been made directly although it should be possible for this to be verified experimentally.

6.8.2 Biological Plausibility

One of the key assumptions of the simulation is that a Turing-like reaction-diffusion system is an appropriate model for filopodia dynamics. With hindsight it seems that this assumption is too restrictive and that **any** dynamical system which produces localised calcium fluctuations in the growth cone would produce filopodia-like structures if outgrowth was linked to calcium concentration. The Turing system of equations which is described in this chapter may not be the most appropriate model which could be used to describe growth cone dynamics.

The stability criteria of the particular reaction scheme used in this model are dependent on the ratio of the diffusion constants $\frac{D_{cAMP}}{D_{Ca}}$ and the ratio of the decay parameters $\frac{k_2}{k_4}$. As the system is being applied to the growth cone, any change in growth cone or filopodial behaviour would have to occur through a modification of the inhibitory decay terms k_2 and k_4. It is possible that these systems are dynamically regulated by the cell in order to govern the response of the growth cone to extracellular stimuli. Recent experimental evidence supports this hypothesis. Song et al. (1997) found that differences in cAMP-dependent activity in a neuron could result in opposite turning of the growth cone in response to the same guidance cue (BNDF and ACh, but not

NT-3). Thus factors that modulate the activity of cAMP can affect the response of the growth cone to environmental stimuli. In the model above a change in the inhibitory-decay term k_4 would affect the behavior of the growth cone by changing the kinetics of the reaction-diffusion system. Inhibiting cAMP could lead to an over-amplification of calcium resulting in shrinkage not growth, in line with the calcium-outgrowth hypothesis. The status of the internal calcium concentration has not yet been determined during alteration of cAMP activity. The model predicts that it is the increase in calcium which has a repulsive effect. However the secondary calcium messenger system is not simulated in great enough detail for the current model to be able to make a strong prediction about which particular pathways might be involved.

One of the failings of the above reaction scheme is that the concentration of calcium approaches zero in the minima, whilst the maxima of calcium may have calcium values of up to 300 nM. In the cell, strong buffering mechanisms would ensure that the actual calcium levels did not fall to zero. Any extreme fluctuations in calcium concentration will be forced back towards their equilibrium value. This is not implemented in the reaction-scheme used in the current model. As a result there is not a direct mapping between the absolute values of the calcium concentration generated by the model and those observed in biological growth cones.

One of the weaknesses of the current simulation is that the number of membrane points allowed to develop into filopodia are limited. This arose as a result of the difficulties of modelling a continuous elastic membrane for smooth outgrowth and shrinkage whilst simultaneously modelling the internal calcium concentrations on a discrete grid. Although it is possible that biological factors such as local calcium stores, and radially oriented microtubules may create discrete sites for filopodia creation, it is more likely that filopodia could develop continuously along the membrane.

The following implementational issue also needs to be modified to make the model more biologically realistic. In the current simulation outgrowth and shrinkage occurs only at the tip of the filopodia. However it is likely that conditions at the base of the filopodia play an important role in determining the lifetime of the filopodia. This was not implemented in the current model. Although it is unlikely to have a significant effect on the types of structures which are generated by the model, there were occasions when a local calcium minima occurred at the base, whilst a more optimal calcium concentration occured at the tip. Under these conditions the simulated filopodia did not retract, although it is likely that this scenario could cause a complete retraction of the filopodia in a biological growth cone.

6.8.3 Conclusion

The aim in developing this model was to move away from a description of filopodia as random and unpredictable structures. I hope that in the process of creating this model I have at least been partially successful in an attempt to move closer towards an understanding of how filopodia might be generated, and how their behaviour could depend on the local subcellular conditions. The overall conclusion of the model is that any mechanism which results in a slowly varying temporal and spatial calcium pattern would alter the local neurite geometry, resulting in filopodial creation, outgrowth and shrinkage. This would not have to be restricted to the Turing reaction-diffusion system implemented here.

On a final note the more abstract issue of a self-modifying structure whose function is in turn dependent on its own shape could also be further explored.

It appears that there are few models which deal with this unusual type of behavior. This may be because few such systems exist (although at a much higher level the brain could be classified as one such system.) This is one of the many possible adaptations that could be made to the present model which it is hoped provides a fresh starting point for understanding filopodia dynamics from a new biological and computational perspective.

Chapter 7

Computational Models of Dendritic Branching.

7.1 Introduction

The function and behaviour of the adult neuron is intrinsically tied to the structure of its dendritic arbor which forms during development. The shape of the arbor determines both the type of cell a neuron makes connections with, and the number and quantity of input signals it receives. This has an immediate effect on its output spiking properties and overall behaviour. Understanding what causes the characteristic dendritic structures of neurons to form would therefore also lead to an increased understanding in the functional properties of neurons. In the previous chapters, growth cone dynamics were modelled over a short timescale of seconds to minutes. This chapter describes a simulation of the development of the dendritic arbor over a period of days to weeks.

This is one of the first models of dendritic branching to produce realistic dendritic arbors with a mechanism which is directly motivated by experimental data.

Previous computational models of dendritic branching are broadly split into 2 categories. Models which aim to describe the structure of dendritic arbors in an efficient statistical manner using a limited number of parameters, e.g. (Kliemann, 1987; Burke, Marks, & Ulfhake, 1992; Tamori, 1993), and models which aim to generate branching patterns based on fundamental biological mechanisms. The latter models have used random branching (Li, Qin, & Wang, 1992), tension induced by the random positioning of growth cone filopodia (van Veen & van Pelt, 1992; Li, Qin, & Wang, 1995), and branching induced by fractal aggregation of neurotrophin (Albinet & Pelce, 1996) [1].

Other models such as the QS-model (van Pelt & Verwer, 1986), a two parameter probability model of neurite branching based on the order of terminal segments, and later variations (van Veen, 1993; Dityatev, Chmykhova, Studer, Karamian, Kozhanov, & Clamann, 1995; van Pelt et al., 1997) and the BESTL model (van Pelt & Uylings, 1997) fall somewhere in between the statistical and mechanistic models. The BESTL model in particular has been extremely successful in reproducing the characteristic dendritic structures of neurons and has given insight into how dendritic elongation and branching rates vary as growth proceeds. However none of these models has directly clarified the mechanisms involved in branching at the level of microtubule or F-actin organization in the neurite.

[1] In this model a circular cell is at the centre of a square grid and a neurotrophic factor is released from random sites around the edge of the grid. When the neurotrophin encounters the cell a new neurite "pixel" is added to the existing cell structure. In this way a fractal branching structure emerges similar to some neuronal branching patterns.

The new model aims to bridge the gap between these different approaches. The model is based on recent experimental data which indicates that the phosphorylation state of microtubule associated protein 2 (MAP2) may play a key role in controlling dendritic elongation and branching (Audesirk, Cabell, & Kern, 1997). This supports the hypothesis put forward by Friedrich and Aszodi (1991) that MAP2 phosphorylation, which increases the spacing between microtubules, could also cause dendritic branching. In the new model, the intracellular calcium concentration (acting through calcineurin and Ca^{2+}/calmodulin-dependent protein kinase II (CaMKII)) influences the (de)phosphorylation state of MAP2 which can switch development between elongation and branching. The basis for branching in the model is the splitting of microtubules caused by wider spacing of microtubules within the bundle. Dephosphorylated MAP2 favours elongation by promoting microtubule polymerization and bundling, whilst branching is more likely to occur when MAP2 is phosphorylated and microtubules are spaced apart. In the model, the rate of elongation and branching is directly determined by the ratio of phosphorylated to dephosphorylated MAP2. This acts as a 2-way switch to control the rate of elongation and branching. This is regulated by calmodulin-dependent protein kinase II (CaMKII) and calcineurin, which are both dependent on the intracellular calcium concentration. In the model, the functions relating calcium with MAP2 (de)phosphorylation have an important role in determining what type of branching pattern will occur.

The new model is able to generate a wide variety of different branching behaviours aswell as reproducing the branching patterns of specific cell types. It is also able to generate specific biological branching patterns without the need for a specific branching or elongation phase. Based on the results from the model, predictions can also be made about the cellular mechanisms that are likely to be involved in controlling neurite branching and elongation. The

results suggest that the same underlying mechanisms could control both elongation and branching in cells with diverse dendritic arbors, e.g pyramidal and Purkinje cells, and that elongation and branching do not have to be independent.

The model predicts that the branching pattern will change following manipulations with calcium, CaMKII and MAP2 phosphorylation. Further experiments are needed to directly link these values to the dynamic processes of branching and elongation. Depending on these values, the dendritic arbor may be largely unbranched, or branch extensively. The model also predicts that the typical branching patterns observed in particular cells could be transformed into the branching pattern of a different cell type through manipulation of calcium and MAP2 levels, and CaMKII phosphorylation status. This should be experimentally verifiable.

7.2 The causes of branching

This section reviews the causes of neurite branching and elongation and highlights the possible role of phosphorylated MAPs in controlling the structure of the dendritic arbor. The branching discussed in this paper refers to bifurcation of the growth cone at the distal tip of the dendrite, rather than branching of the axon which occurs principally by the formation of collaterals (O'Leary & Terashima, 1988).

7.2.1 Internal v External Growth and Branching Signals

In some neurons the number of axons and dendrites appears to be intrinsically programmed. Cultured hippocampal neurons acquire their characteristic form

by a stereotyped sequence of developmental events (Dotti, Sullivan, & Banker, 1988). The cells initially establish several identical processes but after a number of hours, one of the processes begins to grow very rapidly and becomes the axon. The other processes which will become dendrites elongate a few days later at a much slower rate. The morphology of these neurons is largely unaffected by afferent input or target tissue (Lein et al., 1992). This is also generally true for pyramidal cell dendrites. The basal dendrites of cortical pyramidal neurons normally branch towards the grey/white boundary and away from the pia-mater. In "improperly"- oriented cells where the cell body may be 180^o rotated "upside-down", both the basal and apical dendrites form normally in relation to the cell body, but upside down in relation to the rest of the cortex (van der Loos, 1965). This suggests that these dendrites are primarily controlled by an intrinsically generated signal and are not reliant on external influences which would alter the dendritic morphology of a misaligned cell. (In contrast the axons of these mis-oriented pyramidal neurons may be abruptly re-aligned shortly after sprouting, presumably by the presence of an external, chemotropic gradient.) This indicates that in some instances an intrinsic signal can be sufficient to establish cell polarity and dendritic arborizations.

In other cells however, external influences have a strong effect on the overall cell shape. This is true of the cell shape of sympathetic neurons which can be influenced by numerous environmental factors ((Lein et al., 1992) and references therein). In the cerebellum, the characteristic shape of the Purkinje cell is significantly altered by removing the afferent input provided by the parallel fibres of the granule cells (Ito, 1984). Blocking the electrical activity of the Purkinje cell also results in significantly elongated dendrites compared to normal (Schilling, Dickinson, Connor, & Morgan, 1991). However these dendrites only elongate at rates above normal after day 7 in vitro at which time electrical connections between cells first appear. Before this stage it seems that an

intrinsic signal generates the characteristic dendritic arbor which is later modified through synaptic interactions. Therefore any model of branching needs to be able to account for both intrinsically programmed and externally driven branching events.

7.2.2 Branching induced by tension

Analysis of filopodia patterns in tissue cultured cells indicates that there is a progressive increase in branching with an increase in the number of lateral filopodia (van Veen, 1993). Bifurcation of the growth cone occurs when tension created by the pulling of asymmetrically distributed filopodia tears apart the neurite. Branching can also be induced by physically removing the filopodia at the front of the growth cone so that filopodia only remain at the sides (Wessels & Nuttall, 1978). The generation of asymmetric filopodia in developing cells may require the presence of an external influence such as randomly distributed morphogen or chemoattractant.

7.2.3 Microtubule Associated Proteins (MAPs)

As branching is produced by changes in the cytoskeleton involving microtubules and actin (Diez-Guerra & Avila, 1993; Friedrich & Aszodi, 1991), factors which alter microtubule dynamics will also have a significant effect on neurite branching. The microtubule inhibitor taxol inhibits branching in sensory and sympathetic neurites (Letourneau, 1986). In contrast numerous dendritic branches emerge when microtubules are depolymerized with nocodazole, indicating that microtubule disassembly can promote branching (Audesirk et al., 1997). The MAP family of proteins regulate many factors of mi-

crotubule interactions including microtubule assembly and disassembly (Yamamoto, Fukunaga, Tanaka, & Miyamoto, 1983; Pryer et al., 1992), microtubule bundling, microtubule interaction with external receptors (Maccioni & Cambiazo, 1995), microtubule spacing (Chen, Kanai, Cowan, & Hirokawa, 1992), microtubule interaction with actin (Selden & Pollard, 1983), and many others (see Maccioni & Cambiazo (1995) for review).

Within single neurons, the microtubule associated protein MAP2 is primarily found in dendrites, whilst MAP1b and tau are found in the distal region of the axon (Black, Slaughter, & Fischer, 1994; Black, Slaughter, Moshiach, Obrocka, & Fischer, 1996). The different distributions of MAPs can account for the differences in microtubule spacing and orientation between neurites and axons. Microtubules in the developing axon are closely spaced due to the small projection domains of MAP2c and tau. In contrast microtubules in developing dendrites are widely spaced due to the long side-arm projection domain of MAP2 (Chen et al., 1992). In axons microtubules are all oriented in the same direction, with the plus end facing the distal end of the axon whilst in dendrites microtubules are oriented in both directions. In addition to its interaction with microtubules, MAP2 acts as a crosslinker mediating the interaction between microtubules, other cytoskeletal elements such as F-actin, and cytoplasmic organelles (Selden & Pollard, 1983; Friedrich & Aszodi, 1991). As MAP2 is present in dendrites in excess of its binding sites on tubulin it has been suggested that MAP2 functions to ensure virtually total polymerization of tubulin in dendrites (Matus, Bernhardt, Bodmer, & Alaimo, 1986). This total polymerization would promote elongation and suppress branching.

7.2.4 Effects of MAP Phosphorylation

The phosphorylation state of MAPs modulates their interactions with microtubules. Tau and MAP2 bind to microtubules and increase microtubule assembly and/or stability when they are dephosphorylated (Audesirk et al., 1997). However increased phosphorylation decreases these effects. Several protein kinases are involved in MAP2 phosphorylation including cAMP-dependent protein kinase, and CaMKII (Diez-Guerra & Avila, 1993). Phosphorylation of MAP2 and tau by the protein calcium/calmodulin-dependent protein kinase II (CaMKII) inhibits microtubule assembly (Yamamoto et al., 1983) by reducing the binding of MAP2 and tau to microtubules (Biernat, Gustke, Drewes, Mandelkow, & Mandelkow, 1993; Brugg & Matus, 1991). Phosphorylation of MAP2 by CaMKII also inhibits the ability of MAP2 to cross-link actin filaments (Yamauchi & Fujisawa, 1988). In lamprey central neurons microtubule destabilization and protein phosphorylation precedes dendritic sprouting (Hall, Lee, & Kosik, 1991). In contrast dephosphorylation of MAP2 enhances microtubule assembly and bundling (Yamamoto, Saitoh, Fukunaga, Nishimura, & Miyamoto, 1985). Thus the phosphorylation state of MAPs is likely to play an important part in controlling microtubule spacing and subsequently branching.

Modification of microtubule bound MAP2 by CaMKII could affect the microtubule bundling function suggested for MAP2 (Lewis, Ivanov, Lee, & Cowan, 1989), and a decrease of that bundling may be related to the appearance of dendrite arborization. In developing hippocampal cultures, an exponential increase in dendritic arborization correlates with an exponential increase in MAP2 phosphorylation (but not with the total amount of unphosphorylated MAP2, or the overall neurite length) (Diez-Guerra & Avila, 1993). During development, the amount of CaMKII increases 5 fold between postnatal day 0

and day 19 in the rat superior colliculus (Scheetz, Prusky, & Constantine-Paton, 1996). The amount of CaMKII also increases in hippocampal pyramidal neurons during dendrite development where CaMKII is first detected in growth cones (and cell bodies) (Scholz, Baitinger, Schulman, & Kelly, 1988). Further experimental support for a role of CaMKII in dendrite branching was provided recently when it was found that inhibitors of CaM kinases reduced dendrite branching to as little as 30% of control values (Audesirk et al., 1997). In the same set of experiments, an increase in dendritic branching of up to 200% was obtained by applying agents that increased protein phosphorylation.

Changes to the state of the microtubule array due to CaMKII will also affect the dynamics of the F-actin network in the growth cone. Microtubule penetration into the growth cone may promote lamella formation either by local membrane insertion (Martenson, Stone, Reedy, & Sheetz, 1993) or by modulation of actin organization (Rinnerthaler, Geiger, & J., 1988). Calmodulin inhibits the interaction of MAP2 and tau with actin (Kotani, Nishida, Kumagai, & Sakai, 1985) which may make branching more likely to occur. Both calmodulin and CaMKII are molecules which underly the decoding of calcium signals. As CaMKII function is calcium dependent, changes in the growth cone calcium concentration will also affect neurite elongation and branching. The calcium-outgrowth hypothesis (Kater, Mattson, Cohan, & Connor, 1988) states that there is an optimal level of calcium required for neurite elongation. Above and below this level neurite elongation is reduced. Changes in calcium could then affect neurite elongation by altering the physical dynamics of microtubule assembly through the phosphorylating action of CaMKII on MAP2.

The above experimental results suggest that the phosphorylation of MAP2 in dendrites by CaMKII affects microtubule stability and growth and may play a key role in switching neurite development between elongation and

branching. This is the mechanism used in the new model of dendrite elongation and branching. The new model is introduced after the following section which summarizes several previous computational and theoretical approaches to modelling dendritic trees.

7.3 A review of theoretical and computational models of branching

Previous computational models of branching are broadly split into two categories: data-driven (statistical) models and process-driven (explanatory) models. These are discussed separately below.

7.3.1 Data driven models

This type of model simulates the particular branching patterns of a neuron without specifically addressing the underlying cytoskeletal processes involved. In general these models use a limited number of parameters to statistically characterise the dendritic trees involved, e.g. (Kliemann, 1987; Burke et al., 1992; Tamori, 1993; Dityatev et al., 1995). Two important models of this type, the QS-model (van Pelt & Verwer, 1986) and a recent extension, the BESTL-model (van Pelt & Uylings, 1997) are discussed below. The key result from this type of model is that a random branching mechanism is sufficient to generate the wide variety of branching and geometric patterns seen in biological dendritic trees. Results from the BESTL model are used to assess the biological characteristics of dendritic trees generated by the new model in the Results section.

The QS model

The QS-model was one of the first models to successfully characterise different types of dendritic branching (van Pelt & Verwer, 1986). In the QS-model the dendritic arbor is made up of intermediate and terminal segments. Intermediate segments end in a branch point whilst terminal segments are unbranched (See Figure 7.1). The model simulates the branching process in discrete timesteps and at each timestep one intermediate or terminal segment is randomly chosen to undergo a branching event. This process is repeated until the dendritic tree is obtained.

Two parameters, Q and S, are used to determine the probability that any given segment in the dendritic arbor will branch in the next time step. Biological data indicates branching probability decreases as the centrifugal order, γ increases. The centrifugal order, is the number of branch points that lie between any given segment and the soma. The main dendrite is numbered 0 and the centrifugal order increases by 1 at each subsequent branching point. Parameter S determines the effect of the centrifugal order on the branch probability at a terminal segment. This is given by $p_{term} = C2^{-S\gamma}$. If S=0, all terminal segments have the same probability of branching ($p_{term} = C$, where C is a normalisation constant so that the sum of the branching probabilities for all segments in the tree equals 1.) If S=1, the probability that a terminal segment branches decreases by 2 with each increment in the centrifugal order γ.

Parameter Q determines the extent to which the intermediate segments branch. This is given by $p_{int} = \frac{Q}{1-Q}p_{term}$. If Q=0 all branching occurs at the terminal segments and no branching occurs at intermediate segments: if Q=1 branching only occurs at the intermediate segments. By varying the parameters Q and S, the topology of the simulated trees is matched to the biological

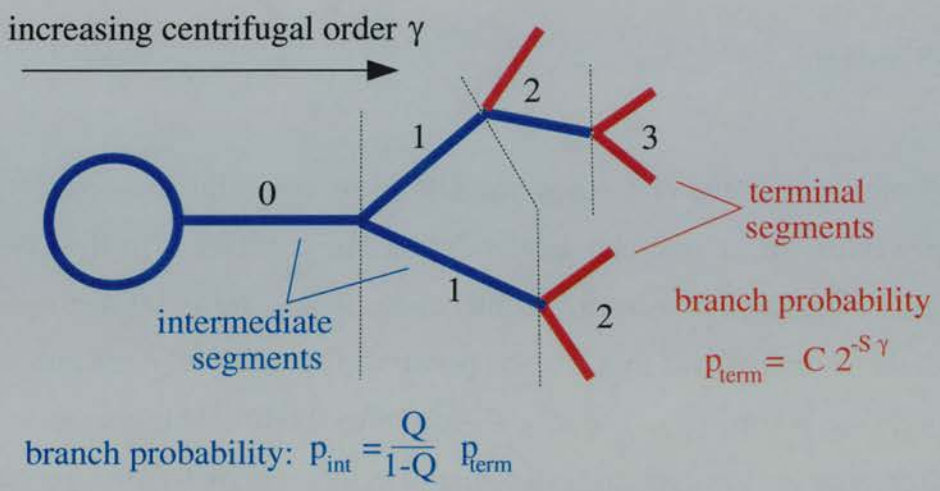

Figure 7.1: The QS branching model. Branching depends on (i) the extent to which the intermediate segments branch (the Q parameter), and (ii) the rate at which the branch probability decreases with increasing centrifugal order γ (the S parameter).

trees to obtain the best fit of the model to the data. A large number of different cell types can be characterised by the model. As stated in van Pelt *et al.* (1997), "in all cases optimized parameter values could be found [in the QS-model] so as to accurately reproduce the observed topological variations." The QS model showed that complicated cell dendritic arbors could be recreated using a fairly simple random process with only two variable parameters. However there do not seem to be any biological chemicals which could directly take the role of the Q- and S-parameters.

The BE- and BESTL models

The BESTL model (van Pelt & Uylings, 1997) is an extended version of the BE-model (van Pelt et al., 1997) which in turn extends the QS model. In the BE- and BESTL models, the parameter Q governing the probability that an intermediate segment branches is set to 0. (Most neurons can be accurately described by assuming that all branching occurs at the terminals (van Veen &

van Pelt, 1992)). Compared to the BE- model, the BESTL model includes extra parameters (S, T, L) to obtain a better fit to experimental observations.

In the BE- growth model, branching events only occur at terminal segments. The simulated period of dendritic tree development is divided into N time bins. In each time bin, i, one terminal segment is randomly chosen to branch with a probability given by:

$$p_i = \frac{B}{N n_i^E} \tag{7.1}$$

The parameter B represents the number of branching events that occur at an isolated segment in the full simulation run. The parameter E denotes the dependence of the branching probability on the total number n_i of terminal segments in the growing tree. If $E = 0$ the probability of branching is a constant at all terminal segments ($p_i = B/N$) and independent of the number of terminal segments in the tree, e.g. if 3 branching events are expected to occur over 200 timesteps then the probability of branching per timestep is $p_i = B/N = 3/200$. If E=1, then the branch probability decreases linearly with the increasing number of terminal segments n_i ($p_i = B/N n_i$).

This model was extended by incorporating the S-parameter from the QS-model so that branching is also dependent on the centrifugal order (γ) of the segment. The next extension to the model was to simulate the branching process in "real-time" (the T parameter) by mapping the time-bin scale (e.g. in units of 1-200) onto a real time-axis. Finally the elongation rate of the segments was determined from experimental observations so that the lengths L of simulated dendrites would be similar to those found in biological arbors. By incorporating the extra parameters S,T and L into the BE-model, both the branching-pattern and geometric topology of the simulated trees could then be closely matched to experimental observations.

As might be expected, the BESTL model is able to accurately fit a wide range of dendritic topologies. Results from the model highlight when different stages of growth occur in different neurons. Based on the parameters used to model individual cell types, clusters of groups of neurons with similar branching patterns appear. This may help to show if the different branching patterns produced by various cell types share the same underlying growth mechanisms.

Process driven models

The second type of model simulates the general mechanisms of neurite elongation and branching. Although the branching in these models may be directly attributable to a possible cytoskeletal event, the dendritic patterns produced by the models may not have any quantitative similarity to dendritic arbors in real cells, e.g. (Li et al., 1992; Hentschel, 1994; Li et al., 1995; Hentschel & Fine, 1996; Albinet & Pelce, 1996).

Albinet and Pelce (1996) developed a model to account for the short-range fractal nature of dendrites. In the model internal fibrillar proteins diffused to the outer cell membrane where they interacted with an external chemoattractant leading to additional growth. This model was able to generate fractal dendritic patterns.

The dendritic growth models of Hentschel and Fine (1994,1996) were based on the action of calcium as a morphogen. In the models, instabilities in the geometry of the membrane surface resulted in a localised increase in the surface area to volume ratio at certain points. This lead to an increased calcium influx which enhanced any membrane instabilities through a positive feedback loop. This created a dendritic stump and further instabilitites then resulted in the

formation of dendritic branches. A robust phenomenon of the model was the emergence of increasing calcium gradients ranging from low levels in the cell body to higher levels more distally along the dendrite. This calcium gradient resulted from spontaneously emerging gradients of sodium and membrane potential. Similar gradients are also seen along the processes of real neurons (Cohan, Connor, & Kater, 1987; Bedlack et al., 1992; Bedlack, Wei, Fox, Gross, & Loew, 1994). (In the new MAP phosphorylation model this calcium gradient is simply created by including an influx term proportional to the surface to volume area of the dendrite.)

Both of these models produced primarily circular dendritic arbors which showed some qualitatively similar geometry to biological dendrites. However in both models the mechanism employed for dendritic branching and elongation is only able to reproduce a limited range of cell branching patterns.

Van Veen and van Pelt developed a model based on the experimental finding that lateral filopodia produce a directed tension which "tears" apart the growth cone, causing the neurite to branch (van Veen & van Pelt, 1992). The filopodia were initiated when they encountered a randomly dispersed morphogen molecule within a certain radius of the tip of the neurite. The neuronal geometries obtained by the model were similar to those obtained in biological neurons. Such experiments indicate that the formation of lateral filopodia can be a key factor in neurite bifurcation. However the intrinsic geometries of hippocampal dendrites cannot easily be explained by the van Veen and van Pelt model.

Finally Li has developed a number of different models of neurite elongation and branching. These have been based on random branching and inhibitive interaction between branches (Li et al., 1992), an extension of the van Veen and

van Pelt model (Li et al., 1995) and a tension based model (Li & Qin, 1996). However none of these models directly simulates the internal processes leading to elongation and branching.

The statistical models, of which the BESTL-simulation is one of the most recent, now characterize biological dendritic arbors to a high accuracy. It is uncertain whether further insight into the branching process will be gained by increasing the number of simulation parameters to account for smaller discrepancies between the model results and biological data. In contrast, none of the models which aim to simulate cellular processes involved in branching are able to accurately match a wide range of dendritic topologies although they might be able to provide testable biological predictions. The aim in creating this new model was to combine the generality and accuracy of the statistical models whilst using a biologically plausible and testable growth mechanism.

7.4 The Model

7.4.1 Compartmental Model

The developing neuron is described by a simple compartmental model which initially has two compartments - a spherical soma of radius R_{soma} and a single, short, cylindrical dendrite of length L and radius R (see Figure 7.2a). Each compartment contains a particular concentration of intracellular calcium (Ca) and MAP2. The model simulates the elongation of the dendritic tree in discrete timesteps, dt. New compartments of length dx are added as the dendrite grows. All terminal dendrite segments grow out until they reach length 2*dx. At this point the terminal compartment is split into two compartments each of

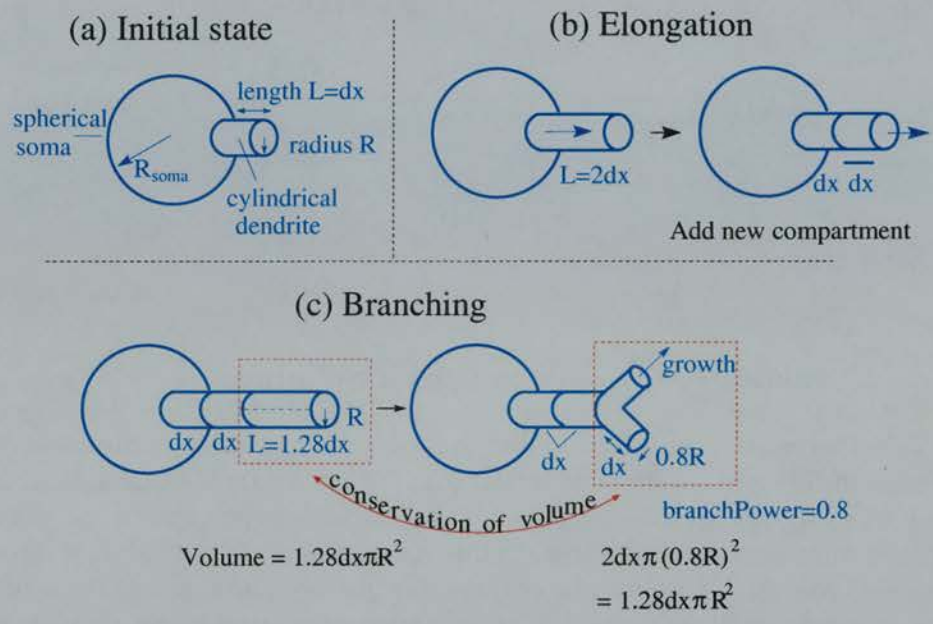

Figure 7.2: The compartmental model. (a) Initial state, (b) New compartments are added when the length of the terminal compartment increases above a fixed threshold. (c) Branching involves the redistribution of the terminal compartment volume into a terminal compartment of unit length. The remaining volume is used to make up two new compartments. The radius of newly branched dendrites is equal to the parent dendrite radius multiplied by the branching Power (default: branchPower=0.8).

length dx (see Figure 7.2b) and the process is repeated with the new terminal compartment. This allows continous dendrite growth using discrete compartments. At each timestep a terminal compartment may branch with a probability, $P_{branching}$, determined by the concentration of Ca and the phosphorylation state of MAP2 (see below for a definition of $P_{branching}$. The segment continues to elongate if $P_{branching} < R$ where R is a random number ($0 < R < 1$). However if $P_{branching} > R$ the segment branches. Two new daughter compartments are then created such that the volume of the terminal compartment is preserved (see Figure 7.2 c). The simulation was stopped after a given length of time and the characteristics of the dendritic arbor were noted.

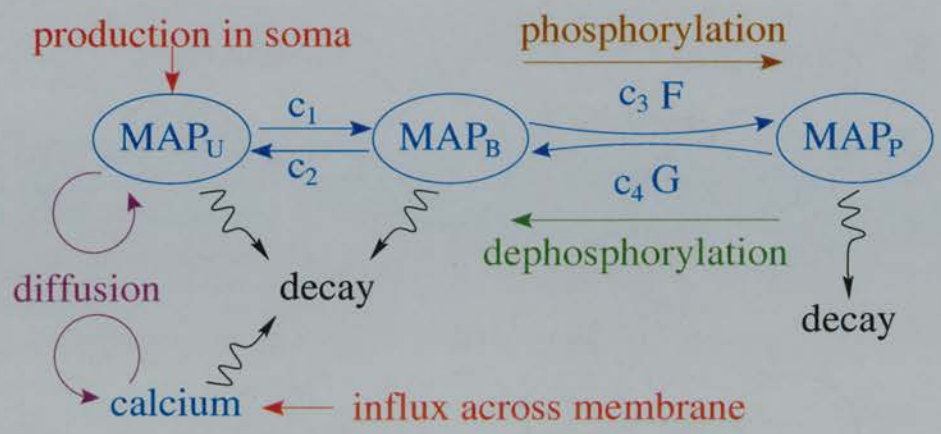

Figure 7.3: The cell dynamics simulated in the branching model. Diffusible $MAP2_u$ is produced in the soma and is converted into the microtubule-bound $MAP2_b$ complex and then phosphorylated into $MAP2_p$. Calcium enters across the membrane and diffuses throughout the dendrite. In the non-linear model the calcium-dependent functions F, G control the on/off rate of phosphorylation. The shape of these functions is shown for various values of the steepness parameter k used in the simulations.

7.4.2 MAP2 (De)phosphorylation.

The reaction scheme used in the model is shown in Figure 7.3.

The two dynamic variables in the model are the concentrations of intracellular calcium (Ca) and soluble and **unbound** MAP2 ($MAP2_u$). These directly determine the concentration of dephosphorylated MAP2 which is **bound** to microtubules ($MAP2_b$) or bound and **phosphorylated** by CaMKII ($MAP2_p$). The concentrations of microtubule polymer and calmodulin/CaMKII protein are not explicitly modelled. The rate of change of Ca and $MAP2_u$,$MAP2_b$ and $MAP2_p$ in each individual compartment is given by the following four differential equations.

$$\begin{aligned} \frac{\partial Ca}{\partial t} &= D_{Ca}\frac{\partial^2 Ca}{\partial x^2} + I - \delta_{Ca}Ca \\ &= diffusion + influx - decay \end{aligned} \tag{7.2}$$

$$\begin{aligned} \frac{\partial MAP2_u}{\partial t} &= D_u\frac{\partial^2 MAP2_u}{\partial x^2} + P - c_1 MAP2_u + c_2 MAP2_b - \delta_u MAP2_u \\ &= diffusion + prodn - rate\ to/from\ MAP2_b - decay \end{aligned} \tag{7.3}$$

$$\begin{aligned} \frac{\partial MAP2_b}{\partial t} &= c_1 MAP2_u - c_2 MAP2_b - F + G - \delta_b MAP2_b = 0 \\ &= rate\ to/from\ MAP2_u - de/phosphorylation\ to/from\ MAP2_p - decay \end{aligned} \tag{7.4}$$

$$\begin{aligned} \frac{\partial MAP2_p}{\partial t} &= F - G - \delta_p MAP2_p = 0 \\ &= de/phoshorylation\ to/from\ MAP2_b - decay \end{aligned} \tag{7.5}$$

The equations were solved using first-order Euler integration with a fixed timestep dt ($< \frac{dx^2}{2D}$ to ensure diffusive stability (Press *et al.*, 1988)). $MAP2_b$ and $MAP2_p$ are assumed to be at steady-state at each timestep. This allows the concentration of $MAP2_b$ and $MAP2_p$ to be directly calculated knowing the concentration of Ca and $MAP2_u$. $MAP2_u$ is produced in the soma at a constant rate P (P is zero elsewhere). To model the calcium gradient observed in growing dendrites (Hentschel & Fine, 1996), there is a small net influx I of calcium across the membrane at a rate proportional to the surface to volume ratio of each compartment [2]. Ca and $MAP2_u$ diffuse throughout the dendrite with rates D_{Ca}, D_u. $MAP2_u$ conversion into $MAP2_b$ is governed by rate constants c_1 and c_2; $MAP2_b$ conversion into $MAP2_p$ is calculated using c_3, c_4 and

[2]The influx is proportional to 1/r where r=dendrite radius. Surface area for spherical soma is $4\pi r^2$: volume is $4\pi r^3/3$. Ratio surface to volume is 3/r. For cylindrical dendrite: surface=$2\pi r\ l$, volume=$\pi r^2\ l$. Cylinder surface to volume =2/r

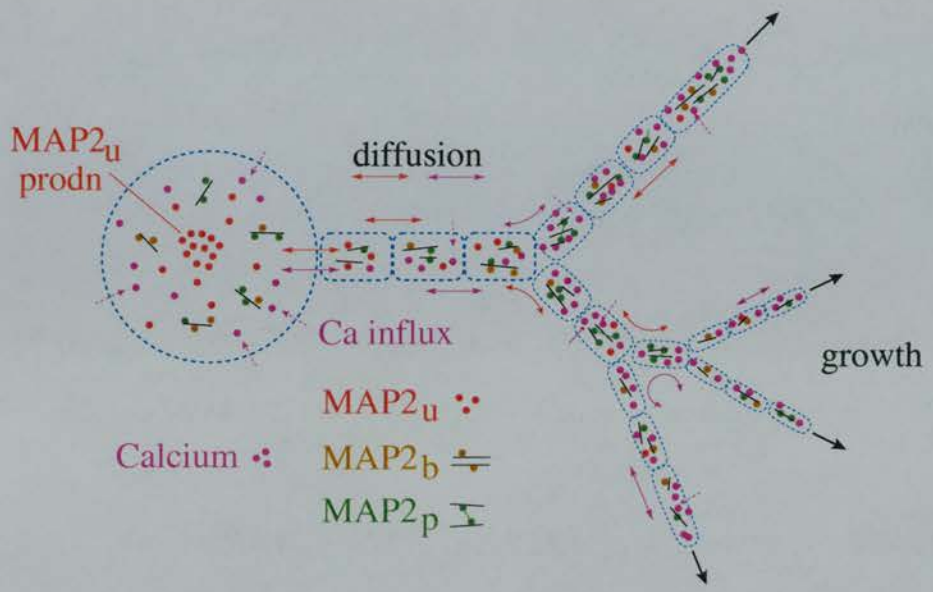

Figure 7.4: An intermediate state of the branching simulation. Each branch may be made up of several compartments of length, e.g. $5\mu m$. Terminal compartments then grow out to $10\mu m$ before being split into two compartments each of length $5\mu m$. $MAP2_u$ has diffused out from the soma and an increasing calcium gradient forms at the distal dendrites. The concentrations of $MAP2_b$ and $MAP2_p$ determine the rate of elongation and branching probability of the terminal compartment.

---

the (de)phosphorylation functions F and G (see below). Finally δ_{Ca} and δ_u, δ_b and δ_p determine the overall decay rate of calcium and MAP2. The model is shown at an intermediate stage of branching in Figure 7.4.

In addition to the parameters in the equation scheme the following parameters were used in the simulation runs:

branchPower b The ratio of the diameter of the daughter dendritic segments (d_l, d_r) to the parent segment (d_p) following branching: $d_l = d_r = b \times d_p$. When creating new daughter segments, the total volume of the end compartment of the parent segment is conserved (see Figure 7.2c) (Default b=0.9).

BranchRate A constant which determines the initial probability of branching per μm of dendrite elongation..

BranchProbability The overall probability that a terminal segment branches in one timestep, dt, is the product of 3 factors: the BranchRate, the amount of elongation during dt and the dynamic branching function B described below (which varies with the ratio $MAP2_p/MAP2_b$). e.g. if a segment grows $0.01\mu m$ in dt and the BranchRate=$0.2/\mu m$ and B = 1 then the probability of branching is 0.01*0.2*1 = 0.002.

elongationRate A constant which determines the initial rate of elongation in μm/hr. Actual growth is a function of the amount of MAP2 (see below).

StartConc The starting calcium concentration in the soma and first dendrite compartment depends on the rate of calcium influx and decay however this was usually set to around 60nM.

dt The timestep for the simulation. This is usually set equal to the maximum timestep permitted by the stability conditions for the diffusion calculation ($dt \leq \frac{dx^2}{2D}$) (Press, Teukolsky, Vetterling, & Flannery, 1992). [3]

When setting these parameters the CaDiffusionRate, branchFactor, branchRate and elongationRate were all set to values from data taken from biological experiments. The ratio of constants c1:c2 was set so that most MAP2 was bound.

[3]Technical implementation point. In normal elongation the distance between the midpoints of neighbouring compartments was used in the diffusion calculation. As the length of terminal compartments $\geq dx$ and the length of non-terminal compartments $= dx$, the distance between the midpoints of compartments is also $\geq dx$. However when a terminal segment branches, the newly created daughter segments have a length $L_{daughter} = \frac{L_{terminal}}{2b^2}$ where $b = branchPower$. In some cases $L_{daughter} < dx$. As a result the distance between the midpoint of the terminal and daughter compartments may be $< dx$. At the start of the simulation the timestep dt was set to a value which ensured that the diffusion calculation remained stable following branching.

The ratio of constants c3:c4, and de/phosphorylation functions F and G was varied to determine the different effect of MAP2 phosphorylation status on elongation and branching. The total number of constants above can be reduced by combining the production constants and decay constants. This was done in the simulations (see Equations 7.6 and 7.10).

7.4.3 Model development

Two versions of the model were developed - a linear, and a non-linear model. The linear model was the first version of the model to be implemented. Changes to this were subsequently made which resulted in the non-linear model. Both models have essentially identical reaction schemes and differ only in the following areas:

- The MAP2 phosphorylation/dephosphorylation functions.
- The functions controlling the elongation rate and branching probability in terms of $MAP2_b$ and $MAP2_p$.

The modifications to the linear-model were made primarily in order to balance the types of de/phosphorylation function used. A consequence of this was that a wider range of dendritic tree topologies could now be simulated. The differences between the two models are now as follows.

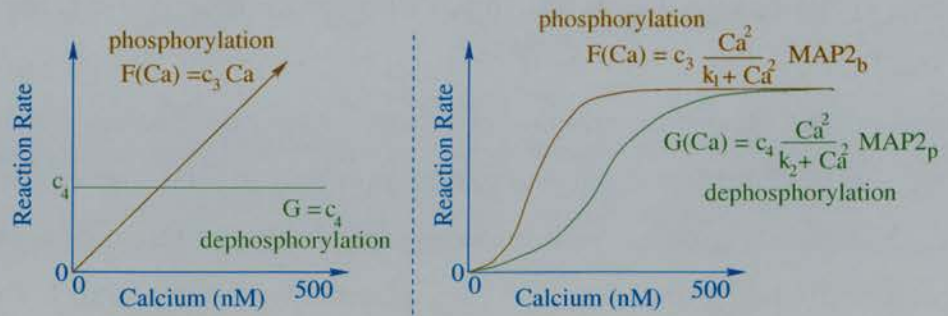

Figure 7.5: (a) Phosphorylation functions in the linear model. (b) Phosphorylation functions in the non-linear model

7.4.4 The linear model

In the linear model the phosphorylation function $F = k_F Ca$ which controls the rate of $MAP2_b \rightarrow MAP2_p$ conversion was linearly dependent on calcium. The dephosphorylation function $G = k_G$ controlling the reaction $MAP2_p \rightarrow MAP2_b$ was independent of calcium. Equations 7.4 and 7.5 can then be written:

$$\frac{\partial MAP2_b}{\partial t} = c_1 MAP2_u + c_4 MAP2_p - MAP2_b(c_2 + c_3\, Ca - \delta_b) = 0 \quad (7.6)$$

$$\frac{\partial MAP2_p}{\partial t} = c_3\, Ca\, MAP2_b - MAP2_p\,(c_4 + \delta_p) = 0 \quad (7.7)$$

As $MAP2_b$ and $MAP2_p$ are in equilibrium, it is possible to rewrite them directly in terms of $MAP2_u$ and calcium concentration (see Appendix A).

In the linear model the dendritic growth rate and branching probability ($P_{branching}$) were defined as follows.

$$elongation = elongationRate \times k_E \times \frac{MAP2_b}{MAP2_b + MAP2_p} \quad (7.8)$$

$$P_{branching}/\mu m = branchingRate \times k_B \times \frac{MAP2_p}{MAP2_b + MAP2_p} \quad (7.9)$$

Constants k_E, k_B ensure that at t=0, initial elongation (in $\mu m/s$) = elongationRate, and that the initial branching probability (per μm of dendrite growth) = branchingRate. These functions were chosen as (a) the higher the ratio of $MAP2_b/MAP2_p$ the higher the elongation rate and (b) the higher the ratio $MAP2_p/MAP2_b$ the greater the branching probability. In this model the relative ratio of the two substances was the determining factor rather than their absolute value which is divided out. The same growth and branching rates occur with $MAP2_b : MAP2_p$ values of 100:200 or 1:2. This means that the total rate of elongation and branching is approximately conserved. High branching rates are concurrent with minimal elongation and vice-versa.

The dendritic trees generated by the computer simulation of the above equations are plotted in the Results section. The Results section also includes a theoretical analysis of how the growth rate and branching probability vary with calcium concentration. This allows the general characteristics of the model to be interpreted in a simple manner.

7.4.5 The non-linear model

In the linear model the MAP2 phosphorylation function F increased linearly with calcium. The dephosphorylation function G was calcium-independent. I was informed[4] that the function simulating the effect of a dephosphorylation agent such as calcineurin should also be calcium activated. Figure 7.6 shows this part of the reaction scheme. The biochemical reaction for this is:

$$MAP2_{P_N} + H_2 \rightarrow MAP2_{P_{N-1}} + PO_4^{3-} \tag{7.10}$$

$$MAP2_{P_{N-1}} + ATP \rightarrow MAP2_{P_N} + ADP \tag{7.11}$$

[4] V.Steuber personal communication.

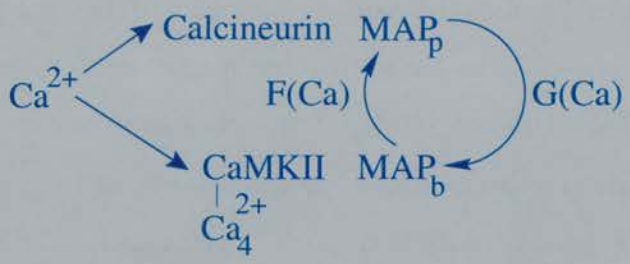

Figure 7.6: Diagram showing the MAP2 phosphorylation/dephosphorylation reaction scheme.

In the non-linear model both the phosphorylation function $F = \frac{Ca^2}{k_F + Ca^2}$ and dephosphorylation function $G = \frac{Ca^2}{k_G + Ca^2}$ were calcium dependent. These functions have the sigmoidal shape shown in Figure 7.5(b) and saturate towards an upper limit rather than increasing indefinitely (k_F, k_G control the steepness of the slope of these curves.) This reflects the finite amount of MAP2 and CaMKII complex found within the dendrites. Equations 7.4 and 7.5 then become:

$$\frac{\partial MAP2_b}{\partial t} = c_1 MAP2_u + \frac{c_4\, Ca^2 MAP2_p}{k_G + Ca^2} + MAP2_b(c_2 + \frac{c_3\, Ca^2}{k_F + Ca^2} + \delta_b) \quad (7.12)$$

$$\frac{\partial MAP2_p}{\partial t} = \frac{c_3\, Ca^2}{k_F + Ca^2} MAP2_b - MAP2_p(\frac{c_4\, Ca^2}{k_G + Ca^2} + \delta_p) = 0 \quad (7.13)$$

The parameters k_F, k_G control the steepness of the slope of the curves. In the simulation $MAP2_b$ and $MAP2_p$ are calculated directly in terms of $MAP2_u$ and Ca (see Appendix A).

7.4.6 Elongation and branching.

At each timestep the elongation rate and branching probability, $P_{branching}$, of each dendritic terminal is calculated. The simulation was initially run for 10000 timesteps without any elongation to eliminate any start up effects and to ensure that the system was at equilibrium before elongation began. The rate of

elongation is proportional to the ratio $\frac{MAP2_b}{MAP2_p}$. The higher the ratio of bound to dephosphorylated MAP2, the faster the elongation. In contrast, the probability that a terminal dendritic compartment branches into two daughter segments in any given timestep is proportional to the inverse ratio $\frac{MAP2_p}{MAP2_b}$. These ratios were multiplied by the absolute values of $MAP2_p$ and $MAP2_p$ respectively, to reflect the fact that a physical amount of MAP2 is required for elongation or branching to occur. The probability that a terminal segment branches in one timestep, dt, is the product of the branching probability per unit length and the elongation during that timestep where:

$$elongation = elongationRate \times k_E \times MAP2_b \frac{MAP2_b}{MAP2_p} \quad (7.14)$$

$$P_{branching}/\mu m = branchingRate \times k_B \times MAP2_p \frac{MAP2_p}{MAP2_b} \quad (7.15)$$

These equations allow a varied range of different growth speeds and branching rates. If both $MAP2_b$ and $MAP2_p$ have equal high concentrations, rapid branching and growth will occur simultaneously. Conversely slow growth and branching can take place at low concentrations.

7.5 Results

7.5.1 The Linear Model

The time sequences of development of three cells are shown in Figures 7.7 - 7.9. All parameters in the 3 plots are the same except for the value of the de/phosphorylation rate constants c_3 and c_4. The value of the other simulation parameters are as given above. (n.b. In these simulations the time units are

arbitrary as the probability of branching varies with the growth in μm of the dendrite and not with actual time elapsed.)

Figure 7.7 shows the development of a cell where the rate of phosphorylation (c_3Ca) and dephosphorylation (c_4) are equal at a calcium concentration of 100nM ($c_3 = 0.005$, $c_4 = 0.5$). The dendritic tree produced with this simulation has long primary dendrites with heavier branching amongst distal segments.

Figure 7.8 shows the development of a cell with phosphorylation reaction rates $c_3 = 0.01, c_4 = 0.1$. At 100nM calcium the forward phosphorylation reaction is ten times that of the dephosphorylation reaction. As a result the dendrite grows out at a slower rate and branches more often. In contrast Figure 7.9 shows the development of a dendrite where $c_3 = 0.001$ and $c_4 = 1$. In this case the dephosphorylation reaction dominates and the dendritic branches elongate rapidly with a lower probability of branching.

The following section compares the characteristics of trees produced by the simulation with a theoretical analysis of the model equations. This theoretical analysis explains in more detail why the dendritic trees in Figures 7.7-7.9 have their respective geometries. This analysis also highlights fundamental limitations of the linear model in explaining experimental observations of biological dendrites.

7.5.2 Analysis of dendritic tree characteristics of the linear model

It is possible to analyse how the growth rate and branching probability vary directly with calcium. The analysis cannot determine the exact form of the

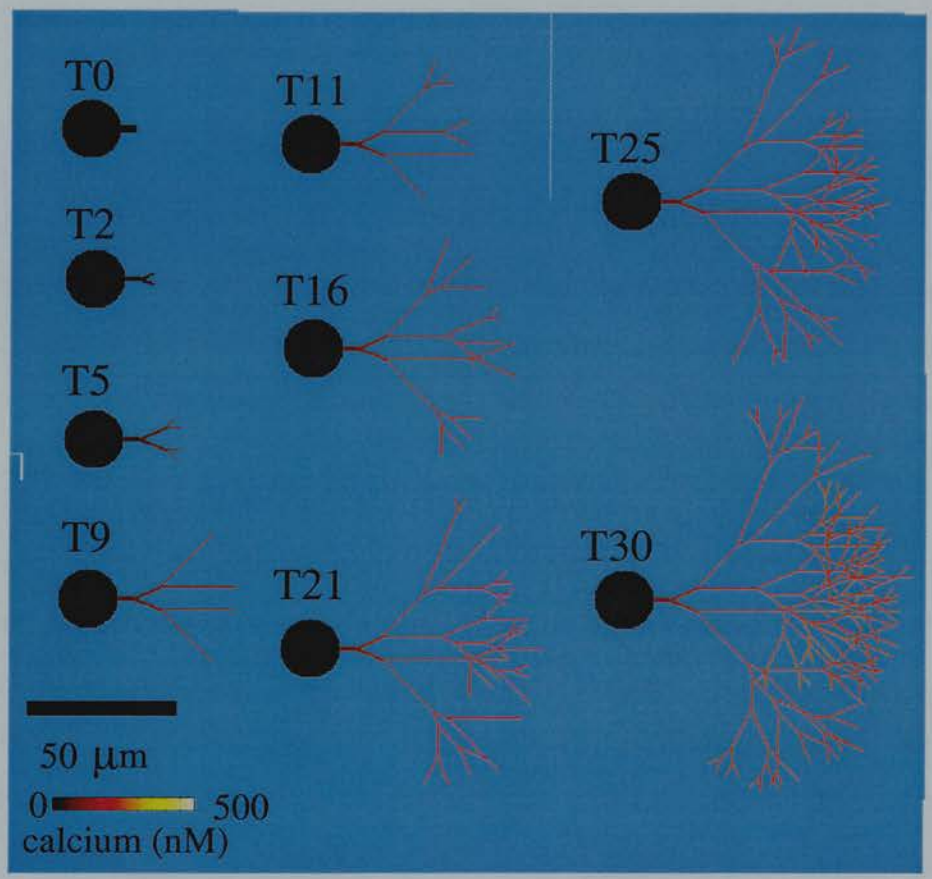

Figure 7.7: A typical dendritic arbor produced by the linear model. The rates of MAP2 phosphorylation and dephosphorylation are approximately equal ($c_3Ca = c_4 = 0.5$ at 100nM calcium)

simulated dendritic tree, but it gives an indication of the range of growth and branching patterns that are possible with the linear model.

From equation 7.7 it is possible to get the ratio R = $\frac{MAP_p}{MAP_b}$ in terms of calcium and the constants c_3, c_4 and the decay parameter δ_p.

$$R = \frac{MAP2_p}{MAP2_b} = \frac{c_3Ca}{c_4 + \delta_p} = \frac{c_3}{c_4}Ca \tag{7.16}$$

where the small decay term δp can be neglected. Equations 7.8 and 7.9 can be written in terms of R by multiplying top and bottom by $\frac{1}{MAP2_b}$ and simplifying.

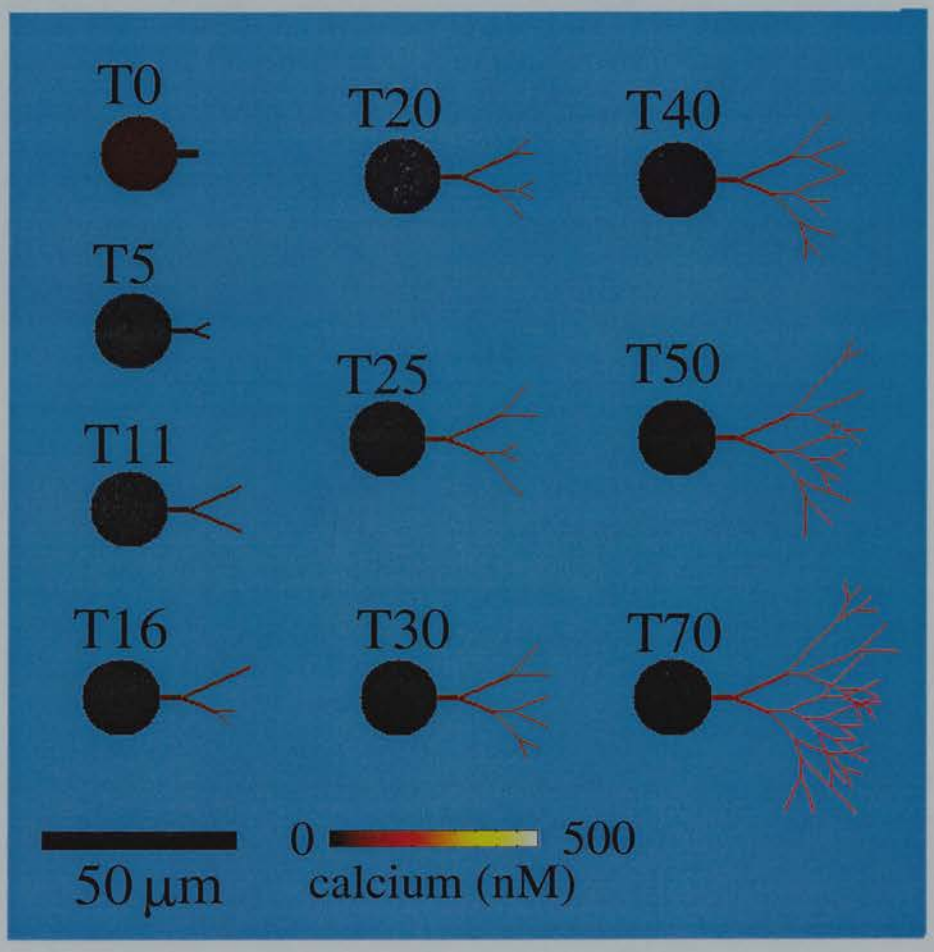

Figure 7.8: A stunted and more heavily branched dendritic arbor created by an increase in the rate of MAP2 phosphorylation rate (c_3Ca=1, c_4=0.1 at Ca=100nM).

$$
\begin{aligned}
growth\ rate &= growth\_constant \times \frac{MAP2_b}{MAP2_b + MAP2_p} \times \frac{\frac{1}{MAP_b}}{\frac{1}{MAP_b}} && (7.17)\\
&= constant \times \frac{\frac{MAP2_b}{MAP2_b}}{\frac{MAP2_b}{MAP2_b} + \frac{MAP2_p}{MAP2_b}} && (7.18)\\
&= constant \times \frac{1}{R+1} && (7.19)\\
&= \frac{1}{\frac{c_3}{c_4} Ca + 1} && (7.20)
\end{aligned}
$$

where the linear growth constant has been dropped. The growth rate is now a

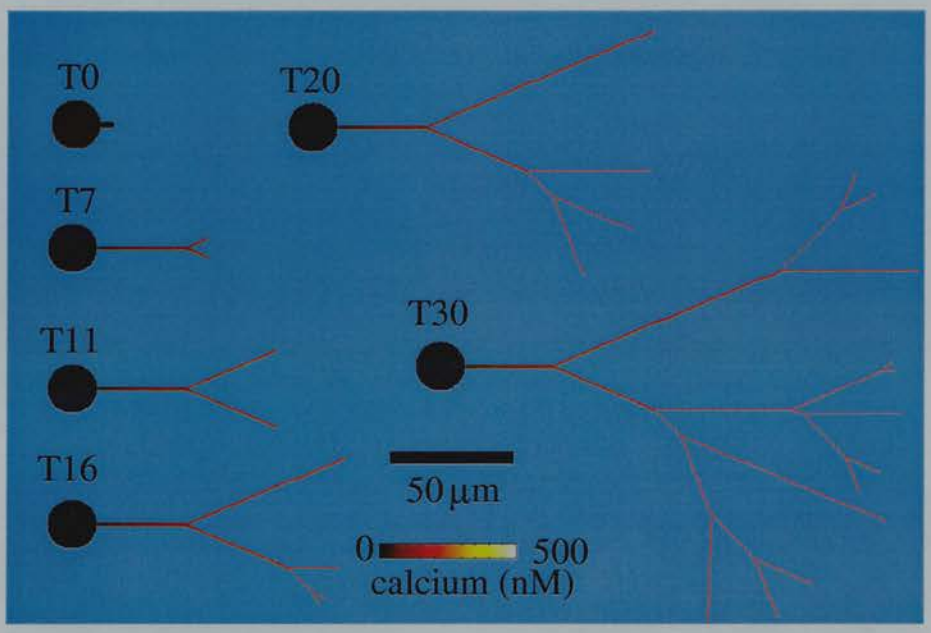

Figure 7.9: An elongated and larger dendritic tree with fewer branches is produced by an increase in the rate of MAP2 dephosphorylation ($c_3Ca = 0.1, c4 = 1$ at 100nM calcium).

---

function of calcium and the phosphorylation rate constants c_3 and c_4. Similarly the rate of branching can be written as:

$$growth\ rate = growth\_constant \times \frac{MAP2_p}{MAP2_b + MAP2_p} \times \frac{\frac{1}{MAP_b}}{\frac{1}{MAP_b}} \quad (7.21)$$

$$= constant \times \frac{\frac{MAP2_p}{MAP2_b}}{\frac{MAP2_b}{MAP2_b} + \frac{MAP2_p}{MAP2_b}} \quad (7.22)$$

$$= constant \times \frac{R}{R+1} \quad (7.23)$$

$$= \frac{\frac{c_3}{c_4} Ca}{\frac{c_3}{c_4} Ca + 1} \quad (7.24)$$

Both the growth rate and branching probability can now be plotted directly against calcium and the phosphorylation constants c_3 and c_4. The overall growth effect of the phosphorylation constants on the shape of the dendritic tree can now be analysed. This is plotted in Figure 7.10. N.B. as calcium increases distally away from the soma, a higher calcium concentration indicates

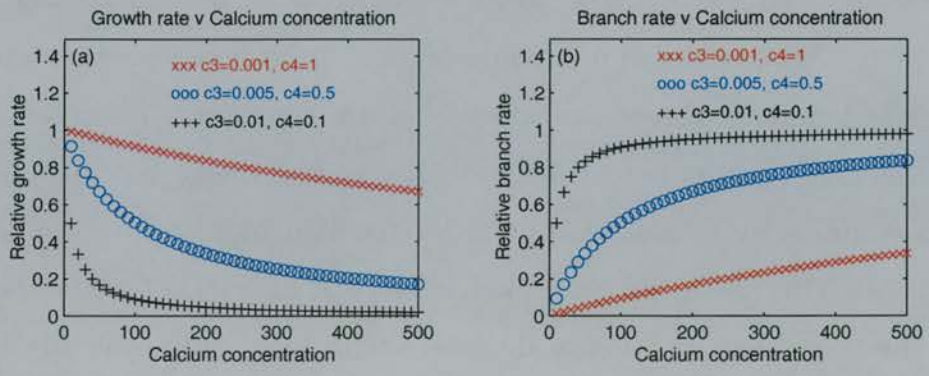

Figure 7.10: The figure plots the growth rate and branching probability as a function of calcium. For all values of the constants c_3 and c_4 and with an increasing calcium concentration - (i) the growth rate (solid lines) decreases from its initial maxium and (ii) the branching probability (dashed lines) asymptotically increases to a constant value from an initial minimum.

---

a more distal position in the dendritic tree and a later time in development. Thus the calcium axis in Figure 7.10 also effectively plots the developmental time course of the growth and branching rates in the dendritic tree.

A number of important points can be inferred from Figure 7.10. It can be seen from the graph that the maximum growth (and minimum branch rate) occurs at low calcium concentrations. This will take place during initial dendritic elongation from the soma. As the calcium concentration increases, the growth rate decreases, and the branching increases. Although the functions in Figure 7.10 are different, the overall shape of the dendritic tree generated by these functions is qualitatively the same whether the on rate of phosphorylation (c_3) is greater than, equal to, or less than the off rate of dephosphorylation (c_4). The longest dendritic branches will be the main dendritic branches (starting from centrifugal order 0) whilst the shortest dendritic segments will occur at the tips of the dendritic tree. This shape will be unaffected by any change in the phosphorylation reaction rates c_3 and c_4 or changes in the absolute amount of dendritic MAP2 produced by altering c_1 or c_2. Changing the rate of MAP2 or calcium diffusion, or calcium influx, will simply alter the height of the curves

but not their general shape. The only form of dendritic tree which can be produced by this model has an increasing branching probability with increasing centrifugal order. However the opposite effect is generally observed in biological dendritic arbors (van Pelt et al., 1997). The distal dendrites of sympathetic neurons in culture tend to be longer than more proximal dendrites (Bray, 1973). This result is a general characteristic of a wide range of neurons where the branching probability decreases with increasing centrifugal order (van Pelt & Uylings, 1997). The linear model is only able to produce a limited range of dendritic characteristics, and is unable to account for the dendritic arbors of most experimentally observed cells. These limitations are overcome in the non-linear model.

7.5.3 Dendritic trees produced by the non-linear model

The model was used to construct a variety of dendritic trees, and to reproduce the characteristics of a specific data set obtained from rat pyramidal basal dendrites (Larkman, 1991).

Different Tree Geometries

Figures 7.11(a-e) and 7.12(a-c) show a range of different dendritic trees produced by the non-linear model.

As can be seen, a wide range of different topologies can be produced, ranging from trees with long proximal segments and heavily branched, short outer segments to trees where the dendrite length increases distally. Figures 7.11(a,d)

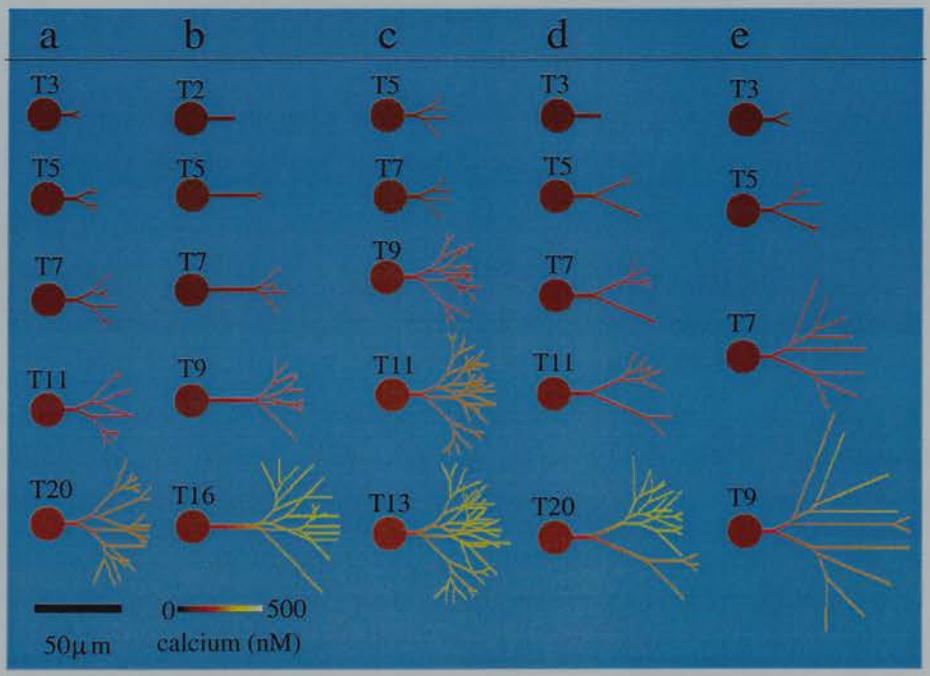

Figure 7.11: Dendritic arbors produced by the non-linear model. This model is able to generate a wider range of dendrites than the linear model by varying the de/phosphorylation reaction rates c_3, c_4 and paramters k_F, k_G which alter the shape of the de/phosphorylation functions F(Ca) and G(Ca). In (a) and (d) the branch probability increases distally and the initial branching probability ($0.1/\mu m$) was half the default value ($0.2/\mu m$)). In (b) and (e) the branch probability decreases distally. In (c) the branch probability remains approximately constant. Default simulation parameters unless otherwise stated: c_3=1, c_4=1, k1=1000, k2=1000 (a) c_3=2, k1=5000. (b) c_3=1.5, k2=5000. (d) c_3=0.75, k1=10000. (e) c_3=0.1, k2=10000.

have similar characteristics - in both simulations the branching probability increases with increasing centrifugal order (similar to the results obtained with the linear model).

The characteristics of the dendritic trees shown in Figures 7.11(b,e) are essentially the reverse of those shown in Figures 7.11(a,c,d). In both (b) and (e) the distal segments are longer than the proximal segments, implying that the branching probability decreases away from the soma (as seen in biological dendrites). In this case, the increased calcium leads to an increase in the rate of $MAP2_p$ dephosphorylation in distal dendrites. The resulting increase in the

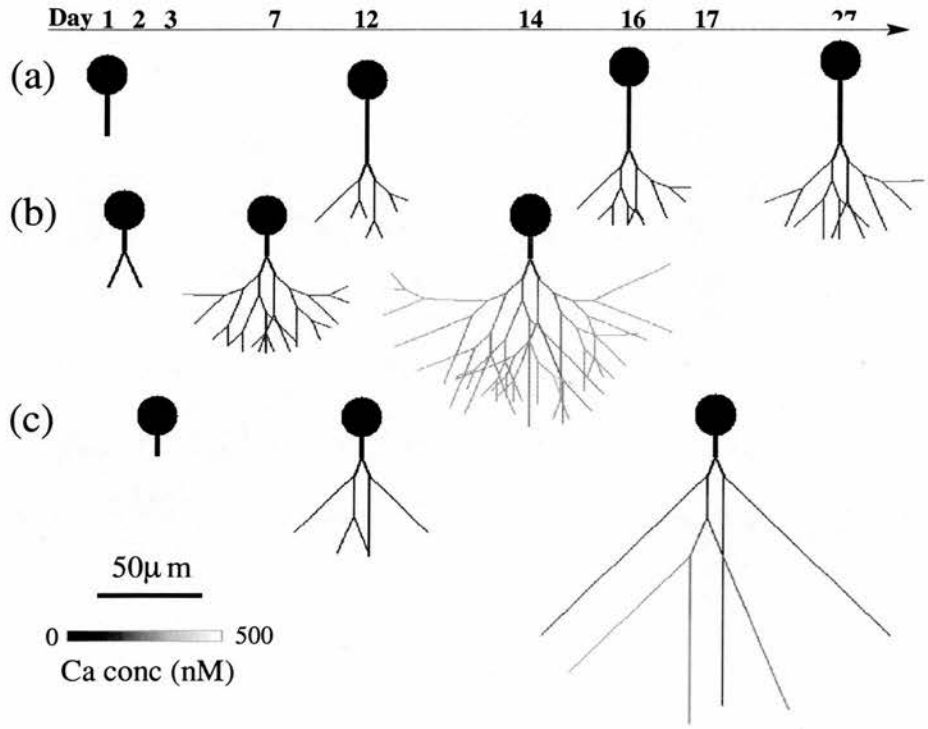

Figure 7.12: Dendritic arbors produced by the non-linear model. This model is able to generate a wide range of dendrites by varying the (de)phosphorylation reaction rates c_3, c_4 and parameters k_F, k_G which alter the shape of the (de)phosphorylation functions F and G. In (a) the branch probability is low initially ($0.015/\mu$m) and increases with time. In (b) the branching probability ($0.2/\mu$m) is approximately constant throughout. In (c) the branching probability is initially high ($0.6/\mu$m) and falls off rapidly as the dendrite grows. The default parameter values are: dx=10μm, dt $\approx$ 40s, somaRadius=10μm, dendriteRadius=1μm, initial growthRate=$2\times10^{-4}\mu$m/s, branchAngle=20^o, branchPower=0.8, c_1=0.95, c_2=0.05, c_3=c_4=0.8, δ_{Ca}=10^{-4}/s, $\delta_{u,b,p}$=10^{-5}/s, CaStartConc=30nM, $MAP2_u StartConc$=10, I=0.01nM/μm s, P=0.003/s, D_{Ca}=D_u=1μm^2/s, k_F=k_G=1000. In (a) c_4=0.2, k_F=20,000, growthRate=$5\times10^{-5}\mu$m/s; in (c) c_3=0.2, k_G=40,000, growthRate=$4\times$ $10^{-4}\mu$m/s.

ratio of $MAP2_b/MAP2p$ results in significantly longer dendrites as development proceeds. In these simulations both an increase in the rate of elongation, and a decrease in the probability of branching, contribute to the overall shape of the dendrites. As well as an increase in the length of the distal segments compared to the proximal ones, the overall size of the dendritic trees in Figure 7.11(b,e) is larger, and the time taken to reach this size is shorter than than the

other dendrites shown in Figures 7.11(a,c,d).

Figure 7.12(a-c) shows the time course of development of three characteristic dendritic arbors produced by the model. Figure 7.12(a) shows the type of dendritic branching pattern observed in cultured hippocampal neurons (Diez-Guerra & Avila, 1993). In this simulation the initial branching probability is low as at low calcium concentrations dephosphorylation is greater than phosphorylation ($k_F = 20,000 > k_G = 1000$. See Fig. 2). An increase in the distal calcium concentrations causes increased MAP2 phosphorylation which leads to an increased branching probability amongst distal dendrites. The Purkinje cell is an extreme example of a cell which might employ this type of branching mechanism (although external factors also play a significant role in its development (Schilling *et al.*, 1991)). Figure 7.12(b) shows the typical branching structure produced when the branching probability and elongation rate remain (approximately) constant throughout the simulation. In this simulation the (de)phosphorylation constants are equal (k_F=k_G=1000). The ratio $\frac{MAP2_b}{MAP2_p}$ remains constant and the elongation and branching rates are unaffected by distal increases in calcium concentration. However both the rate of elongation and the branching probability decrease slowly with increasing distance from the soma due to a lack of available MAP2.

7.5.4 Analysis of the Non-Linear Model

A similar analysis to the one used above for the linear model can be applied to the non-linear model. However, although the ratio R = $\frac{MAP2_p}{MAP2b}$ can be calculated, it is not possible to get the growth and branching rate directly in terms of calcium and constant parameters. (As no information about the individual

concentrations of $MAP2_b$ and $MAP2_p$ can be obtained from knowing the ratio.) However knowing R gives an indication of the variety of dendritic topologies that can be produced by the model.

From equation 7.13 the ratio $\mathbf{R} = \frac{MAP_p}{MAP_b}$ can be calculated in terms of Ca and the constants c_3, c_4 again neglecting the small decay constant δp.

$$\frac{MAP2_p}{MAP2_b} = \frac{\frac{c_3 Ca^2}{k_1 + Ca^2}}{\frac{c_4 Ca^2}{k_G + Ca^2}} = \frac{c_3(k_G + Ca^2)}{c_4(k_1 + Ca^2)} \tag{7.25}$$

This ratio is plotted against an increasing concentration of calcium in Figure 7.13 for various values of c_3, c_4, k_F and k_G.

Figure 7.13 plots the effective rate of branching (or the inverse of elongation) against calcium concentration. The actual branching rate is obtained in the simulation by multiplying this ratio by the physical amount of $MAP2_p$. This has a maximum concentration in the soma and a decreasing value as it diffuses out into the distal dendrites. As a result the ratio of $MAP2_p/MAP2_b$ overestimates the actual amount of dendritic branching. In the most distal segments the branching probability will decrease to 0. This will be matched by a decrease in elongation rate as this is affected by the physical concentration of $MAP2_b$. This ensures that the dendrite is not able to grow indefinitely.

On the left hand side of the graph, the branching probability at low concentrations of calcium ($Ca \to 0$) is obtained from equation 7.25. This gives a starting value of $\frac{c_3 k_G}{c_4 k_F}$. At high values of calcium, the curves tend towards a limiting value of $\frac{c_3}{c_4}$. This indicates that the parameters k_F, k_G which determine the shape of the de/phosphorylation curves can have a significant effect on the overall geometry of the tree (in contrast to the linear model).

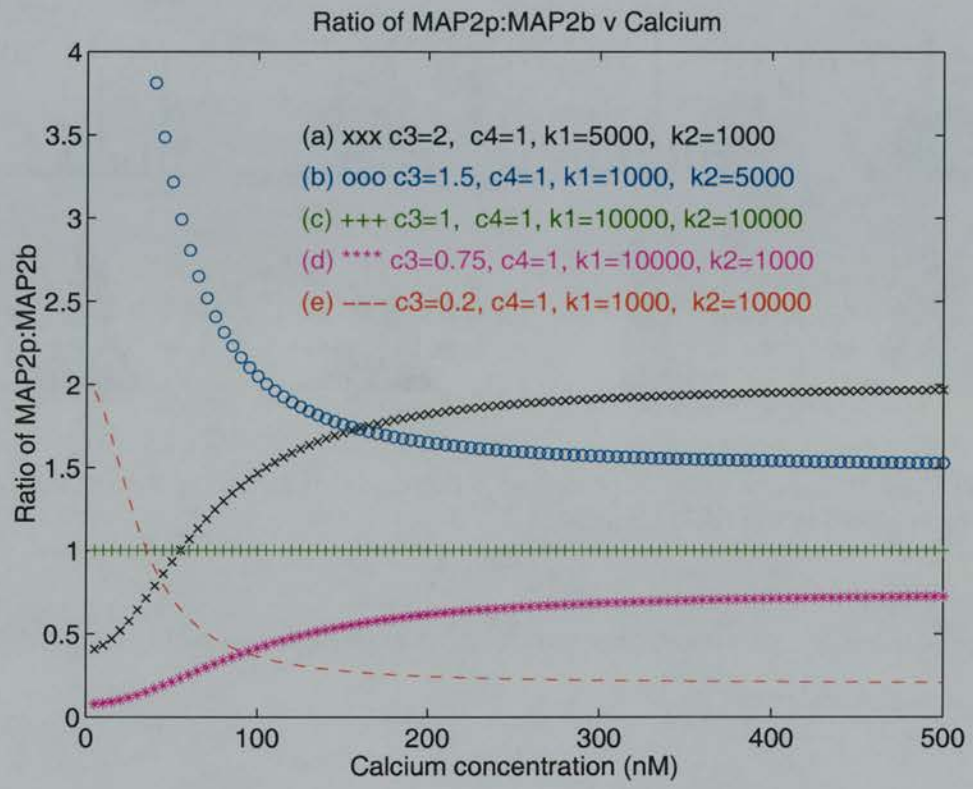

Figure 7.13: Theoretical analysis of possible branching patterns for the non-linear model. The figure plots the ratio of $MAP2_p$:$MAP2_b$ as a function of calcium for various values of the rate constants c_3, c_4, k_F and k_G. The rate of branching is proportional to this ratio times the concentration of $MAP2_p$. The effective rate of branching is not restricted to a linear increase with calcium. Branching can be high initially and then fall (producing a tree with longer distal segments) or low and then rise (producing densely branched distal segments). A wide range of different geometries can be generated depending on the values of the rate reaction parameters (see text).

Curves (a) and (d) corresponding to the dendritic trees (a) and (d) in Figure 7.11 have a low value of the branching ratio $MAP2_p/MAP2_b$ at low values of calcium. This reaches a constant high level with increasing levels of calcium. This occurs at the distal dendrites as the dendritic tree develops. In contrast curves (b,e) simulate the parameters of the trees in Figures 7.11. In both of these dendrites, elongation increases with development leading to shorter proximal, and longer distal segments. This is a general property of biological neurons. The next section describes the results of a comparison between the dendritic

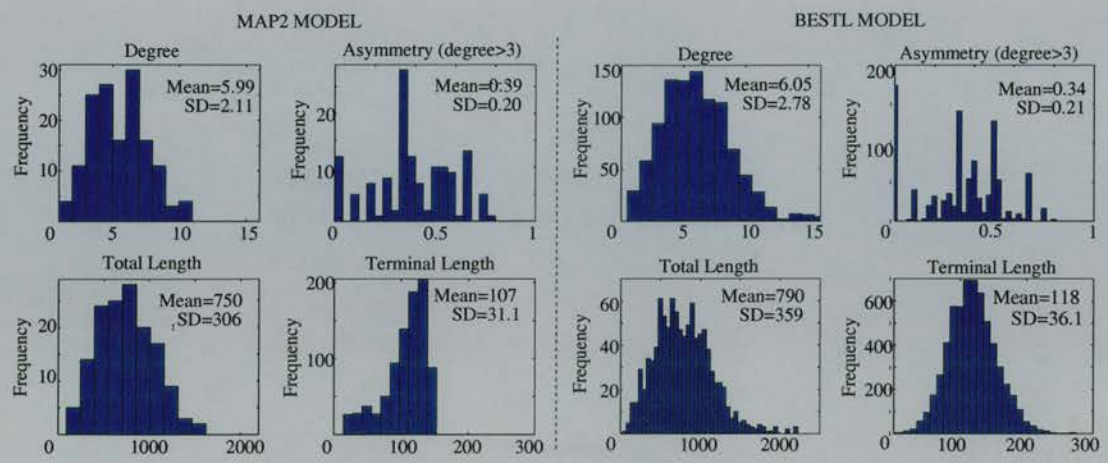

Figure 7.14: Characteristics topologies of dendritic trees generated by the MAP2 model compared to the BESTL model.

tree produced by the non-linear model and experimental data from rat pyramidal basal dendrites.

7.5.5 Comparison with biological dendrites

In contrast to the linear model, the non-linear model is able to produce dendritic trees with a decreasing probability of branching. This corresponds to the biological observations where branching probability decreases with increasing centrifugal order, e.g. in sympathetic neurons in culture (Bray, 1973). Figure 7.12(c) shows the dendritic arbor generated by the model when simulating the basal dendrites of a rat pyramidal neuron.

There are a small number of terminal segments (average six) which are over six times as long as the proximal segments. The form of the functions which model the effect of calcium on MAP2 (de)phosphorylation is crucial in determining the type of dendritic arbor generated. In contrast to Figure 7.12(a), in this simulation the (de)phosphorylation parameters ($k_G = 40000 > k_F = 1000$,

see Fig. 2) promote elongation and inhibit branching at low calcium concentrations. The increased calcium concentration in distal dendrites leads to an increase in the rate of $MAP2_p$ dephosphorylation and in the ratio of $\frac{MAP2_b}{MAP2p}$. This results in longer distal dendrites and a larger overall dendritic tree than in either Figure 7.12(a) or (b).

In order to quantify the type of dendritic arbor, a number of features can be used to determine the characteristic properties of the arbor. These include the total number of terminals per dendritic branch (also called the **degree** of the dendrite) and the tree-**asymmetry** index A_t [5]. The asymmetry index varies between zero and one and is a measure of how symmetrical the branching of the dendritic tree is. A value of zero implies the tree is maximally symmetric whilst a value of one implies maximal asymmetry. Other parameters are the intermediate and terminal segment length, total segment length and pathlength from the soma to distal tips.

Table 7.1 compares the average values of the tree characteristics obtained from 150 simulation runs with parameters as in Figure 7.12(c).

It can be seen that the mean and standard deviation of the simulated tree parameters closely match those of the biological data set. The full set of results produced by the MAP2 simulation is plotted in histogram format in Figure 7.14. This can be compared against the results produced by the BESTL model

[5]The tree-asymmetry index A_t of a tree with n terminal segments is given by:
$A_t = \frac{1}{n-1}\sum_{j=1}^{n-1} A_p(r_j, s_j)$. Each branch point can be considered as the start of a new dendrite with asymmetry A_p defined as
$A_p(r,s) = \frac{\|r-s\|}{r+s-2}$ for r+s >2, where r and s denote the number of terminal segments in the two subtrees. A_t is then the sum of the asymmetry values of the dendrite defined as the higher order segments at every branch point. By definition $A_p(1,1) = 0$. (Adapted from van Pelt and Uylings (1997)).

Shape variables	Biological Data	Simulation Data
Degree[1]	6.0 ± 2.7	5.99 ± 2.1
Asymmetry[2]	0.38 ± 0.22	0.39 ± 0.20
Total Length[3]	777 ± 342	749 ± 306
Terminal Length[1]	117 ± 33	107 ± 31
Intermediate Length[1]	15.4 ± 13.4	22.4 ± 19.5
Pathlength[1]	156 ± 29	161 ± 15

Table 7.1: Comparison between dendritic tree characteristics of MAP model and of rat basal dendrite data (mean $\pm$ S.D). [1] Larkman (1991); [2] van Pelt *et al.* (1992); [3] van Pelt & Uylings (1997).

with parameters optimized against the data from rat pyramidal cell basal dendrites (van Pelt & Uylings, 1997). [6]

7.6 Discussion

7.6.1 Strengths, Weaknesses and Assumptions

The linear and non-linear models are the first models to simulate dendritic branching patterns based on MAP2 regulation of dendritic elongation and branching. In contrast to previous models, neurite branching and elongation are controlled by the same underlying mechanism. This occurs through dynamic changes in the ratio of dephosphorylated to phosphorylated MAP2 caused by a distally increasing calcium concentration. This simultaneously controls both the elongation rate and branching probability. The model is able to generate a variety of dendritic branching patterns which have a high similarity to the characteristics of biological arbors. These include dendrites where

[6]These results were reproduced in an equivalent simulation of the BESTL model by Graham, Hely, and van Ooyen (1998).

branching increases distally (c.f. cultured hippocampal neurons (Diez-Guerra & Avila, 1993)) or dendritic trees with elongated distal dendrites (pyramidal neuron basal dendrites). This suggests that cells with different dendritic geometries, such as pyramidal and Purkinje cells, may use the same fundamental elongation and branching mechanisms during development.

The first version of the model to be implemented was the linear model. In this model MAP2 phosphorylation was linearly dependent on calcium whilst dephosphorylation was calcium independent. The particular form of these functions resulted in an increased branch probability at increasingly distal segments. The theoretical analysis showed that this was true for all values of the phosphorylation rate constants. The linear model is only able to produce a limited set of branching patterns. It cannot reproduce biological dendrites which show a decrease in branching probability with increasing centrifugal order. This led to the development of the non-linear model.

In the non-linear model the functions F and G relating calcium with MAP2 (de)phosphorylation will strongly influence what type of branching pattern will occur. At high calcium concentrations any MAP2 phosphorylation by CaMKII will largely be cancelled out by a calcium dependent phosphatase such as calcineurin. To model I used sigmoidal (de)phosphorylation functions. The exact shape of these functions have yet to be determined experimentally but this would provide a rigorous test of the predictions of the model.

Different dendritic geometries can be achieved simply by varying the model parameters. The size and degree of the dendritic arbor is primarily affected by the initial elongation and branching rates. The constants k_F, k_G which control the slope of the MAP2 (de)phosphorylation functions F, G are also important as they determine whether branching is promoted or inhibited as the dendrite

grows and the calcium concentration increases distally. Increasing the rate of $MAP2_u$ or Ca diffusion leads to shallower concentration gradients. The same effect occurs by increasing the size of the soma as a large cell will have a greater buffering capacity than a small one. With rapid diffusion, any distal increase in calcium concentration would be buffered by the soma which acts as a sink. In the limit this would lead to constant rates of elongation and branching.

The non-linear model is able to capture the overall characteristics of rat pyramidal neuron basal dendrites (Larkman, 1991). Although the mean and standard deviation of the dendrite asymmetry of the simulated trees match the biological values (Table 7.1) the model generated significantly fewer symmetric trees (see Figure 7.14). The asymmetry effect which does occur is due to differences in the ratio of surface area to volume caused by the reduction in dendrite diameter following branching. In the simulations of the rat basal dendrites, increased branching occurs at lower calcium levels. As a result the larger, unbranched dendrite is slightly more likely to branch than the newly branched dendrite. This mechanism produces only a slight bias towards symmetrical trees.

One of the weaknesses of the current implementation of the model is that the minimum length of dendrite branches is limited to the length scale dx. To obtain results from multiple simulation runs, a length scale of 5μ m or 10μm was used. This allowed a larger value of dt to be used compared to simulation runs at a smaller length scale. At low branching probabilities ($P_{branching} < 0.1/\mu m$) there is little difference in the branching patterns produced by these simulations as compared to a simulation run where $dx = 1\mu m$. However with larger branching probabilities ($P_{branching} > 0.1/\mu m$), a smaller length scale (e.g. $dx = 1\mu m$) would result in more heavily branched dendritic arbors. In the simulation run which reproduces the rat, basal dendrite data, $dx = 10\mu m$ and the

initial $P_{branching} = 0.6/mum$. Although the value of $P_{branching}$ falls off rapidly with distance from the soma, the number of initial dendrite branches is dependent on the fact that the minimum segment length is $\geq 10\mu m$.

The pyramidal basal dendrites simulated by the model (e.g. Figure 7.12c) fail to produce the population of extremely long terminal segments (> 150 μm) observed in real cells. The model dendrites were generated in a single simulation run without modifying any parameters. In contrast the terminal length data in the BESTL model (van Pelt & Uylings, 1997) was created using separate branching and elongation phases. In the BESTL model the branching process is stopped at day 12 and the terminal segments grow out without branching to obtain the required distribution pattern. The observed differences in the distributions may result in part from the effect of an intrinsic elongation phase or by external influences.

Both the linear and non-linear model simulate the elongation and branching of the cell using only intrinsic signalling. However many dendritic branching patterns will be heavily modified by external influences. In hippocampal cells in culture an exponential increase in branching on day 3 occurs when the cells may begin to make significant synaptic connections (Diez-Guerra & Avila, 1993). Although the BESTL- model has been used to predict the shape of Purkinje cell dendrites (van Pelt et al., 1997), it is known that these cells are heavily dependent on their environment. The Purkinje dendrites grow through and synapse extensively with parallel fibres, the axons of the cerebellar granule cells. If these fibres are missing, the Purkinje dendritic arbor is stunted (Ito, 1984). Electrical activity is also crucial to the normal formation of Purkinje dendrites. If electrical activity is blocked, Purkinje cell dendrites are significantly elongated and branch less frequently than normal (Schilling et al., 1991). These results indicate that for many cells a large part of the final dendritic structure is heavily influenced by external factors.

At present the MAP model does not directly take into account such external factors. However the current model is not at odds with a branching mechanism which is influenced by external signals. The present model could be adapted to include the effect of external molecules such as chemoattractants on growth and branching, or the synaptic interactions of cells in a network. Any synaptic activity will have a significant effect on the calcium signalling pathways and the rate of MAP2 de/phosphorylation. The aim of the current model is to show how a characteristic branching template may by set up by the cell which may be modified or altered by environmental influences. It is not the aim of the model to suggest that control of the microtubule array through CaMKII phosphorylation of MAP2 is the only possible mechanism involved in dendritic development. However this model does provide a possible starting point for investigating how intrinsic and extrinsic factors combine to produce the characteristic dendritic branching patterns of neurons.

Chapter 8

Emergent firing synchronization in neuronal networks.

8.1 Introduction

In contrast to the previous chapters which concentrated on the single cell, this chapter deals with interactions between networks of developing neurons. In particular it introduces a new simulation of the phenomenon of emergent synchronization amongst developing cortical neurons in culture (Murphy, Blatter, Wier, & Baraban, 1992; Robinson et al., 1993). In these cultures the firing of the cells is initially random and spontaneous. As the culture develops, the activity of the cells in the network becomes synchronous and almost all cells fire at the same time and with the same frequency. At present the causes of this synchronization are still unclear.

The aim of the current simulations was to see if a revised version of a general model of synchronization was able to account for the emergent synchronization seen in developing neurons in culture. The model simulates a network of interacting cells using a limiting case of the Hodgkin-Huxley equation (Knight, 1972). The firing of one cell advances the firing of all other cells to which it is connected. Over a period of time these coupling interactions drive the network to synchrony through "indirect synchronization".

This system was previously used to investigate the behaviour of visual cells receiving external input in the horseshoe crab *Limulus* (Knight, 1972). It was then specifically adapted to account for the synchronization of cardiac pacemaker cells (Peskin, 1975). This model proved that coupling interactions could ensure the phase synchronization of two oscillating cells. More recently the method was extended and applied to general biological systems which display synchronization such as flashing fireflies or chirping crickets (Mirollo & Strogatz, 1990). However the following five key areas of the basic coupling mechanism were revised in order to develop a more biologically plausible model.

Revision 1. Spatial Position. In Mirollo and Strogatz (1990) the proof of network synchronization did not take into account the spatial position of the cells (each cell was considered to be the neighbour of every other cell and connected to all other cells.) The spatial position of each cell is taken into account in the new model.

- The amount of activity generated by the network is strongly dependent on the strength of coupling between cells. The effect of varying the coupling strength (parameter ϵ) on synchronization was analyzed for the original network.

Revision 2. Network Connectivity. The proof of firing synchronization of Mirollo and Strogatz (1990) only applies to fully connected networks and is not necessarily valid for partially connected networks (i.e. biological networks). The size of a cultured neuronal network can be approximately 1cm in diameter whilst the maximum extent of neuronal projections is only around $200\mu m$ (Maeda, Robinson, & Kawana, 1995). In these cultures, cells interact primarily through local connections and the network will only be partially connected. One of the key aims of the model was to determine whether synchronization was possible using the coupling method with partially connected networks of cells.

Revision 3. Chain-Reaction. In the original model, if a cell was pushed above threshold by the firing of a neighbouring cell, it was not able to fire until the next time-step. As the time scale for firing is very short ($< 10mS$ may separate the firing of cells up to 1mm apart) the new model examined the effect of relaxing this condition. With the "chain-reaction" condition on, a cell which was brought above firing in the current time-step was allowed to fire, and could also bring other cells above the firing threshold. The timestep was not advanced until there were no more cells which remained above their firing threshold.

Revision 4. Weighted Coupling. In the original model the strength of the coupling interactions was identical between all cells in the network. In contrast the strength of interactions between cultured neurons will depend on the overlap of their respective dendritic trees. This was introduced into the new model by weighting the coupling strengths between cells. Coupling between neighbouring cells was increased whilst coupling between more distant cells was reduced.

Revision 5. Firing Frequency. In the original model each cell in the network

fires at the same frequency. In the biological system the firing frequencies of different cells will vary due to differences in intrinsic pacemaking ability or in the input signals they receive.

Each of these revisions were implemented in the new model and the effect on the behaviour of the network was analysed. The analysis of the model shows that synchronization can occur through two different ways in this network - direct and indirect. Direct synchronization occurs with high values of coupling strengths between cells. In this system the firing of one cell causes a number of other cells to fire. The firing of these cells in turn then leads to the rapid onset of firing throughout the network (a "domino-effect"). In a network with low values of the coupling strength, indirect synchronization can take place. Under these circumstances, synchronization occurs due to the gradual coupling of cell phases over a large number of firing periods. This can take place in a partially-connected network where the cells may have non-identical coupling strengths and different firing frequencies. However the range of conditions under which indirect synchronization occurs is restricted. Analysis of the model suggests that the synchronization of neuronal cultures occurs through direct synchronization caused by the rapid propagation of high levels of neuronal activity.

8.1.1 Discrepancy between simulated and biological cells

In the model of Mirollo and Strogatz (1990), each unit in the network has an intrinsic pacemaking ability - whether it is a pacemaking cell, flashing firefly, or chirping cricket. After revising their model I discovered that the cultured neurons simulated in the current model do not display any signs of an intrinsic pacemaking potential (Robinson et al., 1993). It is unlikely that the original

coupling mechanism which causes indirect synchronization is appropriate in these circumstances. This is discussed in more detail in the conclusion. However the mechanisms underlying direct synchronization in the current model are still valid for this system. Direct synchronization is caused solely by the rapid spread of activity throughout the network and only requires a minimum network connectivity to ensure that activity is successfully propagated between neighbouring cells.

8.2 The role of synchronized activity in development

Activity plays a crucial role in the successful development and functioning of biological neuronal networks (Shatz, 1990). Synchronized activity in particular may be important in shaping the structure and function of certain areas of the brain. It has been proposed that the coupled activity of neuronal domains in the developing neocortex may serve as a blueprint on which adult functional areas are mapped (Yuste, Peinado, & Katz, 1992). Synchronized activity may have an important role in timekeeping general cognitive functions (Engel, Konig, Kreiter, Shillen, & Singer, 1992).

In the retina, ganglion cells undergo spontaneous activity during development long before external visual input is received (Meister, Wong, Baylor, & Shatz, 1991). The activity takes the form of a wave of excitation which spreads across the retina at a rate of around $100\mu m$ per second. These waves of activity have been implicated in the formation of a topographic map between the retina, lateral geniculate nucleus (LGN) and visual cortex. This synchronous activity disappears at the time of eye opening when external visual input refines those

connections that are already in place. It is not yet clear whether the exact form and timing of the retinal waves directly influences the formation of the ocular dominance columns seen in the visual cortex. However synchronous activity in one part of the brain may have a long range influence on the general development of other brain areas.

8.2.1 Synchronous activity in developing neuronal cultures

In cultures of developing neurons, extensive processes and functional synaptic connections are observed (Dichter, 1978). These cells are electrically active and their burst firing leads to an increase in the concentration of intracellular calcium. Optical recording of calcium can then be used to simultaneously monitor the activity of multiple neurons as they develop. Using this approach spontaneous synchronized transients of intracellular calcium have been observed in hippocampal neurons (Kudo & Ogura, 1986; Ogura, Iigima, Amano, & Kudo, 1987) and cortical neurons (Murphy et al., 1992; Robinson et al., 1993).

The initial activity of these neurons is varied but in general the firing behaviour of the neurons is random and uncorrelated. This spontaneous firing appears after about 3 days in vitro[1]. Over the course of about a week, the firing of individual cells is transformed progressively into synchronized bursting of the network. The synchronization time between the onset of firing in cells up to 1mm apart is only of the order of tens of milliseconds. During this period the calcium transients have a regular frequency and amplitude and occur every 10-20 seconds. These oscillations are stable for many weeks although the period of oscillations and propagation velocity of bursts gradually speeds up (from approximately 0.01 to 0.5Hz, and from 5 to 100mm/s respectively (Robinson

[1]Cells came from 17/18 day rat embryos.

et al., 1993)). This pattern of synchronized firing then develops into the mature firing pattern at around 4 weeks. In general the mature firing pattern is complex with single and multiple bursts occuring at non-periodic intervals.

The highly repetitive calcium oscillations seen over a period of many weeks in developing neuronal cultures may help to drive the growth and further differentiation of these particular cell types. Recently it was found that the survival rate of cultured cortical neurons which participated in synchronized activity were significantly more likely to survive than either (a) cells which were either inactive, or (b) cells which were active, but not involved in the synchronous activity of the network (Voigt, Baier, & de Lima, 1997). Thus the synchronous activity seen in the developing brain may play multiple but highly coordinated roles in the generation of adult neuronal connectivity.

8.3 A general theory of synchronizing oscillators

The new model that is introduced in the next chapter is an extension of a general **coupling model** of synchronization (Mirollo & Strogatz, 1990). This model in turn was based on a previous theoretical analysis of synchronized oscillatory activity in cardiac pacemaker cells (Peskin, 1975). It seemed that the coupling theory would be an appropriate theory to descibe the development of cortical neuronal cultures for the following reasons. Firstly the theory models the coupling interactions of identical excitatory units in a manner similar to those found in the neuronal cultures. Other models which have simulated emergent synchrony in locally coupled neural systems, e.g. (Konig & Schillen, 1991; Wang, 1995) are based on oscillations that occur through interactions between excitatory and inhibitory cells. These models are not applicable as there are no

inhibitory cells in these neuronal cultures. Secondly it has been proposed that this theory could account for the synchronization observed in other biological systems, such as networks of fireflies and crickets, and may also be appropriate for neuronal ensembles (Mirollo & Strogatz, 1990).

The coupling model consists of a network of N integrate-and-fire neurons with all-to-all connectivity. Each cell is characterised by a state x (corresonding to membrane potential) and phase ϕ both confined to values between 0 and 1. The neuron fires when $x \geq 1$ and both the phase ϕ and state x of the cell are immediately reset to 0. When one neuron fires it pulls up the phase of all the other neurons by an amount ϵ - the coupling factor. The dynamics of a single oscillator is shown in Figure 8.1. The function $f(\phi) = x$ describing the value of the membrane potential at a given phase has a concave form. This can be modelled using the equation

$$\frac{dx}{dt} = S_0 - \gamma x \tag{8.1}$$

The parameter S_0 can be either an external input received by the cell or an intrinsic pacemaking constant which leads to an increase in the potential of the cell. γ represents decay of potential with increasing depolarization (the "forgetfullness" of the neuron after it receives an input signal). This equation is a limiting case of the Hodgkin-Huxley equations (Knight, 1972). [2]

Figure 8.2 shows the coupling interactions of 2 oscillating cells. Both oscillators can be considered as points moving to the right along the fixed curve $x = f(\phi)$. In Figure 8.2a, oscillator A has just fired and its state has been reset to 0. Figure 8.2b shows the state of the system just before oscillator B fires. The phase difference of the oscillators is the same as in (a). In Figure 8.2c, oscillator B has

[2]It was first used to describe the behaviour of eccentric visual cells in the horseshoe crab *Limulus Polyphemus* (Knight, 1972).

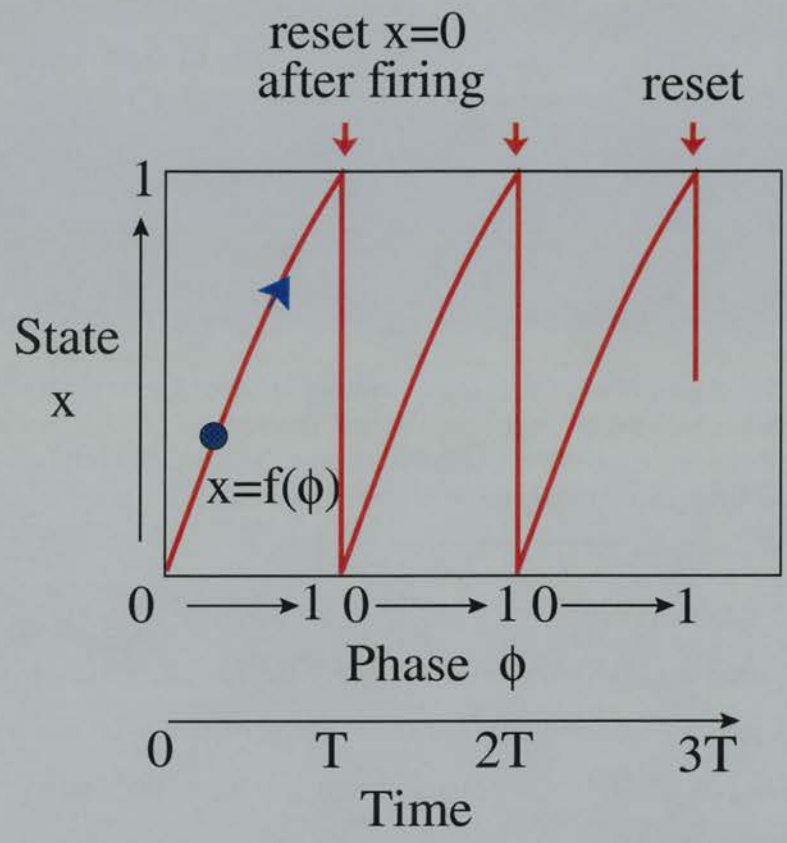

Figure 8.1: Dynamics of single Peskin oscillator for three cycles with no external firing input. Both the state x, and phase ϕ reset to 0 after firing. The time is plotted in the period T of the oscillator. (Adapted from (Mirollo & Strogatz, 1990).)

---

just fired and the phase of oscillator A has advanced from value $f(1-\phi)$ to $\epsilon + f(1-\phi)$. If the function $x = f(\phi)$ was linear instead of curved, the phase advance due to the firing of A would be exactly cancelled out by the firing of oscillator B. In this case the oscillators would not synchronize. Mirollo and Strogatz (1990) also proved that no synchrony would occur if the curve was convex. However because of the concave form of the curve, the phase difference between the two oscillators is consistently reduced or increased. Peskin proved that for small values of constants S_0 and γ, eventually the phase difference will either decrease to 0 or increase to 1 (Peskin, 1975). The result in both cases is that the two oscillators will synchronize their firing.

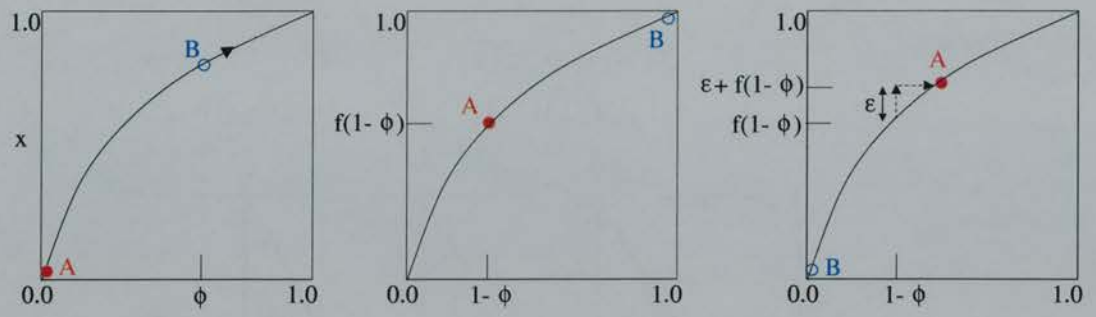

Figure 8.2: The sequence of events following the firing of 2 interacting oscillators. In (a) osclllator A has just fired. In (b) oscillator B is about to fire and A has advanced. The phase difference between the two oscillators is the same in both (a) and (b). In (c) oscillator B has fired and advanced the phase of oscillator A.

The model of Peskin was extended by Mirollo and Strogatz (1990). They proved that such a network would synchronize for all positive values of the constants S_0 and γ, and for any concave curve of the type shown in Figure 8.1 (1st derivative positive (increasing x with ϕ) and 2nd derivative negative (becoming less steep)).

8.4 The New Model of Network Synchronization

8.4.1 Revision 1. Spatial Position

In the theoretical approach of Peskin (1975) it was assumed that the network is fully coupled and any spatial effects were ignored. This was also true of the general model developed by Mirollo and Strogatz (1990). To introduce spatial effects into the system the network was implemented in 2-dimensions by locating cells at a random position in a 1x1 grid. Cells which are separated by less than the connectivity distance D are connected to each other with coupling

strength ϵ. Cells lying further apart are not connected ($\epsilon = 0$). If the connectivity distance D $\geq \sqrt{2}$, the network is fully connected (as $\sqrt{2}$ is the distance separating two cells lying at opposite corners in the grid e.g. (0,0) and (1,1)).

Varying the Coupling Strength.

The effect of varying the coupling strength on the time taken for the original fully connected network to synchronize was analysed. With a strong, coupling strength, the firing of one cell will bring a large number of other cells up to firing. These cells will then become locked in phase. The synchronization which occurs from a large, coupling strength results from the rapid propagation of high levels of activity rather than a subtle mechanism in which cell phases are gradually aligned.

8.4.2 Revision 2. Network Connectivity

The second revision to the original model was to determine the effect of partical connectivity on the ability of the network to synchronize. In the grid-model above, if D $< \sqrt{2}$ the network will only be partially connected. Figure 8.3 schematically shows the connectivity pattern for a partially coupled network (D=0.2).

The partial connectivity C of a network of N cells can be defined as $C = \frac{nConnections}{N*N}$. For a fully connected network of 100 cells, the maximum number of connections is approximately[3] N*N=10,000. If only 1000 connections are

[3]In the simulation runs, connections between the same cell were discounted so that the total number of possible connections is N*(N-1). For 100 cells this gives a maximum of 9900 connections.

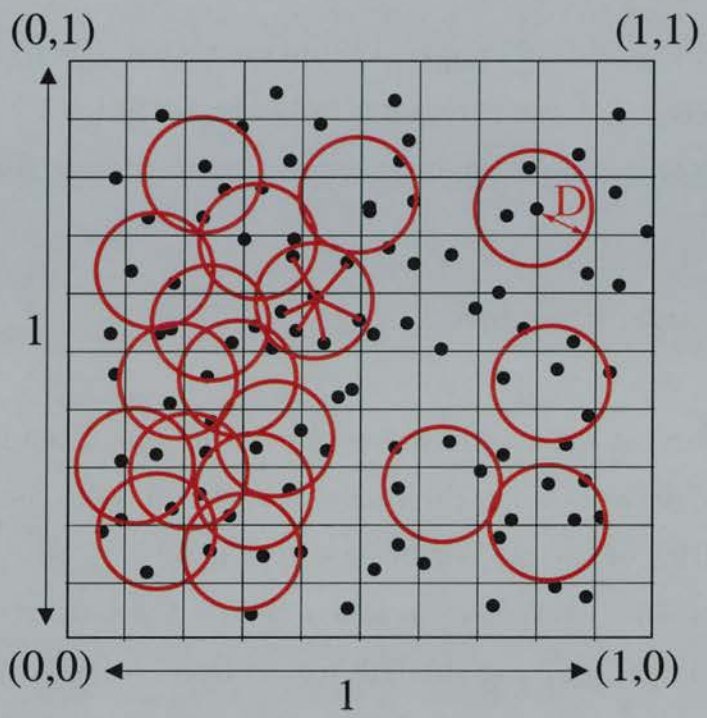

Figure 8.3: The schematic figure shows 100 oscillating cells distributed randomly on a 1x1 grid. Each cell is connected to all other cells within a distance D which simulates a circular dendritic field. The diagram represents a simulation run where cells with circles have just fired.

---

made then $C = 10\%$. Figure 8.4 shows how the partial connectivity of the network, C, varies with the connectivity distance, D. Decreasing the connectivity distance results in an approximately linear decrease in the partial connectivity of the network. The effect of decreasing the connectivity distance on the synchronization time of the network is given in the Results section.

8.4.3 Revision 3. The Chain-Reaction condition,

In the models of Peskin and Mirollo, if a cell was pushed above threshold it was not able to fire until the next time-step. If this condition is withdrawn then the firing of one cell, or group of cells, may promote other cells above

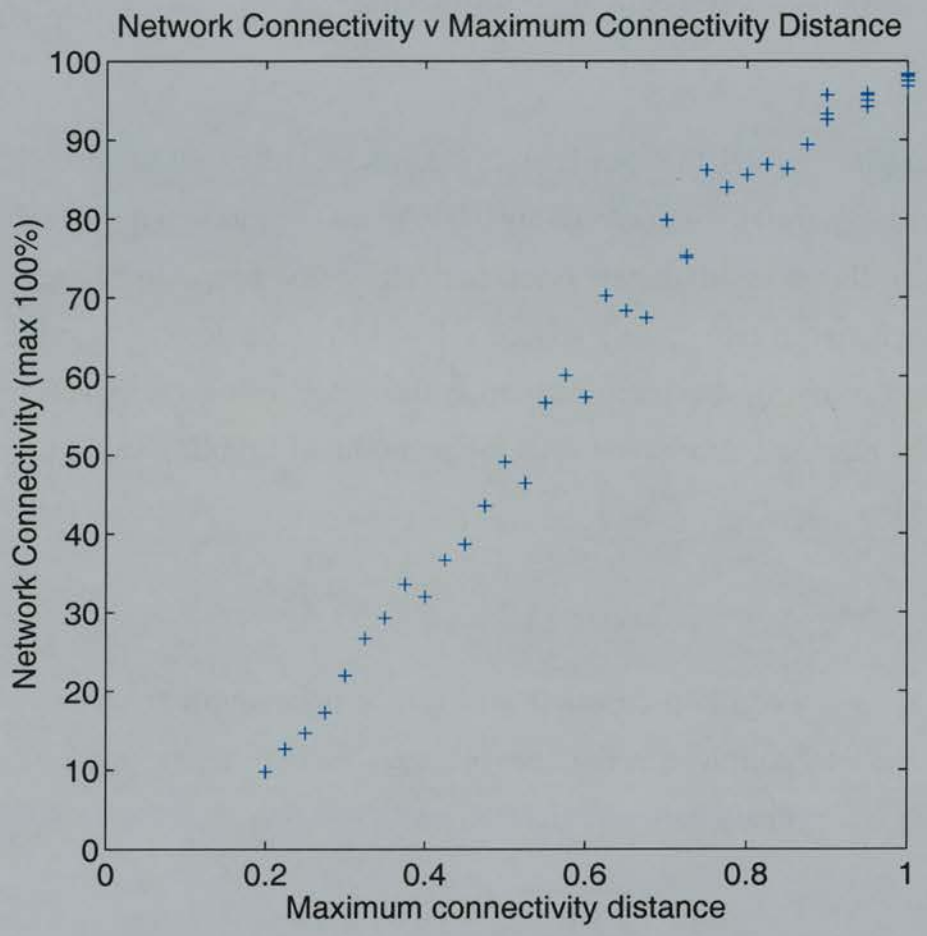

Figure 8.4: The figure plots the network connectivity against the maximum connectivity distance. If 2 cells are closer than this distance they are connected. Otherwise their coupling strength is set equal to 0 and the firing of one cell does not affect the phase of the other.

---

threshold causing them to fire. These cells in turn may cause more cells to fire. This can result in a "chain-reaction" of firing events. The chain-reaction will last until no more cells are induced to fire in the current timestep. A large, coupling strength may result in the immediate and synchronous firing of all cells in the network.

8.4.4 Revision 4. Weighted Coupling.

In the original model, the coupling strength, ϵ, was identical for all cells. However in a biological network, cells are likely to make more synapses with neighbouring cells than with distant ones. In this case, the coupling strength will be stronger between two closely spaced cells and weaker for cells further apart. Weighted coupling was implemented in the model using a simple formula to relate the distance, d, between cells to the modified coupling strength, ϵ'. This is given by:

$$\epsilon' = \frac{C}{w + d} \tag{8.2}$$

where w is a weighting constant and C is a normalisation constant which makes the total coupling in the network equal to that in a network where the coupling strength is ϵ between all cells, i.e.

$$C \times \sum_{i=1}^{nConnections} \epsilon'_i = nConnections \times \epsilon \tag{8.3}$$

This ensures that any difference in the behaviour of the network is due to the weighted coupling strength and not simply to a change in the overall activity levels caused by an increase or decrease in the total amount of coupling. The effect of the weighting constant w for values of 0.1 and 1 is shown in Figure 8.5. For strong coupling ($w = 0.1$) the coupling is 2.5 times greater for a cell 0.1 apart compared to one which is 0.4 apart. For weak coupling ($w = 1$) the strength of interaction of the closer cell is only 1.2 times greater than the more distant one. The effect of strong and weak coupling interactions on the synchronization time of the network was then simulated and the result is given in the Results section.

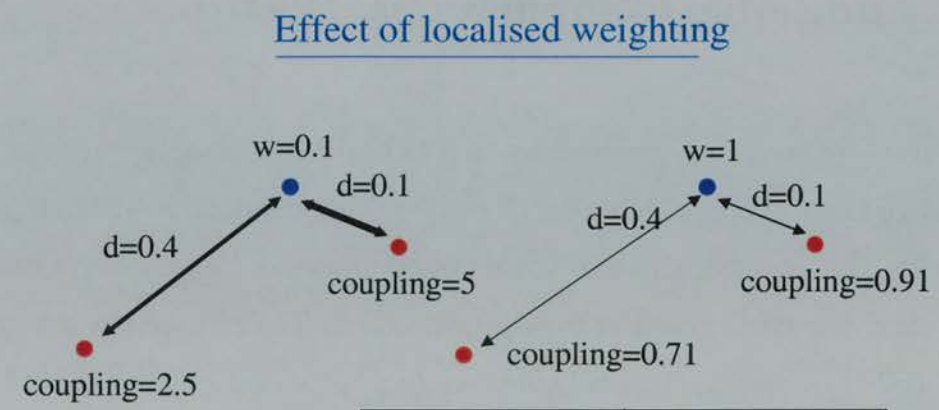

	Strong weighting w=0.1		Weak weighting w=1	
Distance d between cells	d=0.1	d=0.4	d=0.1	d=0.4
Actual coupling = $\frac{1}{w+d}$	5	2	0.91	0.71
Effective coupling ratio	2.5		1.27	

Figure 8.5: The effect of localised weighting on the coupling strength between 2 cells. A lower value of the weighting parameter w gives a higher effective coupling ratio.

8.4.5 Revision 5. Variation in Firing Frequency.

In the model of Mirollo and Strogatz (1990) the input signal S_0 was a constant for each cell in the network, i.e. the intrinsic firing frequency was identical for all cells. This parameter represented either an external input signal which is received by all the cells in the network, or a pacemaking constant which is intrinsic to the neuron and which is the same for all cells. This requirement is unrealistic as not all cells will receive the same input. In a system of intrinsic pacemaker cells there will be a spread of different oscillating frequencies. In these simulation runs each cell had a different value of S_0 which remained constant throughout the simulation.

8.5 Additional Computational Details

The cells were randomly positioned on a 1x1 grid (revision 1). All cells within a distance D were connected to each other with a connection strength = ϵ (revision 2). The edges of the grid were not connnected, i.e. cells near one edge were not connected to cells at the opposite edge. The connection strength between cells further apart than D was set to 0. The revised model is identical to the original model is implemented if $D > \sqrt{2}$. In the weighted coupling simulations (revision 4), the connection strength ϵ' (Equation 8.2) was used. The position of the cells in the network and the connections between cells did not change during the simulation. This allowed a connectivity matrix to be calculated at the beginning of the simulation to speed up the simulation.

At the start of the simulation (time t=0), each cell i, was given a random phase $0 < x_i < 1$. The phase was updated using the update rule from Peskin (1975): $dx_i = dt(S0 - \gamma x_i); x_i = x_i + dx_i$. The equations were solved using first-order Euler integration with a fixed timestep dt (default dt =0.001);

If the phase of cell i, $x_i > 1$ at time t, the cell fires and all cells to which it is connected have their phase increased by ϵ. The phase of the cell is reset to zero in the next time step. During this refractory period any additional inputs received by the cell do not affect the phase of the cell which starts the next timestep at zero. In the chainReaction condition (revision 3), the timestep is not advanced until there are no more cells remaining above threshold. If a cell fired during any given timestep, all other cells were checked to see if this brought their phase above the firing threshold. This loop was repeated to check if the latest round of firings had caused any more cells to fire. When no more cells remained above threshold, the phase of all the cells which had fired was reset to 0.

In simulations in which the firing frequency was not identical for all cells (revision 5), the intrinsic pacemaking signal S_0 for each cell was given a random value between S_0Min and S_0Max at the start of the simulation. This remained constant throughout the simulation run.

8.6 Results

8.6.1 Implementation of the original model (Fully Connected Network).

Figure 8.6 shows the activity of 10 cells as a network of 100 cells becomes synchronized (In all simulations default parameters: N=100, $\epsilon = 0.005, \gamma = 1, S_0 = 2$.) It can be seen that the pattern of cell activity is not smooth. This is due to the effect of coupling pulses produced by cell firing which create step-like discontinuities in the phase. Initially the size of these steps is small reflecting the firing of only 1 or a few neurons. The size of the jumps increases with time due to the appearance of larger clusters in the network. These emit a stronger coupling pulse as all the cells fire together. When the network is synchronized it behaves as a single oscillator and produces a large single spike at threshold. However most of the coupling strength of this large pulse is wasted as all cells in the network are already near threshold.[4] For this reason the firing period at synchronization is longer than at the beginning.

[4]For $\epsilon = 0.005$ most of the single pulse which increases the cell voltage by 0.5 has no effect on the firing frequency.

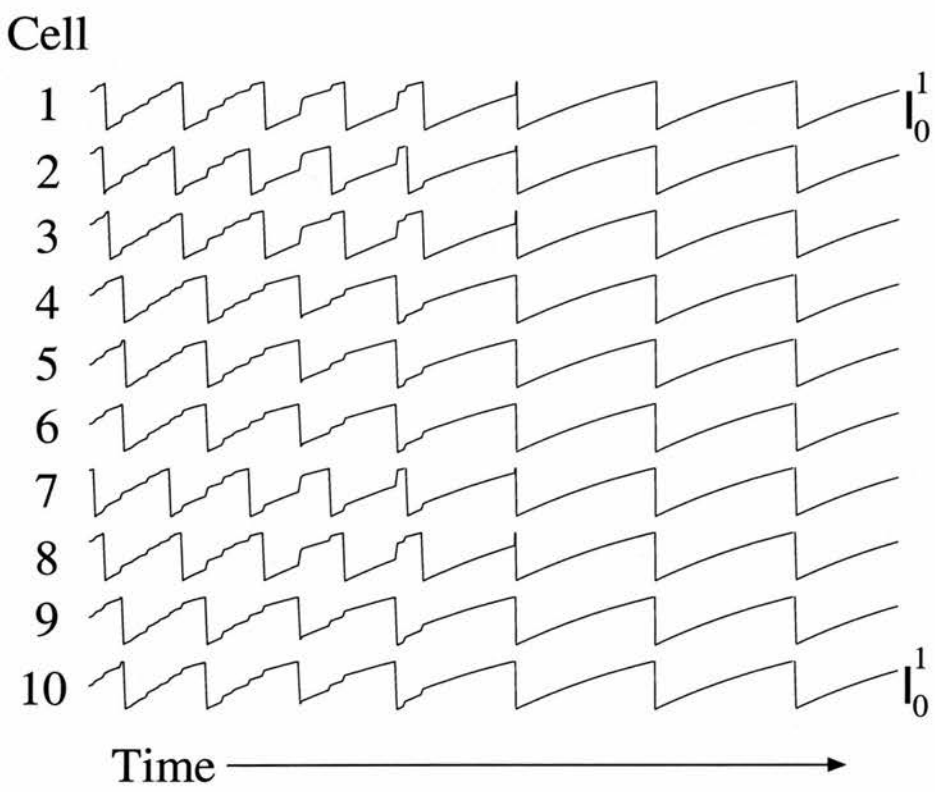

Figure 8.6: The sawtooth plot shows the activity of 10 cells in the network. Initially the cells are all out of phase. The activity of individual cells produces small jumps in the phase. As time progresses, the firing of larger groups of cells produces large steps in the phase of the 10 cells which eventually become coupled together.

8.6.2 Varying the Coupling Strength

Time to synchronization.

In the original coupling model, the strength of the coupling parameter has a strong effect on the time taken for the network to synchronize. Figure 8.7 shows the time taken for simulations with different values of the cell coupling parameter ϵ. It can be seen that the time taken for the network to synchronize rapidly increases with a corresponding decrease in the coupling strength.

Direct v. Indirect synchronization.

The coupling parameter also affects the mechanism by which synchronization is achieved. For a fully connected network of N=100 neurons where $\epsilon > 1/N$ the firing of one cell is likely to push at least one other cell above threshold. This occurs as the starting condition where the N cells are evenly distributed between 0 and 1, at least 1 cell is likely to have a potential $x > (1 - \epsilon)$. The firing of this cell in turn pushes another cell above threshold and so on. This results in a "domino-effect" where all cells in the network are then likely to fire within the next N timesteps. This form of "direct synchronization" depends on the propagation of high levels of activity, and not on a mechanism where firing phases are gradually coupled together. It is possible for a network with large coupling to synchronize in a time of less than 1 intrinsic period.

For values of $\epsilon < 1/N$ the synchronization of the network occurs through "indirect" phase coupling. As the value of ϵ decreases, the time taken to synchronize gradually increases. However further decreases in ϵ lead to a rapid increase in the time taken to synchronize (synchronization time $\rightarrow \infty$ as $\epsilon \rightarrow 0$). In this system there are two different mechanisms by which synchronization can occur, direct and indirect synchronization."Direct" synchronization occurs when a large amount of activity spreads rapidly throughout the network and causes all cells to fire immediately. Indirect synchronization occurs through the gradual coupling together of firing phases.

8.6.3 Revision 1 Results. Incorporating Spatial Position.

In the new implementation of the original coupling model, each cell has a location in a 1x1 grid (revision 1). This allows the development of the network

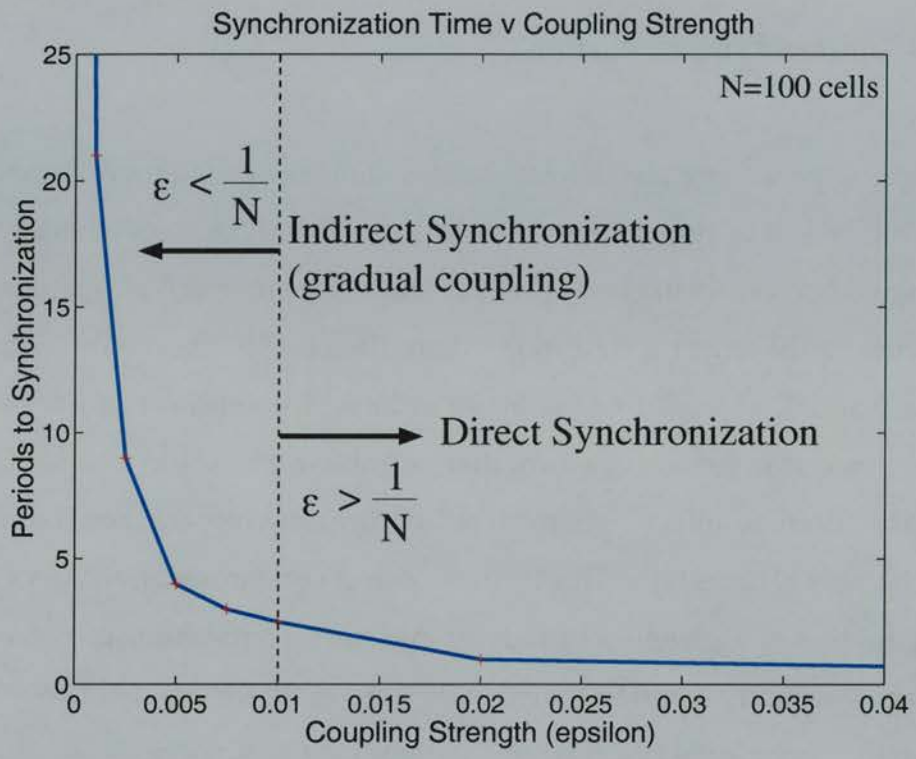

Figure 8.7: Synchronization in the original model. The plot shows the time taken for the network to synchronize for a range of values of the coupling-strength parameter ϵ.

---

to be plotted as a sequence of snapshots as shown in Figure 8.8. This shows the synchronization of the original network from a random starting state to synchronization. Each individual plot contains the phase of every cell in the network at that particular time. Snapshots are taken every 0.2 periods. Initially all the cells have a random phase and there is no synchronization. As the sequence develops, cells begin to fire with the same phase. As the network is fully connected there is no correlation between the firing of neighbouring cells. After around 3 periods most cells are firing with the same phase. At T=3.4 around 80 cells have just fired and only 20 cells are out of sync. At T=4 the number out of phase has been reduced to only 6. At the end of the sequence all cells are now closely in phase and the network is near full synchronization.

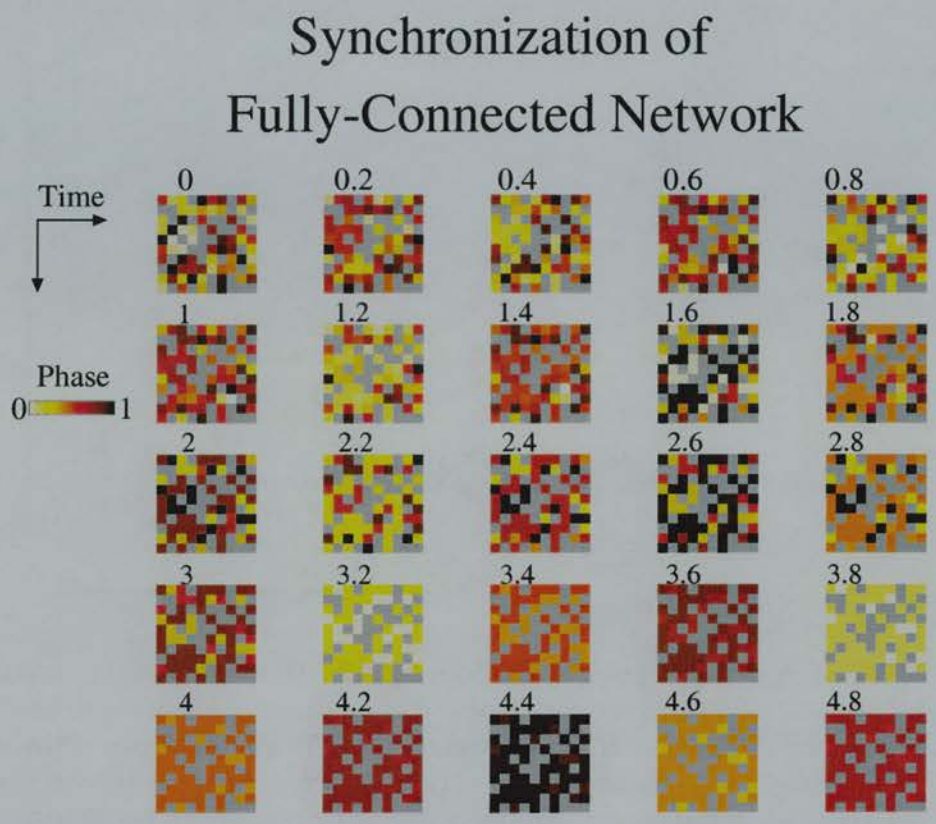

Figure 8.8: The plot shows the synchronization of the fully connected network over 5 periods. 100 cells are randomly arranged on a 1x1 grid ($\epsilon = 0.005$). The colour shows the phase of each cell: white=phase 0=just fired, black=phase 1=just about to fire. Initially the phase of each cell is random and there is no correlation between cells. As time progresses the network rapidly begins to synchronize. After only 5 periods almost all cells are synchronized and the cells oscillate in phase. N.B. There are no cells located in the grey grid points.

In Figure 8.9 the number of cells firing within a particular phase (between 0 and 1 in 10 divisions) is plotted as the network develops ($\epsilon = 0.0001$). Initially all cells fire with a random phase which is equally spread throughout 0 and 1. As time increases, cells begin to clump together in larger groups and fire with the same frequency. This is shown by the increasing number of cells firing within the same phase range. The strong coupling interactions of the cluster pull other oscillators into the group until eventually only one group dominates and the network is synchronized.

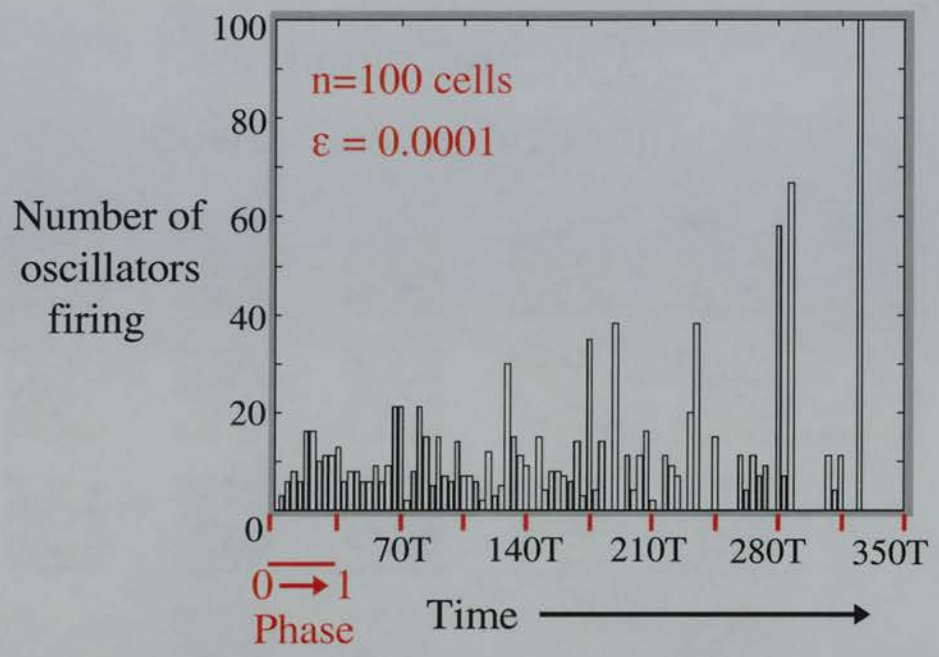

Figure 8.9: Synchronization of the Peskin network. The plot shows the number of oscillators firing as a function of time. Time is plotted in multiples of the natural period T of the oscillators. Each period is divided into 10 equal intervals, and the number of oscillators firing during each interval is plotted vertically. Initially the frequency is random and each bin has approximately the same number of oscillators. As the network develops phase-coupling begins to take place and clumps of oscillators with the same phase appear and begin to dominate. At the end of the simulation all 100 oscillators are synchronized. Parameters C=2, k=1, dt=ϵ=0.0001.

The same simulation run is shown in Figure 8.10 as a time/phase plot. The plot simulates a "strobe-effect" where the colour indicates the number of oscillators with a particular phase. As time increases darker bars appear indicating a growing number of oscillators firing at the same frequency. At the end of the simulation all cells fire in phase and oscillate as a single group.

8.6.4 Revision 2 Results. Effect of Partial Connectivity.

In the original coupling network all cells were fully connected to each other. It can be seen intuitively that the system will take longer to synchronize if the

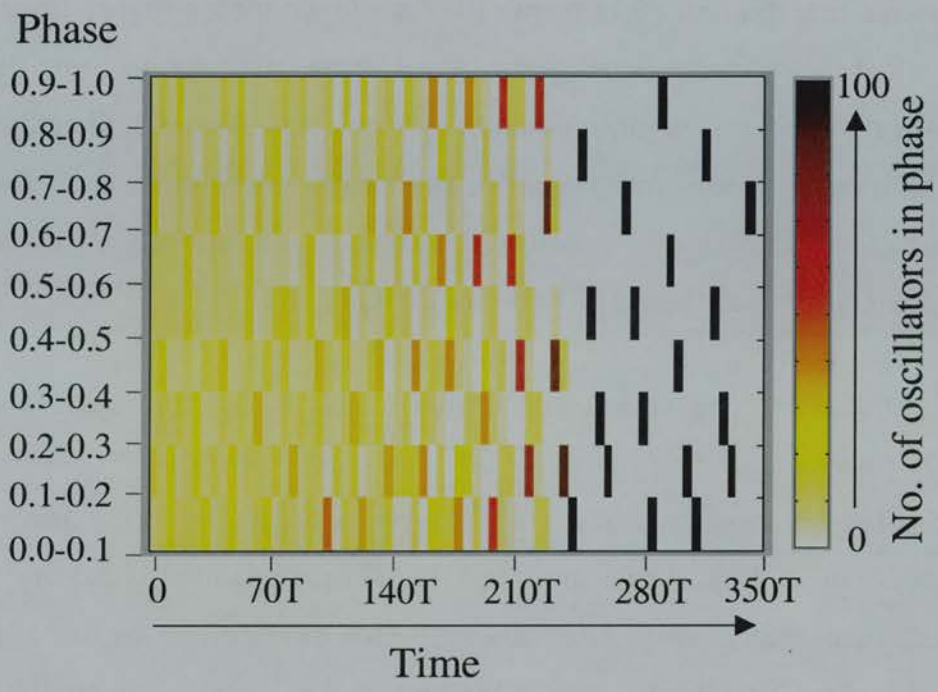

Figure 8.10: The graph plots the phase of the network against time. The colour indicates the number of oscillators at a given phase and time. This varies from white (0) to black (100). At the beginning of the simulation the oscillators have random phases and approximately 10 oscillators are in each of the 10 phase bins (uniform yellow). As development proceeds the appearance of stronger colours indicates an increase in the number of neurons oscillating with the phase. By the end of the simulation all neurons fire together (black bar) in a phase which continues to oscillate between 0 and 1.

---

system is partially-connected. This is because:

- There is less activity around to drive the system to synchrony as a result of fewer connections and

- As a result of partial connectivity, cells which are in synchrony in one cluster may be pushed out of phase by the activity of cells in another cluster. Developing clusters of cells will now compete until only one dominates. As the connectivity distance decreases, it is not guaranteed that such clusters will be able to synchronize.

The dashed line in Figure 8.11 shows the time taken for a network to synchronize against the connectivity distance. A reduction in the connectivity distance has a strong effect on the time taken to synchronize. As the connectivity distance is decreased, the time taken for the network to synchronize increases until synchrony is no longer possible. This occurs at a connectivity distance of around 0.6 (approximately 60% network connectivity).

The onset of synchronization takes approximately 3 days in the neuronal culture. For an initial firing period of 30s this would require 2*60*24*3 = 8640 periods. The above simulations were stopped after 2000 periods due to computational constraints. It was assumed that synchronization would not occur if it had not already done so after this time. However during the first few days of development, the connectivity of the neuronal culture is extremely low and most of the connections that will be seen in the mature network have yet to develop. During this time the amount of coupling activity driving the network to synchronization will be extremely limited. Therefore the time-scale for the onset of synchronization in the model is not in disagreement with the actual time required for synchronization in the neuronal cultures.[5]

8.6.5 Revision 3 Results. Effect of the Chain-Reaction condition.

As shown in Figure 8.11 the original network is unable to synchronize with local connections below a distance of about 0.6. However this can be overcome by introducing the chain-reaction scheme of firing. The lower curve in Figure 8.11 plots the time taken for full synchronization of the network using

[5]The discussion of TTX blockade of synchronization in the Conclusion section is also relevant to the time scale issue.

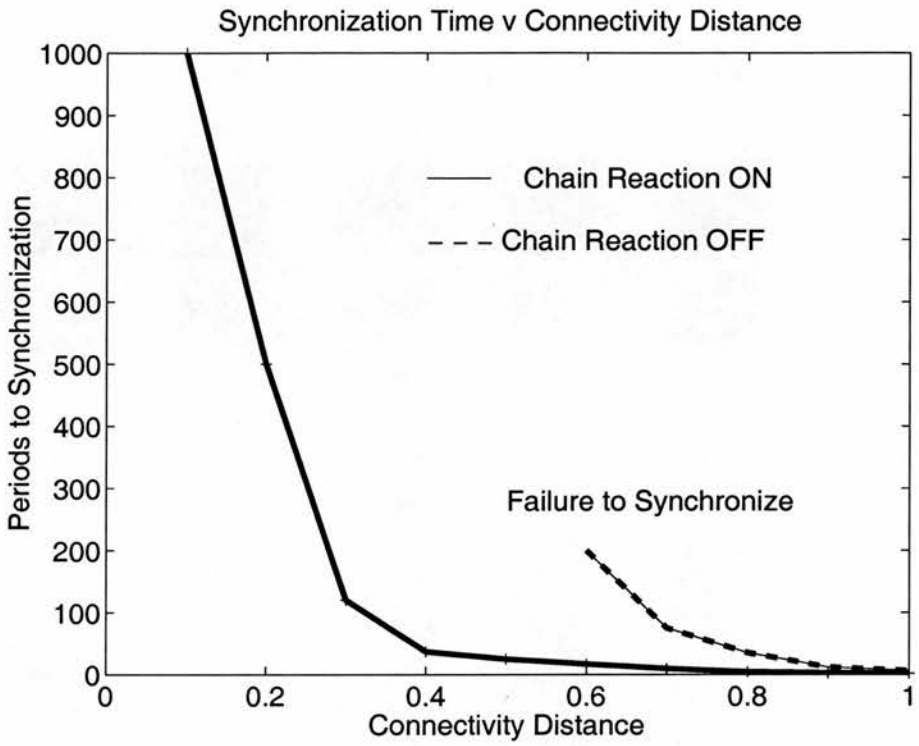

Figure 8.11: The plot shows the time taken for the network to synchronize for decreasing values of the connectivity distance. The original network fails to synchronize below a connectivity distance of around 0.6 (around 60% network connectivity). With the chain-reaction on, the network is able to synchronize down to a connectivity distance of 0.2 (around 10% connectivity).

---

the chain-reaction system. The chain-reaction network achieves synchronization with a connectivity distance as low as 0.2 (network connectivity around 10%). As a result of this, the chain reaction modification was included in all the simulations of localized weights and varied firing frequencies which follow.

Figure 8.12 shows the synchronization of a network with only 10% connectivity (D=0.2). Snapshots are taken every 20 periods. Initially all the cells have a random phase and there is no synchronization. In this network coupling interactions occur through neighbouring cells. As the sequence develops, local clusters of synchronized cells begin to form. This is evident at the bottom right of the network after 60 periods. After 200 periods, synchronized clusters are

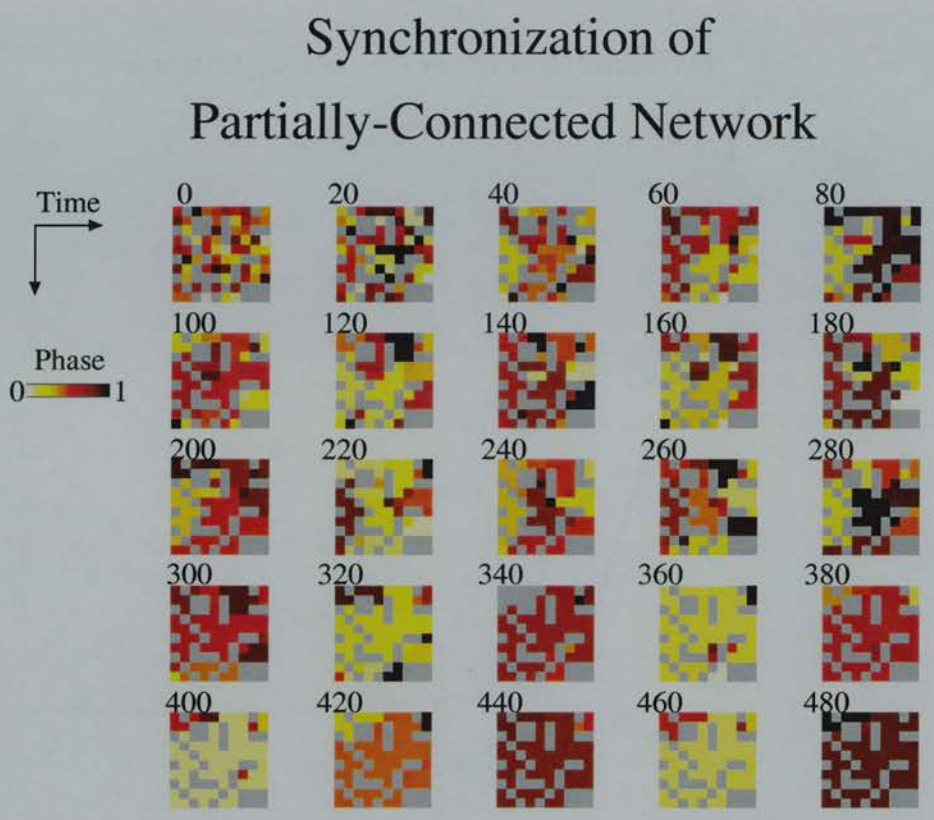

Figure 8.12: The plot shows the synchronization of the partially connected network over 500 periods. Connectivity=10%, D=0.2, N=100, $\epsilon = 0.005$. Initially the phase of each cell is random and there is no correlation between cells. As time progresses, local coupling interactions lead to the formation of clusters. The network synchronizes slowly due to the competition between clusters and the lack of a single coupling signal. Four clusters are evident after 200 periods however these have merged into one main cluster by around 320. After 480 periods the firing of the network is almost fully synchronized.

---

beginning to develop at each corner of the network. After 320 periods, a main cluster is forming in the centre of the network. Finally after 480 periods almost all cells in the network are now oscillating in phase.

8.6.6 Revision 4 Results. Effect of Weighted Coupling.

Figure 8.13 shows the the effect of strong weighting (w=0.1), weak weighting (w=1) and random weighting, on the time taken for the network to synchronize. In all three cases the overall amount of coupling between cells is the same. The strong weighting should enable neighbouring cells to synchronize more quickly due to their higher coupling strength. However this will also reduce coupling interactions at greater distances. These two effects appear to cancel each other out. The best fit curve through the strong weighting data is almost identical to that of the weak coupling model (which is closely matched to the original model). There is an increase in synchronization time for random weighting at lower values of the network connectivity. However this does not prevent network synchronization from occurring. These results indicate that the amount of coupling in the network is a more important factor in determining when synchronization occurs than the precise form of the coupling interactions between cells.

8.6.7 Revision 5 Results. Effect of Varying the Firing Frequency.

Variations in the rate of firing of the cells will disturb the overall synchronization. In a network where all cells are initially in phase, different pacemaking frequencies will spread out the times at which cells fire. In this situation the network will only fire in full synchrony if the coupling interactions between the cells are large enough for a chain-reaction to take place. This will occur when the firing of the fastest cells brings on the onset of firing of slower cells. However this will not take place if the coupling strength, ϵ, is not large enough.

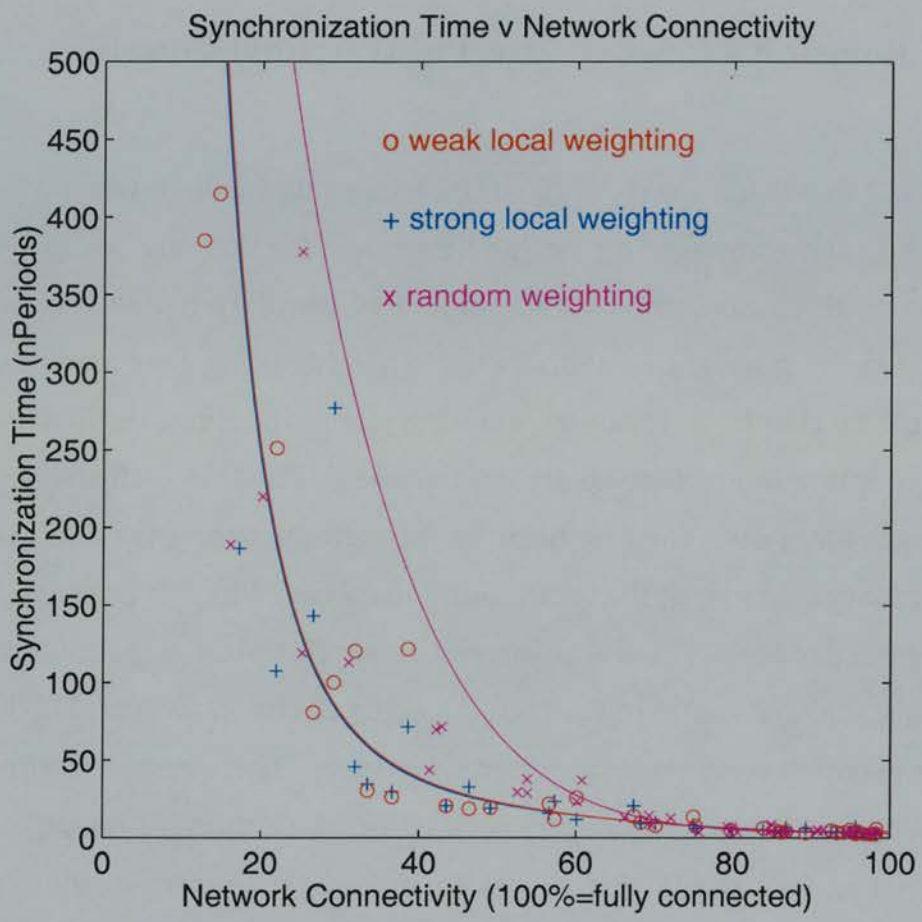

Figure 8.13: The plot shows the time taken for the network to synchronize for strong weighting (k=0.1) or weak weighting (k=1). Connections between cells in the network are weighted inversely with distance so that local connections are up to 3-times stronger than more distant ones. The best fit curves are almost identical for the two conditions suggesting that non-equal coupling has little effect on the overall synchronization time.

Figure 8.14 shows the membrane potential of cells in a simulation where the intrinsic pacemaking signal for the cell, S_0, was randomized. Each cell was given a random value of S_0 between 1 and 2 which remained a constant for the duration of the simulation. This meant that the faster cells fired at twice the frequency of the slower cells.

In this simulation run, cells which have similar firing frequencies are able to couple together. A larger value of the coupling strength enables more cells

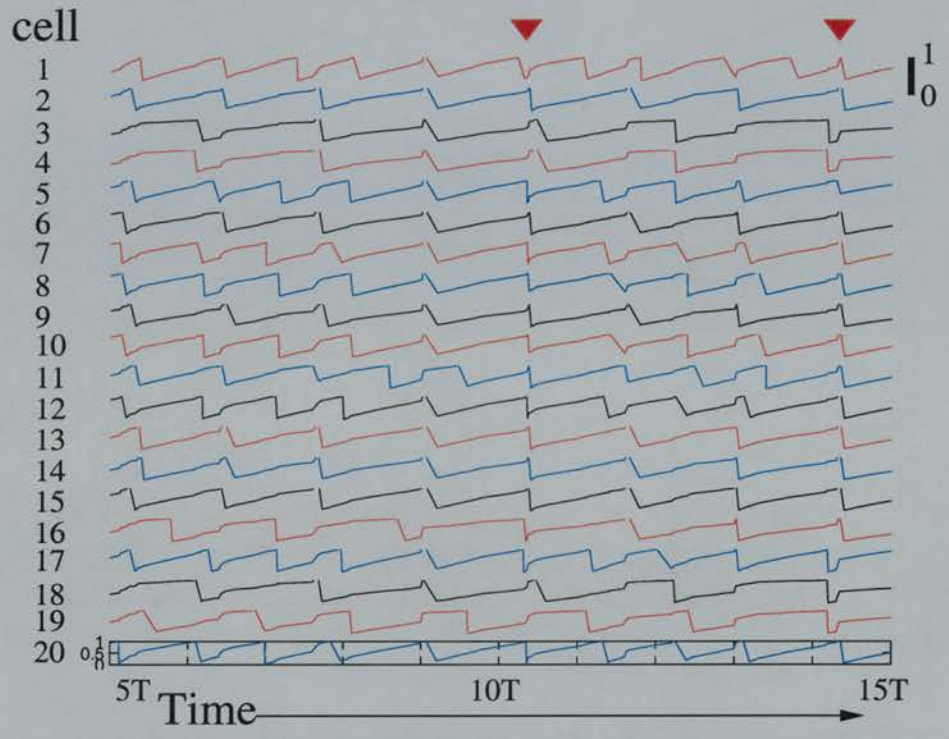

Figure 8.14: The plot shows the membrane potential of cells during several oscillations. In this network not every cell fires at each burst. Fast firing cells, e.g cell 1 are regularly out of phase with slow firing cells, e.g cell 2. Arrows show states in which the network is nearly synchronized. Parameters ϵ=0.005, γ=1.

---

firing at a lower frequency to be brought up to the firing threshold by faster firing cells. These cells will remain synchronized. If this is not the case, the cells will fire out of phase for most of the time. Occasionally the network almost synchronizes (this is shown by the arrows). However fast firing cells (e.g. cells 1 and 17) are not able to phase lock with slower firing cells (e.g. cells 2 and 18) and the network is unable to fully synchronize. In this simulation run, the maximum number of cells firing at any one time was 94/100. However if the difference in firing rates is increased, or the strength of the coupling interaction is decreased, the synchronization of the network rapidly degrades.

Figure 8.15 shows the results from a simulation in which the firing frequencies were varied by a factor of four ($S_0Min = 1, S_0Max = 4$). The plot shows the

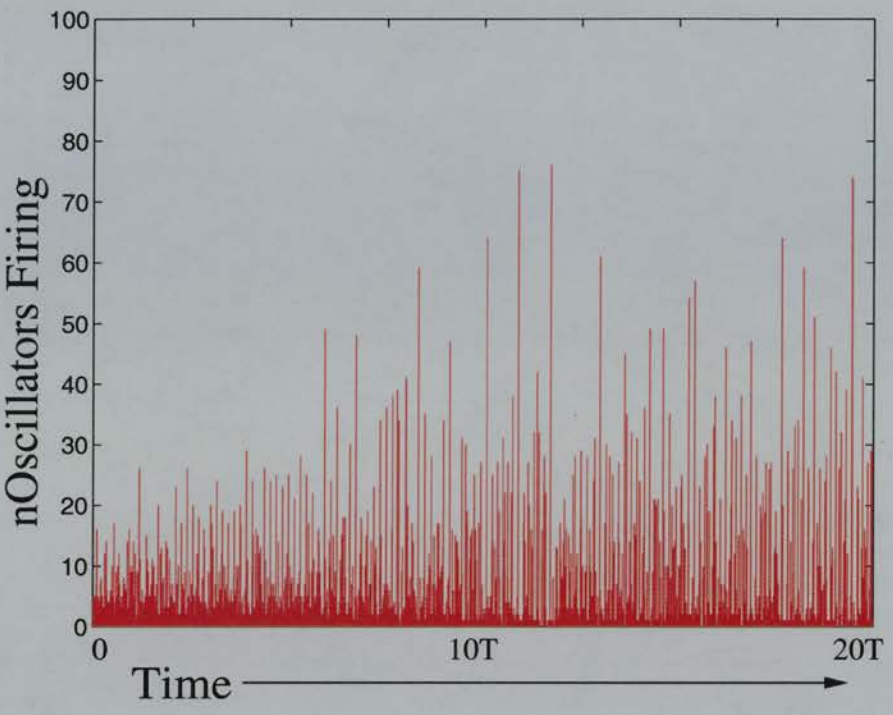

Figure 8.15: The plot shows the firing times of cells in a network which have varying pacemaking abilities. The network is unable to reach full synchronization and the distribution of firing times is extremely chaotic. Parameters: ϵ=0.005, γ=1.

number of cells which fire at a given time. In this network the firing pattern is unstable and does not reach full synchronization (The maximum number of cells that fired in synchrony within 100 periods was 84/100). The synchronization that takes place in this network occurs directly through firing of cells as they respond to a large amount of local activity rather than indirect coupling. When the coupling strength ϵ was decreased from 0.005 to 0.001, only a maximum of 5/100 cells fired in synchrony over the same period.

In the above simulations, each cell has been able to fire without requiring external bursting activity of other cells. Such cells could either be intrinsic pacemakers, or receive enough spontaneous background activity to overcome the decay in potential. In contrast Figure 8.16 shows the firing time of cells in a simulation where most cells were not able to reach firing threshold. In this

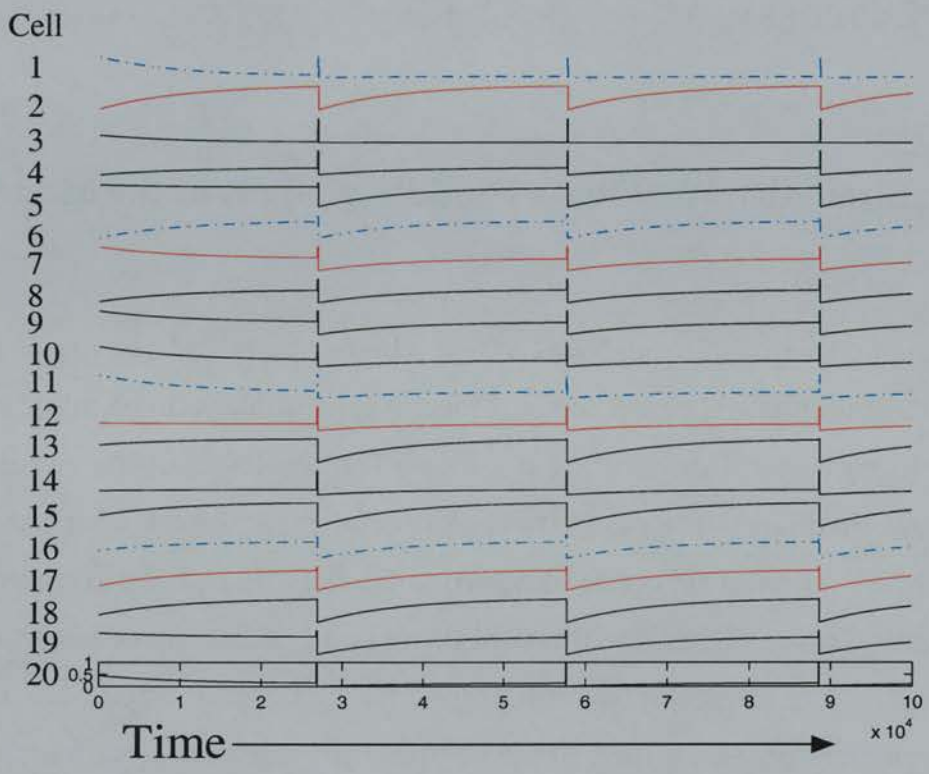

Figure 8.16: The plot shows how the membrane potential of 20 cells with varying pacemaking abilities varies with time. Some of the cells are not-intrinsic oscillators and their potential is flat between firings. These cells only fire following activity from the actively oscillating cells. Parameters: $0 < S_0 < 0.11, \epsilon = 0.1, \gamma = 0.1$.

---

simulation the firing frequency S_0 was given a random value between 0 and 0.11, and the decay rate $\gamma = 0.1$. Cells in which $S_0 < \gamma$ are unable to fire of their own accord. However in a small population of cells, $S_0 > \gamma$, and these cells are able to reach a firing threshold. Most of the cells in this network are silent between firings (e.g. cells 1,3,4,10,11,12,14,20) and simply respond to the activity that is initiated by the firing of the oscillating cells. This system is only able to achieve full synchronization for values of the coupling parameter $\epsilon > 1/N$. In this type of simulation the firing of one cells can cause a "domino effect" which leads directly to the synchronization of the network. The gradual and indirect coupling effect does not occur.

8.7 Discussion

8.7.1 Strengths, Weaknesses and Predictions of the Models

The aim of the current model was to test whether a revised version of the indirect, coupling model could account for the synchronization of cell firing observed in cultures of developing neurons. The results from the simulations show that there are (at least) two very different mechanisms which can lead to synchronization of this type of network - direct and indirect. Indirect synchronization occurs when the phase of firing of an oscillating cell is gradually coupled together to its neighbouring cells. In a locally connected network this creates clusters of cells which compete until only one cluster dominates. At this point the network is fully synchronized. This was the mechanism put forward to account for the synchronized firing of cardiac pacemaker cells (Peskin, 1975) and general synchronizing systems such as flashing fireflies (Mirollo & Strogatz, 1990) (although both these systems considered fully-connected networks).

Direct synchronization occurs when the firing of one or a few cells creates a large build up of activity which immediately induces all other cells in the network to fire. In this system the firing of one cell has an immediate "domino effect" on the firing of all other cells. It is likely that this is mechanism causes synchronization in developing neuronal cultures. It has been observed that cells in which electrical activity has been blocked with TTX during development are able to synchronize almost immediately following washout (Murphy et al., 1992). This suggests that a slow, coupling between electrically active cells is not required for full synchronization. This observation alone does not rule

out the gradual coupling model. It is known that the coupling strength of individual synapses increases following blockade of activity (Turrigiano, Leslie, Desai, Rutherford, & Nelson, 1998). The activity blockade increases the sensitivity of the postsynaptic cell to glutamate. The rapid synchronization that occurs following TTX blockade may simply result from the "domino effect" caused by the artificial increase in the coupling strength between cells.

However, after revising the model of Mirollo and Strogatz (1990) I discovered that the cultured neurons simulated in the current model do not display any signs of an intrinsic pacemaking potential (Robinson et al., 1993). Although the cells in the culture fire at a constant frequency, the membrane potential of each cell remains at rest from shortly after the cell fires, until shortly before the onset of synchronized firing. At this point the membrane potential rapidly rises to threshold and the cell fires. The simulated neurons in the current model also have a constant firing frequency, but this is generated by a pacemaking signal. This does not have to be intrinsic to the cell as it could be generated by an external mechanism, e.g. afferent synaptic input. However this would also cause an observable increase in the membrane potential which is not seen in the experiments. Clearly some mechanism is responsible for producing the regular and long refractory period that is seen (up to 20s). It has been suggested that the long quiescent times between bursts may represent the time required for replenishing neurotransmitter (Kamioka, Maeda, Jimbo, Robinson, & Kawana, 1996). There are very few synaptic vesicles present in synaptic terminals at this developmental stage (Ichikawa, Muramoto, Kobayashi, Kawahara, & Kuroda, 1993) and these may be substantially depleted following firing. This mechanism could act as an effective pacemaker for the cell and the membrane potential of the cell would remain at base levels until the neurotransmitter was sufficiently replenished.

The indirect synchronization which occurs with the coupling mechanism does

not provide an appropriate explanation of how synchronization occurs in this particular system of cells in culture. However the revised coupling model presented here is still valid for the biological systems to which the model was first applied. As well as systems such as flashing fireflies, and chirping crickets, this includes groups of cells in the brain whose firing patterns may become entrained through coupled firing. The revised model simulates the spatial position of cells (revision 1) which was not included in the original model. Synchronization can also occur in this type of network with partial connectivity (revision 2). In the original model, the network can synchronize down to a partial connectivity of approximately 60%. The inclusion of chain-reaction firing in the model (revision 3) greatly assisted the onset of synchronization in the network. With the chain-reaction mechanism on, the network was able to fully synchronize with a partial connectivity as low as 10%. Network synchronization was also largely unaffected by varying the strengths of connections so that neighbouring cells were more coupled than distant ones (revision 4). However introducing varied firing rates (revision 5) led to an immediate reduction in the ability of the network to synchronize. Under these conditions, the majority of cells are only able to synchronize if the coupling strength is large enough. The exact number of cells which fire in any given burst varies widely and depends on the firing history of the cell. However biological observations from neurons in developing cultures aswell as from developing cells in the retina suggest that these network may never fully synchronize. In the retina only 60% of active cells may participate in synchronous activity at any given time[6]. In developing neuronal cultures some cells either remain inactive, or actively fire but do not fire in synchrony (Voigt et al., 1997). The simulation results suggest that this observed lack of firing may simply be a consequence of the connectivity of the network, rather than as a result of external effects or

[6]Dr. Stephen Eglen, personal communication.

improper development.

Although the coupling mechanism which gradually aligns the phases of cells (indirect synchronization) requires an intrinsic pacemaking signal, the direct synchronization mechanism does not. Direct synchronization is achieved through the rapid spread of activity once a critical number of cells have reached firing threshold. It is likely that the time delay that is observed for the initial synchronization to occur is due to the lack of connections in an immature network. As these connections develop, cells throughout the network begin to fire at the same time. It is predicted that any inhibitor of neurite outgrowth, or synaptic devlopment would significantly delay the onset of synchronized firing. Similarly it is predicted that the increasing firing frequency and greater speed of activity propagation that is observed in the more mature network is simply due to an increased network connectivity. The current model does not specifically address these issues, however it provides the basis on which a more detailed model of this phenomenon could be developed.

Chapter 9

Conclusion

The aim of this thesis was to develop computational models which would lead to an increased understanding of the mechanisms underlying the development of biological neuronal networks. At present there is little theoretical understanding of how overall cell behaviour arises from subcellular interactions. Each of the new models simulate three different but related stages of neuronal development:

- How neurons find their target cells.
- How neurons achieve their characteristic pattern of connections.
- How functioning neuronal networks are formed.

The aim in modelling these systems has been to highlight possible factors that might play a key role in controlling the response of the cell. The models of growth cone microtubule and filopodia dynamics simulate the mechanisms which give the growth cone its navigational properties and enable it to find the

correct target area. The model of dendritic branching shows how the characteristic pattern of dendritic connections can arise primarily through an intrinsic signalling mechanism. Finally the model of synchronized firing amongst developing neurons in culture looks at one aspect of how functioning neuronal networks are formed.

All of these models were motivated by the unifying theme of "Computational Models of Developing Neural Systems". Individually, each model simulates a particular aspect of neuronal development and each model can be treated independently. However it is also intended that they can be viewed together to give a broader understanding of neuronal development than would be possible using a single model alone. The remainder of this chapter discusses the main findings of each of the models presented in the thesis and suggests possible future work that could be based on these findings.

9.1 Growth cone microtubule dynamics

The model of microtubule dynamics and growth cone turning suggests that the short term nature of dynamic instability may affect the long term elongation and turning behaviour of the developing axon. Growing microtubules at the front of the bundle shield rearward microtubules from the compressive force of the rearward-flowing F-actin network. As a result of the "slipstreaming effect" the rescue and catastrophe frequencies of these microtubules will be respectively increased/decreased. This will reduce the energy required for elongation resulting in efficient outgrowth. The higher turnaround from shrinkage to growth of microtubules in the neurite shaft ensures that the array of microtubules will be able to respond quickly and in large numbers to any

change in the F-actin flow caused by filopodial contact or receptor activation. It was found that microtubules could only respond in this way if they were able to grow out from the neurite shaft into the direction of least resistance (the target segment in the simulation). It is possible that this is the most energetically favourable direction for the addition of new tubulin dimers at the microtubule tip. Alternatively the reduced F-actin flow may allow microtubules in the target segment to be stabilized. These pioneer microtubules may then define the future direction of growth by providing a scaffold which rearward microtubules are able to grow along.

There are a number of extensions to the model which might lead to interesting results. At present it is not clear how the microtubule bundle is affected when more than one direction is energetically favourable, e.g. when several filopodia interact with target cells or there is a strong gradient of chemoattractant across the growth cone. The current model may help to determine when the microtubule bundle grows forward as a single unit and when it splits into two separate paths.

The model does not explicitly simulate the effect of the tubulin concentration. Microtubule behaviour would be affected by local differences in the tubulin concentration in the growth cone although these have not been observed (Letourneau et al., 1987). If tubulin uptake into microtubules did vary across the growth cone, the frequency of catastrophe might be increased at the growth cone periphery, or decreased within the neurite shaft, due to the lack of, or presence of other microtubules. There may also be competition between microtubules for tubulin dimers although this is not taken into account in the current model.

Finally the overall position of the growth cone does not change during the encounter with the target. One of the reasons for this is due to the difficulty of

simulating a continously changing membrane surface. There is also a lack of quantitative data regarding growth cone collapse and new growth cone formation at the leading filopodia. At present the mechanisms which enable the growth cone to switch between a stable and collapsed state are not fully known. It is possible that a modified form of the current model could be used to simulate the dynamic advance of the growth cone.

9.2 Growth cone filopodia dynamics

The model of filopodia dynamics showed how localised changes in the calcium concentration at the leading edge of the growth cone could alter the stability of F-actin/substrate coupling. Changes in the membrane surface may have a positive feedback effect on local calcium concentration reinforcing any fluctuation (Hentschel, 1994). Filopodia would extend whilst this fluctuation remained stable and shrinkage would occur following decoupling between the F-actin network and substrate. It is proposed that calcium could act as an activator with a chemical such as cAMP playing the role of an inhibitor in a Turing-like reaction-diffusion system. A similar mechanism may be responsible for the generation and outgrowth of membrane protrusions in Acetabularia. Such a system could also account for the increase in the number of filopodia, and the narrowing of filopodia spacing following localized electrical stimulation. In this situation the model produces a narrowing in the characteristic width of the reaction-diffusion patterns. This would provide the growth cone with an intrinsic method for generating filopodia in the absence of external input from the extracellular matrix.

The current model does not directly take into account interactions between the growth cone and the extracellular matrix which will have significant effects

on filopodia behaviour. These include filopodial contact of other cells and receptor activation by chemicals such as adhesion factors, chemoattractants or neurotransmitters. These will affect a wide range of second messengers which alter the amount of calcium or cAMP which is locally available. However in both the intrinsic and external cases it seems that the end effect - localised coupling of the F-actin network to the substrate - is the same.

Rapid changes in the shape of the local environment caused by filopodia activity and cytoplasmic streaming might ensure that the hypothesized Turing reaction-diffusion patterns underlying filopodial outgrowth do not remain fixed unless they are otherwise stabilized. However, even with these disrupting influences, it is possible that the Turing system described here remains too unresponsive to rapid changes in external input. Any mechanism (of which the Turing system is one) which creates transient and localised changes to the binding of the F-actin network could result in characteristic filopodia activity. This model attempts to move away from the situation where the dynamics of filopodia are attributable to random, unpredictable events towards a predictive understanding of the underlying cellular mechanisms involved.

9.3 Causes of dendritic branching

The model of dendritic branching aims to combine a descriptive model of the dendritic geometry with a biologically plausible cellular mechanism. Models of dendritic branching which do not attempt to define the causes of branching and outgrowth are able to accurately simulate the observed dendritic arbors using a number of appropriately chosen random parameters. However there may be a fundamental limit to the value of the results that can be achieved

with this approach. The current model simulates the effect of the microtubule-associated protein MAP2 on the long term growth and spacing characteristics of the microtubule array. This in turn defines the rate of dendritic outgrowth and branching. The model is able to account for a wide variety of dendritic shapes primarily through the phosphorylation status of MAP2. This acts as a 2-way switch to control the rate of outgrowth and branching. The particular MAP2 setting is in turn controlled through the action of calcium-dependent CaMKII/calmodulin phosphorylation/dephosphorylation of the microtubule-MAP2 complex.

It is clear that a large number of other chemical signals will be involved in this pathway and that this will not be the only way in which the characteristic dendritic arbor can be created. However this mechanism unifies the role of intrinsic and external influences on cell shape. During the early period of dendritic growth it is likely that intrinsic signals are largely reponsible for the characteristic shape of a particular neuron. As contact is made with the branches of other cells, synaptic interactions may guide the subsequent branching. In some cells it seems that dendritic elongation is promoted, and branching is inhibited until a specific target is contacted, e.g. the long apical dendrites of pyramidal neurons which branch extensively on arrival in layer I of the cerebral cortex. In others such as the growth of the pyramidal basal dendrites in layer IV of the cortex it seems that intrinsic factors play an important role in defining the cell shape. The model is consistent with the experimental observations that Purkinje cells elongate in the absence of electrical activity (and reduced intracellular calcium). In contrast branching is observed following the arrival of synaptic activity and a general increase in the interconnectivity of the network (Schilling et al., 1991).

There are a large number of possible modifications that could be made to the model.

- The model could be extended by dynamically varying the production of MAP2 at the soma to be dependent on reactions which occur at the tip of the dendrites. This would allow branching to be inhibited until external contact has been made. This would allow the possible role of feedback to be tested. Different branching structures would be generated depending on the dynamics of the production of MAP2. One possible experiment would be to analyze the structure of dendrites under tests in which the concentration of MAP2 was varied. The question of whether MAP2 production is increased following external contact with other cells could be answered by plating cells at different densities and measuring the ratio of MAP2 with time. If the rise in MAP2 occurred much later in sparsely plated cultures it is likely that the increase is a response to external contact. However if the MAP2 rise is similar in differentially plated cultures, it would suggest that the rise in MAP2 is purely an intrinsic process.

- At present the model does not directly simulate the physical amount of material required for dendritic outgrowth. This may be a limiting factor in halting elongation or reducing the branching probability. Including this factor may lead to competition between growing dendrites which is not seen in the model.

- The model does not include active-transport of MAP2. However it is unlikely that this plays a significant role in development when distances between distal dendritic tips and the soma are still relatively short ($< 200\mu m$). In contrast to slow axon transport it is also not clear how active dendritic transport occurs along the bi-directional microtubule array that is found in dendrites. One of the weaknesses of the model is that the concentration of MAP2 decreases away from the soma in a predictable fashion. The model is not able to capture the increase in MAP2 which is seen at branching points. It is possible that by simulating the active

transport of MAP2, the simulated distribution of MAP2 would match that seen in biological dendrites more closely. This may have a significant effect on the branching patterns that are seen.

- The model does not simulate dendritic retraction or removal of branches. Very low or high calcium concentrations are prohibitive to dendritic outgrowth and the outgrowth function could be modified to take account of such retraction. Simulating both outgrowth and shrinkage may lead to branching patterns which are not possible using simple one-way model of outgrowth.

All of these considerations could be included in variations of the basic model.

Finally it appeared that the general characteristics of the model could be predicted by a theoretical consideration of the reaction equations. The agreement between the actual simulation and theoretical analysis confirms that the results are not the by-product of a specific implementation of the computer code. It also suggests that modelling each compartment may not be necessary. At present only one primary dendrite is simulated in each run as the multi-compartmental approach is computationally intensive. It is likely that modelling each dendritic branch with just one compartment would have little consequence on the actual dendritic topologies produced. This could result in a significant speed up of the program and reduction of the memory required. This would then allow networks of developing cells to be simulated. At present most simulations of networks of cells use connectivity patterns based on average biological statistics rather than allowing the individual neurons to interact by growing connections. The current model may make this type of developmental connection formation more feasible.

9.4 Synchronization of activity in neuronal networks

The aim of the new simulations was to see if a revised version of a general synchronizing model was able to account for the synchronized behaviour observed in developing neuronal cultures. In this model, the active coupling synchronization requires a pacemaking potential either through an intrinsic ability of the cell, or through a constant background source of activity. As a pacemaking potential is not observed amongst developing neurons in culture, the simulation results suggest that the type of synchronization seen in these cultures is purely passive and results from the rapid spread of a large amount of electrical activity through the system. Therefore on re-evaluation, the active coupling model is not an appropriate mechanism to apply to the synchronization of developing neurons in culture.

However the results from the new simulations show that this type of network is able to synchronize at low values of network connectivity. This extends the results of previous models which have used global connectivity as the basis of their synchronization mechanism, e.g. (Mirollo & Strogatz, 1990; Tsodyks, Mitkovm, & Sompolinsky, 1993; Abbott & Vanvreeswijk, 1993; Hansel & Meunier, 1995). In particular it was found that introducing the chain-reaction method allowed full synchronization to occur at around 10% connectivity levels. At lower levels of connectivity, full synchronization cannot occur due to the presence of isolated cells which do not make any connections.

The new simulations also showed that in this type of system the exact form of coupling interaction is not a fundamental factor which controls the ability of the network to synchronize. Synchronization was possible using either equal

coupling, weighted local coupling, or randomized coupling. In the latter case synchronization was degraded at low levels of connectivity. In each of these simulations the total amount of activity in the system was equal. It appears that the total amount of activity in the system has a stronger bearing on the speed of the network to synchronize than the exact form of the coupling interactions.

The inclusion of different cell firing frequencies in the network was found to have a more disruptive influence. If the range of different firing frequencies is small, the firing of the faster cells is able to bring the slower cells up above threshold. However for larger differences in the firing frequencies, the network exhibits chaotic behaviour. Such a network can only achieve synchronized activity through passive synchronization.

There are a number of extensions to the model which could be based on the current simulations. Firstly any model should incorporate a mechanism which allows a periodic build up of activity but which does not result in an effective pacemaking potential. The exact cause of the long refractory period is unknown however it is likely that a localized depletion of the excitatory neurotransmitter glutamate is involved. This has recently been shown to recover with a time constant of about 10 seconds (Stevens & Tsujimoto, 1995). This could be simulated by including a fixed amount of glutamate in the network. As firing becomes synchronized, all local sources will become depleted at the same time. This could result in the observed periodic firing and may also help to drive the network to synchronization. However it is not clear how the firing frequency of the network could increase from approximately once a minute (0.01Hz), to once every 2 seconds (0.5Hz) if glutamate recovery requires at least 10 seconds.

The current model does not examine the timing of the synchronized bursts once synchronization has been achieved. As mentioned above the firing frequency increases during development. It is likely that this is due in part to the increase in network connectivity as the cells mature and make more synapses. These effects could be incorporated into the model by starting with a small initial value of the connectivity distance and gradually increasing its size as the network develops. Including a small delay between the firing of different cells would also allow the effect of network connectivity on the propagation velocity to be examined. At present the propagation velocity is not simulated as the firing of one cell instantaneously brings other cells up to firing.

Finally the current model does not investigate the role of synchronized firing on the survival rate of the cells. The results of Voigt et al. (1997) showed that cells which are inactive, or active but not participating in synchronous firing, are less likely to to survive than cells which display synchronized activity. It is not clear whether cells which fail to survive develop abnormal processes, or whether synchronized firing allows concurrent pre- and post- synaptic mechanisms to be established. Such a model could include Hebbian-like strengthening of the connections of cells which were simultaneously active. The network connectivity would then be altered by the pattern of activity received by each cell. It is likely that this would favour the survival of those cells which participate in synchronized activity.

Bibliography

Abbott, L., & Vanvreeswijk, C. (1993). Asynchronous states in networks of pulse-coupled oscillators. *Physical Review E, 48*, 1483–1490.

Al-Mohanna, F., Cave, J., & Bolsover, S. (1992). A narrow window of intracellular calcium concentration is optimal for neurite outgrowth in rat sensory neurones. *Developmental Brain Research, 70*, 287–290.

Albinet, G., & Pelce, P. (1996). Computer simulation of neurite outgrowth. *Europhysics letters, 33*, 569–574.

Audesirk, G., Cabell, L., & Kern, M. (1997). Modulation of neurite branching by protein phosphorylation in cultured rat hippocampal neurons. *Developmental Brain Research, 102*, 247–260.

Baas, P., & Black, M. (1990). Individual microtubules in the axon consist of domains that differ in both composition and stability. *Journal of Cell Biology, 111*, 495–509.

Bamburg, J., Bray, D., & Chapman, K. (1986). Assembly of microtubules at the tips of growing axons. *Nature, 321*, 788–790.

Bandtlow, C., Zachleder, T., & Schwab, M. (1990). Oligodendrocytes arrest neurite growth by contact inhibition. *The Journal of Neuroscience, 10*, 3837–3848.

Barry, J., & Ribchester, R. (1995). Persistent polyneuronal innervation in partially denervated rat muscle after reinnervation and recovery from prolonged nerve- conduction block. *Journal of Neuroscience, 15*, 6327–6339.

Bastmeyer, M., & Stuermer, C. (1993). Behavior of fish retinal growth cones encountering chick caudal tectal membranes: a time-lapse study on growth cone collapse. *The Journal of Neurobiology, 24*, 37–50.

Bayley, P., Schilstra, M., & Martin, S. (1990). Microtubule dynamic instability: numerical simulation of microtubule transition properties using a Lateral Cap model. *Journal of Cell Science, 95*, 33–48.

Bedlack, R., Wei, M.-d., Fox, S., Gross, E., & Loew, L. (1994). Distinct electric potentials in soma and neurite membranes. *Neuron, 13*, 1187–1193.

Bedlack, R., Wei, M.-d., & Loew, L. (1992). Localized Membrane Depolarizations and Localized Calcium Influx during Electric Field-Guided Neurite Growth. *Neuron, 9*, 393–403.

Belmont, L., Hyman, A., Sawin, K., & Mitchison, T. (1990). Real time visualisation of cell cycle-dependent changes in microtubule dynamics in cytoplasmic extracts. *Cell, 62*, 579–589.

Biernat, J., Gustke, N., Drewes, G., Mandelkow, E.-M., & Mandelkow, E. (1993). Phosphorylation of Ser262 strongly reduces binding of tau to microtubules: distinction between PHF-like immunoreactivity and microtubule binding. *Neuron, 11*, 153–163.

Bjorklund, A., Lundvall, O., Isacson, O., & Brundin, P. (1987). Mechanisms of action of intracerebral neural implants: studies on nigral and striatal grafts to the lesioned striatum. *Trends in Neurosciences, 10*, 509–516.

Black, M., Slaughter, T., & Fischer, I. (1994). Microtubule-associated Protein 1b (MAP1b) is Concentrated in the Distal Region of Growing Axons. *The Journal of Neuroscience, 14*, 857–870.

Black, M., Slaughter, T., Moshiach, S., Obrocka, M., & Fischer, I. (1996). Tau is Enriched on Dynamic Microtubules in the Distal Region of Growing Axons. *The Journal of Neuroscience, 16*, 3601–3619.

Bogdan, M., Babanine, A., Kaniecki, J., & Rosentiel, W. (1995). Nerve Signal Processing using Articial Neural Nets. In Paton, R. (Ed.), *Information Processing in Cells and Tissues (IPCAT-95)*, No. 1 in IPCAT, pp. 55–68 The Univesity of Liverpool.

Bray, D. (1973). Branching Patterns of Individual Sympathetic Neurons in Culture. *Journal of Cell Biology, 56*, 702–712.

Bray, D. (1984). Axonal Growth in Response to Experimentally Applied Mechanical Tension. *Developmental Biology, 102*, 379–389.

Bray, D. (1988). Cortical Flow in Animal Cells. *Science, 239*, 883–888.

Broadie, K., Sink, H., VanVactor, D., & Fambrough, D. (1993). From Growth Cone to synapse: the life history of the RP3 motor neuron. *Development 1993 Supplement*, 227–238.

Brown, M., Hopkins, W., & Keynes, R. (1991). *Essentials of neural development.* Cambridge University Press.

Brugg, B., & Matus, A. (1991). Phosphorylation determines the binding of microtubule-associated protein 2 (MAP2) to microtubules in living cells. *The Journal of Cell Biology, 114*, 735–743.

Burke, R., Marks, W., & Ulfhake, B. (1992). A parsimonious description of motoneuron dendritic morphology using computer simulation. *The Journal of Neuroscience., 12,* 2403–2416.

Buxbaum, R., & Heidemann, S. (1988). A Thermodynamic Model for Force Integration and Microtubule Assembly During Axonal Elongation. *The Journal of Theoretical Biology, 134,* 379–390.

Buxbaum, R., & Heidemann, S. (1992). An Absolute Rate Theory Model For Tension Control of Axonal Elongation. *The Journal of Theoretical Biology, 155,* 409–426.

Cajal, R. (1893). La retine des vertebres. *La Cellule, 9,* 119–258.

Caroni, P., & Schwab, M. (1988). Antibody against myelin–associated inhibitor of neurite growth neutralizes non–permissive substrate properties of CNS white matter. *Neuron, 1,* 85–96.

Chen, D., Jhaveri, S., & Schneider, G. (1995). Intrinsic changes in developing retinal neurons result in regenerative failure of their axons. *Proceedings of the National Academy of Sciences. USA, 92,* 7287–7291.

Chen, J., Kanai, Y., Cowan, N., & Hirokawa, N. (1992). Projection domains of MAP2 and tau determine spacings between microtubules in dendrites and axons. *Nature, 360,* 674–677.

Chen, Y.-D., & Hill, T. (1985). Theoretical treatment of microtubules disappearing in solution. *Proceedings of the National Academy of Sciences. USA, 82,* 4127–4131.

Cleveland, D., Pittenger, M., & Lopata, M. (1983). Autoregulatory control of expression of alpha-tubulin and beta-tubulin. *Journal of Submicroscopic Cytology, 15,* 353–358.

Cohan, C., Connor, J., & Kater, S. (1987). Electrically and Chemically Mediated Increases in Intracellular Calcium in Neuronal Growth Cones. *The Journal of Neuroscience, 7*, 3588–3599.

Cohen, S. (1960). Purification of a nerve-growth promoting protein from the mouse salivary gland and its antiserum. *Proceedings of the National Academy of Science, USA, 46*, 302–311.

Colamarino, S., & Tessier-Lavigne, M. (1995). The axonal chemoattractant netrin-1 is also a chemorepellent for trochlear motor axons. *Cell, 81*, 621–629.

Cornell-Bell, A., & Thomas, P. (1992). Ca2+ and filopodial responses to glutamate in cultured astrocytes and neurons. *Canadian Journal of Physiological Pharmacology, 70*, S206–S218.

Davenport, R., Dou, P., Mills, R., & Kater, S. (1996). Distinct Calcium Signalling within Neuronal Growth Cones and Filopodia. *Journal of Neurobiology, 31*, 1–15.

Davenport, R., Dou, P., Rehder, V., & Kater, S. (1993). A sensory role for neuronal growth cone filopodia. *Nature, 361*, 721–724.

Davenport, R., & Kater, S. (1992). Local Increases in Intracellular Calcium Elicit Local Filopodial Responses in Helisoma Neuronal Growth Cones. *Neuron, 9*, 405–416.

Dennerll, T., Joshi, H., Steel, V., Buxbaum, R., & Heidemann, S. (1988). Tension and Compression in the Cytoskeleton of PC-12 Neurites II: Quantitative Measurements. *The Journal of Cell Biology, 107*, 665–674.

Dichter, M. (1978). Rat cortical neurons in cell culture: culture-methods, cell morphology, electrophysiology, and synapse formation. *Brain Research, 149*, 272–293.

Diez-Guerra, F., & Avila, J. (1993). MAP2 phosphorylation parallels dendrite arborization in hippocampal neurones in culture. *NeuroReport, 4*, 412–419.

Dityatev, A., Chmykhova, N., Studer, L., Karamian, O., Kozhanov, V., & Clamann, H. (1995). Comparison of the Topology and Growth Rules of Motoneuronal Dendrites. *The Journal of Comparative Neurology, 363*, 505–516.

Dotti, C., Sullivan, C., & Banker, G. (1988). The establishment of polarity by hippocampal neurons in culture. *Journal of Neuroscience, 8*, 1454–1468.

Edelstein-Keshet, L. (1988). *Mathematical Models in Biology*. Birkhauser Mathematics Series.

Engel, A., Konig, P., Kreiter, A., Shillen, T., & Singer, W. (1992). Temporal coding in the visual cortex: new vistas on integration in the nervous system. *Trends in the Neurosciences, 15*, 218–226.

Forscher, P. (1988). Calcium and polyphosphoinositide control of cytoskeletal dynamics. *Trends in Neurosciences, 12*(11), 468–479.

Forscher, P., & Smith, S. (1988). Actions of Cytochalasins on the Organization of Actin Filaments and Microtubules in a Neuronal Growth Cone. *Journal of Cell Biology, 107*, 1505–1516.

Friedrich, P., & Aszodi, A. (1991). MAP2: a sensitive cross-linker and adjustable spacer in dendritic architecture. *FEBS Letters, 295*, 5–9.

Fuller, R. (1961). Tensegrity. *Portfolio and Artnews Annual, 4*, 112–127.

Goodman, C., & Shatz, C. (1992). Developmental Mechanisms That Generate Precise Patterns of Neuronal Connectivity. *Cell (Supplement), 72*, 77–98.

Goodwin, B., & Trainor, L. (1985). Tip and Whorl Morphogenesis in Acetabularia by Calcium-Regulated Strain Fields. *Journal of Theoretical Biology, 117*, 79–106.

Gordon-Weeks, P. (1989). Growth at the growth cone. *Trends in Neurosciences, 12*, 238–240.

Graham, B., Hely, T., & van Ooyen, A. (1998). An internal signalling model of the dendritic branching process. *European Journal of Neuroscience, 10S*, 274.

Graziadei, P., & Monti-Graziadei, G. (1979). Neurogenesis and neuron regeneration in the olfactory system of mammals. I. Morphological aspects of differentiation and structural organization of the olfactory sensory neurons. *Journal of Neurocytology, 8*, 1–18.

Gundersen, R., & Barrett, J. (1979). Neuronal chemotaxis: chick dorsal root axons turn toward high concentrations of nerve growth factor. *Science, 206*, 1079–1080.

Hall, G., Lee, V., & Kosik, K. (1991). Microtubule destabilization and neurofilament phosphorylation precede dendritic sprouting after close axotomy of lamprey central neurons. *Proceedings of the National Academy of Sciences USA, 88*, 5016–5020.

Hansel, D. Mato, G., & Meunier, C. (1995). Synchrony in excitatory neural networks. *Physical Review Letters, 74*, 1570–1573.

Harrison, L., Graham, K., & Lakowski, B. (1988). Calcium localization durin Acetabularia whorl formation: evidence supporting a two-stage hierarchical mechanism. *Development, 104*, 255–262.

Harrison, L., & Hillier, N. (1985). Quantitative Control of Acetabularia Morphogenesis by Extracellular Calcium: A Test of Kinetic Theory. *Journal of Theoretical Biology, 114*, 177–192.

Harrison, R. (1935). On the origin and development of the nervous system studied by the methods of experimental embryology. *Proceedings of the Royal Society (London) B, 118*, 155–196.

Hentschel, H. (1994). Instabilities in Cellular Dendritic Morphogenesis. *Physical Review Letters, 73*, 3592–3595.

Hentschel, H., & Fine, A. (1996). Diffusion-regulated control of cellular dendritic morphogenesis. *Proceedings of the National Academy of Sciences USA, 263*, 1–8.

Hill, T. (1984). Introductory analysis of the GTP-cap phase-change kinetics at the end of a microtubule. *Proceedings of the National Academy of Sciences USA, 81*, 6728–6732.

Hill, T., & Chen, Y.-D. (1984). Phase changes at the end of a microtubule with a GTP cap. *Proceedings of the National Academy of Sciences USA, 81*, 5772–5776.

His, W. (1874). *"Unsere Korperform und das physiologische Problem ihrer Entstehung,Leipzig."*. Cited in Thompson,D.W. (1963) "Growth and Form," Vol. I, pp 111,114. Cambridge University Press,London.

Holy, T., & Leibler, S. (1994). Dynamic Instability of microtubules as an efficient way to search in space. *Proceedings of the National Academy of Sciences USA, 91*, 5682–5685.

Hotary, K., & Robinson, K. (1990). Endogenous electric currents and the resultant voltage gradients in the chick embryo. *Developmental Biology, 140*, 149–160.

Hotary, K., & Robinson, K. (1994). Endogenous electric currents and voltage gradients in Xenopus neurons and the consequences of their disruption. *Developmental Biology, 166*, 1789–1800.

Hughes, A. (1953). The growth of embryonic neurites: a study on cultures of chick neural tissues. *Journal of Anatomy, 87*, 150–162.

Ichikawa, M., Muramoto, K., Kobayashi, K., Kawahara, M., & Kuroda, Y. (1993). Formation and maturation of synapses in primary cultures of rat cerebral cortical cells: an electron microscopic study. *The Journal of Neuroscience Research, 16*, 95–103.

Ito, M. (1984). *The Cerebellum and Neural Control*. Raven Press, New York.

Iwashita, Y., Kawaguchi, S., & Murata, M. (1984). Restoration of function by replacement of spinal cord segments in the rat. *Nature, 367*, 167–170.

Joshi, H., Chu, D., Buxbaum, R., & Heidemann, S. (1985). Tension and Compression in the Cytoskeleton of PC-12 Neurites. *The Journal of Cell Biology, 102*, 1400–1411.

Kamioka, H., Maeda, E., Jimbo, Y., Robinson, H., & Kawana, A. (1996). Spontaneous periodic synchronized bursting during formation of mature patterns of connections in cortical cultures. *Neuroscience Letters, 206*, 109–112.

Kandel, E., Schwartz, J., & Jessell, T. (1991). *Principles of Neural Science: Third Edition*. Appleton and Lange, Prentice-Hall.

Kater, S., Mattson, M., Cohan, C., & Connor, J. (1988). Calcium and the regulation of the neuronal growth cone. *Trends in the Neurosciences, 11*, 315–321.

Kennedy, T., Serafini, T., De la Torre, J., & Tessier-Lavigne, M. (1994). Netrins are diffusible chemotropic factors for commissural axons in the embryonic spinal cord. *Cell, 78*, 425–435.

Keynes, R., & Cook, G. (1992). Repellent Cues in Axon Guidance. *Current Opinions in Neurobiology, 2,* 55–59.

Kirschner, M., & Mitchison, T. (1986). Beyond Self Assembly: From Microtubules to Morphogenesis. *Cell, 45,* 329–342.

Kliemann, W. (1987). Stochastic dynamic model for the characterization of the geometrical structure of dendritic processes. *Bulletin of Mathematical Biology., 49,* 135–152.

Knight, B. (1972). Dynamics of Encoding in a Population of Neurons. *Journal of General Physiology., 59,* 734–766.

Konig, P., & Schillen, T. (1991). Stimulus-dependent assembly formation of oscillatory responses: I. Synchronization. *Neural Computation, 3,* 155–161.

Kotani, S., Nishida, E., Kumagai, H., & Sakai, H. (1985). Calmodulin inhibits interaction of actin with MAP2 and tau, two major microtubule-associated proteins. *The Journal of Biological Chemistry, 260,* 10779–10783.

Kudo, Y., & Ogura, A. (1986). Glutamate-induced increase in intracellular Ca2+ concentration in isolated hippocampal neurones. *British Journal of Pharmacology, 89,* 191–198.

Larkman, A. (1991). Dendritic morphology of pyramidal neurones of the visual cortex of the rat: I. Branching patterns. . *Journal of Comparative Neurology, 306,* 307–319.

Lefcort, F., & Bentley, D. (1987). Pathfinding by pioneer neurons in isolated opened and mesoderm-free limb buds of embryonic grasshopper. *Developmental Biology, 119,* 446–480.

Lein, P., Banker, G., & Higgins, D. (1992). Laminin selectively enhances axonal growth and accelerates the development of polarity by hippocampal neurons in culture. *Developmental Brain Research, 69*, 191–197.

Letourneau, P. (1983). Differences in the organization of actin in the growth cones compared with the neurites of cultured neurons from chick embryos. *Journal of Cell Biology, 97*, 963–973.

Letourneau, P. (1986). Branching of sensory and sympathetic neurites in vitro is inhibited by treatment with taxol. *The Journal of Neuroscience, 6*, 1912–1917.

Letourneau, P., Madsen, M., Palm, S., & Furcht, L. (1988). Immunoreactivity for laminin in the developing ventral longitudinal pathway of the brain. *Developmental Biology, 125*, 135–144.

Letourneau, P., Shattuck, T., & Ressler, A. (1987). "Pull" and "Push" in Neurite Elongation: Observations on the Effects of Different Concentrations of Cytochalasin B and Taxol. *Cell Motility and the Cytoskeleton, 8*, 193–209.

Lewin, G., & Barde, Y.-A. (1996). Physiology of the Neurotrophins. *Annual Review of Neuroscience, 19*, 289–317.

Lewis, S., Ivanov, I., Lee, G., & Cowan, N. (1989). Organization of microtubules in dendrites and axons is determined by a short hydrophobic zipper in microtubule-associated proteins MAP2 and tau. *Nature, 342*, 498–505.

Li, G.-H., & Qin, C.-D. (1996). A Model for Neurite Growth and Neuronal Morphogenesis. *Mathematical Biosciences, 132*, 97–110.

Li, G.-H., Qin, C.-D., & Wang, Z.-S. (1992). Neurite Branching Pattern Formation: Modeling and Computer Simulation. *Journal of Theoretical Biology, 157*, 463–486.

Li, G.-H., Qin, C.-D., & Wang, Z.-S. (1995). Computer Model of Growth Cone Behavior and Neuronal Morphogenesis. *Journal of Theoretical Biology, 174,* 381–389.

Lin, C.-H., & Forscher, P. (1995). Growth Cone Advance is Inversely Proportional to Retrograde F-Actin Flow. *Neuron, 14,* 763–771.

Lindvall, O. (1994). Clinical application of neuronal grafts in Parkinson's disease. *The Journal of Neurology,Supplement, 242*(1), S54–S56.

Maccioni, R., & Cambiazo, V. (1995). Role of Microtubule-Associated Proteins in the Control of Microtubule Assembly. *Physiological Reviews, 75,* 835–864.

Maeda, E., Robinson, H., & Kawana, A. (1995). The Mechanisms of Generation and Propagation of Synchronized Bursting in Developing Networks of Cortical Neurons. *The Journal of Neuroscience, 15,* 6834–6845.

Marsh, L., & Letourneau, P. (1984). Growth of neurites without filopodial or lamellipodial activity in the presence of Cytochalasin B. *Journal of Cell Biology, 99,* 180–187.

Martenson, C., Stone, K., Reedy, M., & Sheetz, M. (1993). Fast axonal transport is required for growth cone advance. *Nature, 366,* 66–69.

Mattson, M., & Kater, S. (1987). Calcium Regulation of Neurite Elongation and Growth Cone Motility. *The Journal of Neuroscience, 7,* 4034–4043.

Matus, A., Bernhardt, R., Bodmer, R., & Alaimo, D. (1986). Microtubule-associated protein 2 and tubulin are differently distributed in the dendrites of developing neurons. *Neuroscience, 17,* 371–389.

McCaig, C., & Rajnicek, A. (1991). Electrical Fields, Nerve Growth and Nerve Regeneration. *Experimental Physiology, 76,* 473–494.

Meinhardt, H., & Klinger, M. (1987a). A model for pattern formation on the shells of molluscs. *Journal of Theoretical Biology, 126*, 63–89.

Meinhardt, H., & Klinger, M. (1987b). Pattern formation by coupled oscillations: The pigmentation patterns on the shells of molluscs. *Lecture Notes in Biomathematics, 71*, 184–198.

Meister, M., Wong, R., Baylor, D., & Shatz, C. (1991). Synchronous Bursts of Action Potentials in Ganglion Cells of the Developing Mammalian Retina. *Science, 252*, 939–943.

Mirollo, R., & Strogatz, S. (1990). Synchronization of Pulse-Coupled Biological Oscillators. *SIAM Journal of Applied Mathematics, 50*, 1645–1662.

Mitchison, T., & Kirschner, M. (1984a). Dynamic instability of microtubule growth. *Nature, 312*, 237–242.

Mitchison, T., & Kirschner, M. (1984b). Microtubule assembly nucleated by isolated centrosomes. *Nature, 312*, 232–237.

Mitchison, T., & Kirschner, M. (1987). Some thoughts on the partitioning of tubulin between monomer and polymer under conditions of dynamic instability. *Cell Biophysics, 11*, 35–55.

Mitchison, T., & Kirschner, M. (1988). Cytoskeletal Dynamics and Nerve Growth. *Neuron, 1*, 761–772.

Murphy, T., Blatter, L., Wier, W., & Baraban, J. (1992). Spontaneous synchronous synaptic calcium transients in cultured cortical neurons. *Journal of Neuroscience., 12*, 4834–4845.

Norbeck, B., & Denburg, J. (1992). Molecular gradients along the proximodistal axis of embryonic insect legs: possible guidance cues of pioneer axon growth. *Development, 116*, 467–479.

O'Connor, T., & Bentley, D. (1993). Accumulation of Actin in Subsets of Pioneer Growth Cone Filopodia in Response to Neural and Epithelial Guidance Cues In Situ. *The Journal of Cell Biology, 123*(4), 935–948.

O'Connor, T., Duerr, J., & Bentley, D. (1990). Pioneer growth cone steering decisions mediated by single filopodia contacts in situ. *The Journal of Neuroscience, 10*, 3935–3946.

Odde, D., & Buettner, H. (1995). Time series characterization of simulated microtubule dynamics in the nerve growth cone. *Annals of Biomedical Engineering, 23*, 268–286.

Ogura, A., Iigima, T., Amano, T., & Kudo, Y. (1987). Optical monitoring of excitatory synaptic activity between cultured hippocampal neurons by a multi-site Ca2+ fluometry. *Neuroscience Letters, 78*, 69–74.

O'Leary, D., & Terashima, T. (1988). Cortical axons branch to multiple subcortical targets by interstitial axon budding; implications for target recognition and "waiting periods". *Neuron, 1*, 901–910.

Pelce, P. (1993). Origin of Cellular Ionic Currents. *Physical Review Letters, 71*, 1107–1110.

Peskin, C. (1975). *Mathematical Aspects of Heart Physiology*. Courant Insititute of Mathematical Sciences, New York University, New York.

Pini, A. (1994). Growth cones say no. *Current Biology, 4*, 131–133.

Press, W., Teukolsky, S., Vetterling, W., & Flannery, A. (1992). *Numerical Recipes in C: The art of scientific computing*. Cambridge University Press.

Prusinkiewicz, P. (1993). Modeling and visualization of biological structures. In *Proceedings of Graphics Interface '93*, pp. 128–137.

Prusinkiewicz, P. (1994). Visual Models of Morphogenesis. *Artificial Life, 1,* 67–74.

Pryer, N., Walker, R., Skeen, V., Bourns, B., Sobeiro, M., & Salmon, E. (1992). Brain microtubule-associated proteins modulate microtubule dynamic instability in vitro. *The Journal of Cell Science, 103,* 965–976.

Rehder, V., & Kater, S. (1996). Filopodia on neuronal growth cones: multifunctional structures with sensory and motor capabilities. *Seminars in the Neurosciences, 8,* 81–88.

Reinsch, S., Mitchison, T., & Kirschner, M. (1991). Microtubule polymer assembly and transport during axonal elongation. *Journal of Cell Biology, 115,* 365–379.

Richardson, P., McGuiness, U., & Aguayo, A. (1980). Axons from CNS neurones regenerate into PNS grafts. *Nature, 284,* 264–265.

Rieder, C., & Alexander, S. (1990). Kinetochores are transported poleward along a single astral microtubule during chromosome attachment to the spindle in newt lung- cells. *Journal of Cell Biology, 110,* 81–95.

Rinnerthaler, G., Geiger, B., & J., S. (1988). Contact formation during fibroblast locomotion: involvement of membrane ruffles and microtubules. *Journal of Cell Biology, 106,* 747–760.

Robinson, H., Kawahara, M., Jimbo, Y., Torimitsu, K., Kuroda, Y., & Kawana, A. (1993). Periodic synchronized bursting and intracellular calcium transients elicited by low magnesium in cultured cortical neurons. *Journal of Neurophysiology, 70,* 1606–1616.

Sabry, J., O'Connor, T., Evans, L., Toroian-Raymond, A., Kirschner, M., & Bentley, D. (1991). Microtubule Behavior during Guidance of Pioneer Neuron Growth Cones in situ. *Journal of Cell Biology, 115,* 381–395.

Safford, R., & Bassingthwaite, J. (1977). Calcium diffusion in transient and steady states in muscle. *Biophysical Journal, 20,* 113.

Scheetz, A., Prusky, G., & Constantine-Paton, M. (1996). Chronic NMDA Receptor Antagonism Duyring Retinotopic Map Formation Depresses CaM Kinase II Differentiation in Rat Superior Colliculus. *European Journal of Neuroscience, 8,* 1322–1328.

Schilling, K., Dickinson, M., Connor, J., & Morgan, J. (1991). Electrical Activity in Cerebellar Cultures Determines Purkinje Cell Dendritic Growth Patterns. *Neuron, 7,* 891–902.

Scholz, W., Baitinger, C., Schulman, H., & Kelly, P. (1988). Developmental-changes in Ca-2+/calmodulin-dependent protein kinase-II in cultures of hippocampal pyramidal neurons and astrocytes. *The Journal of Neuroscience, 8,* 1039–1051.

Selden, S., & Pollard, T. (1983). Phosphorylation of microtubule associated proteins regulate their interaction with actin filaments. *Journal of Biological Chemistry, 258,* 7064–7071.

Shatz, C. (1990). Impulse activity and the patterning of connections during CNS development. *Neuron, 5,* 745–756.

Shi, R., & Borgens, R. (1995). Three-dimensional gradients of voltage during development of the nervous system as invisible coordinates for the establishment of embryonic pattern. *Developmental Dynamics, 202,* 101–114.

Son, Y., & Thompson, W. (1995). Schwann-cell processes guide regeneration of peripheral axons. *Neuron, 14,* 125–132.

Song, H.-j., Ming, G.-l., & Poo, M.-m. (1997). cAMP-induced switching in turning direction of nerve growth cones.. *Nature, 388,* 275–279.

Stevens, C., & Tsujimoto, T. (1995). Estimates for the pool size of releasable quanta at a single central synapse and for the time required to fill the pool. *Proceedings of the National Academy of Sciences, USA, 92*, 846–849.

Stewart, R., Erskine, L., & McCaig, C. (1995). Calcium Channel Subtypes and Intracellular Calcium Stores Modulate Electric Field-Stimulated and -Oriented Nerve Growth. *Developmental Biology, 171*, 340–351.

Suter, D., Errante, L., Belotserkovsky, V., & Forscher, P. (1998). The Ig superfamily cell adhesion molecule, apCAM, mediates growth cone steering by substrate-cytoskeletal coupling. *Journal of Cell Biology, 141*, 227–240.

Takemura, R., Okabe, S., Umeyama, T., Kania, Y., Cowan, N., & Hirokawa, N. (1990). Increased microtubule stability and alpha tubulin acetylation in cells transfected with microtubule-associated proteins MAP1B,MAP2 or tau. *Journal of Cell Science, 103*, 953–964.

Tamori, Y. (1993). Theory of dendritic morphology. *Physical Review E, 48*, 3124–3129.

Tanaka, E., & Kirschner, M. (1991). Microtubule Behaviour in the Growth Cones of Living Neurons during Axon Elongation. *Journal of Cell Biology, 115*, 345–363.

Tanaka, E., & Sabry, J. (1995). Making the Connection:Cytoskeletal Rearrangements during Growth Cone Guidance. *Cell, 83*, 171–176.

Thompson.W.J. (1986). Changes in the innervation of mammalian skeletal muscle fibres during postnatal development. *Trends in Neuroscience., 9*, 25–28.

Tsodyks, M., Mitkovm, I., & Sompolinsky, H. (1993). Pattern of synchrony in inhomogenous networks of oscillators with pulse interactions. *Physical Review Letters, 71*, 1280–1283.

Turing, A. (1952). The chemical basis for morphogenesis. *Philosophical Transactions of the Royal Society of London, 237*, 37–72.

Turrigiano, G., Leslie, K., Desai, N., Rutherford, L., & Nelson, S. (1998). Activity-dependent scaling of quantal amplitude in neocortical neurons. *Nature, 391*, 892–896.

van der Loos, H. (1965). The "improperly" oriented pyramidal cell in the cerebral cortex and its possible bearing on problems of neuronal growth and cell orientation. *Bulletin of Johns Hopkins Hospital, 117*, 228–250.

van Pelt, J., Dityatev, A., & Uylings, H. (1997). Natural Variability in the Number of Dendritic Segments: Model-Based Inferences About Branching During Neurite Outgrowth. *The Journal of Comparative Neurology, 387*, 325–340.

van Pelt, J., & Uylings, H. (1997). Mathematical modeling of dendritic branching patterns. In Poznanski, R. (Ed.), *Mathematical modeling in the neurosciences: from ionic channels to neural networks.* Gordon and Breach.

van Pelt, J., Uylings, H., Verwer, R., & Pentney, R.J.and Woldenberg, M. (1992). Tree asymmetry - a sensitive and practical measure of binary topological trees. *Bulletin of Mathematical Biology, 54*, 759–784.

van Pelt, J., & Verwer, R. (1986). Topological properties of binary trees grown with order-dependent branching probabilities. *Bulletin of Mathematical Biology, 48*, 197–211.

van Veen, M. (1993). *Dynamic Mechanisms of Neuronal Outgrowth.* Ph.D. thesis, Free University, Amsterdam.

van Veen, M., & van Pelt, J. (1992). A Model for Outgrowth of Branching Neurites. *Journal of Theoretical Biology, 159*, 1–23.

Viereck, C., Tucker, R., & Matus, A. (1989). The Adult Rat Olfactory System Expresses Microtubule-Associated Proteins Found in the Developing Brain. *The Journal of Neuroscience, 9*, 3547–3557.

Voigt, T., Baier, H., & de Lima, A. D. (1997). Synchronization of Neuronal Activity Promotes Survival of Individual Rat Neocortical Neurons in Early Development. *European Journal of Neuroscience, 9*, 990–999.

Walker, R., O'Brien, E., Pryer, N., Soboeiro, M., Voter, W., Erickson, H., & Salmon, E. (1988). Dynamic instability of individual microtubules analyzed by video light-microscopy - rate constants and transition frequencies. *Journal of Cell Biology, 107*, 1437–1448.

Wang, D. (1995). Emergent Synchrony in Locally Coupled Neural Oscillators. *IEEE Transactions in Neural Networks, 6*, 941–948.

Weiss, P. (1941). Nerve patterns. The mechanics of nerve growth. *Third Growth Symposium, 5*, 153–203.

Wessels, N., & Nuttall, R. (1978). Normal branching, induced branching, and steering of cultured parasympathetic motor neurons. *Experimental Cell Research, 115*, 111–122.

Woolford, T., & Toriumi, D. (1995). The enhancement of nerve regeneration using growth factors: A brief review. *Journal of Long–Term Effects of Medical Implants., 5*(1), 19–26.

Yamada, K., Spooner, B., & Wessells, N. (1970). Axon growth: roles of microfilaments and microtubules. *Proceedings of the National Academy of Science, 66*, 1206–1212.

Yamamoto, H., Fukunaga, K., Tanaka, E., & Miyamoto, E. (1983). Ca2+ and calmodulin-dependent phosphorylation of microtubule-associated pro-

tein 2 and TAU factor, and inhibition of microtubule assembly. *The Journal of Neurochemistry, 41,* 1119–1125.

Yamamoto, H., Saitoh, Y., Fukunaga, K., Nishimura, H., & Miyamoto, E. (1985). Dephosphorylation of microtubule proteins by brain protein phosphatases 1 and 2A, and its effect on microtubule assembly. *The Journal of Neurochemistry, 50,* 1614–1623.

Yamauchi, T., & Fujisawa, H. (1988). Regulation of the interaction of actin filaments with microtubule-associated protein 2 by calmodulin-dependent protein kinase II. *Biochimica et Biophysica Acta, 968,* 77–85.

Young, D. (1984). A local activator-inhibitor model of vertebrate skin patterns. *Mathematical Biosciences, 72,* 51–54.

Yuste, R., Peinado, A., & Katz, L. (1992). Neuronal Domains in Developing Neocortex. *Science, 257,* 665–669.

Zheng, J., Buxbaum, R., & Heidemann, S. (1993). Investigation of microtubule assembly and organization accompanying tension-induced neurite initiation. *Journal of Cell Science, 104,* 1239–1250.

Zheng, J., Wan, J., & Poo, M. (1996). Essential role of Filopodia in Chemotropic Turning of Nerve Growth Cone Induced by a Glutamate Gradient. *The Journal of Neuroscience, 16,* 11140–1149.

Zimprich, F., & Bolsover, S. (1996). Calcium channels in Neuroblastoma Cell Growth Cones. *European Journal of Neuroscience, 8,* 467–475.

Zot, H., Doberstein, S., & Pollard, T. (1992). Myosin-I Moves Actin Filaments on a Phospholipid Substrate: Implications for Membrane Targeting. *Journal of Cell Biology, 116,* 367–376.

Appendix A

Mathematical reduction of branching model equations

The four differential equations in the branching model describe the time rate of change of calcium and $MAP2_{u,b,p}$. To simplify the analysis both $MAP2_b$ and $MAP2_p$ are taken to be at equilibrium ($\delta/\delta t = 0$). They can then be written directly in terms of $MAP2_u$ and calcium. This reduction is carried out below for the linear model equations 7.6 and 7.7 in Chapter 7. Exactly the same process can be used to reduce the non-linear model equations 7.16 and 7.17

A.1 Reduction of dynamic model parameters

The differential equations describing $MAP2_u$ and $MAP2_b$ in the linear model are given by Equations A.1 and A.2 below:

$$\frac{\partial MAP2_b}{\partial t} = c_1 MAP2_u + c_4 MAP2_p - MAP2_b\,(c_2 + c_3\,Ca - \delta_b) = 0 \quad \text{(A.1)}$$

$$\frac{\partial MAP2_p}{\partial t} = c_3\,Ca\;MAP2_b - MAP2_p\,(c_4 + \delta_p) = 0 \quad \text{(A.2)}$$

Rearranging equation A.2 gives $MAP2_p$ in terms of $MAP2_b$:

$$MAP2_p\,(c_4 + \delta_p) = c_3\,Ca\;MAP2_b \quad \text{(A.3)}$$

$$MAP2_p = \frac{c_3\,Ca}{c_4 + \delta_p} MAP2_b \quad \text{(A.4)}$$

The form of $MAP2_p$ in equation A.4 can then be inserted into A.1 to get $MAP2_b$ as a function of $MAP2_u$.

$$c_1 MAP2_u = MAP2_b\,(c_2 + c_3 Ca - c_4(\frac{c_3\,Ca}{c_4 + \delta_p}) + \delta_b) \quad \text{(A.5)}$$

$$MAP2_b = \frac{c_1 MAP2_u}{(c_2 + c_3 Ca - c_4(\frac{c_3\,Ca}{c_4+\delta_p}) + \delta_b)} \quad \text{(A.6)}$$

$MAP2_p$ can also be written as a function of $MAP2_u$ and calcium by combining equations A.4 and A.6 as follows:

$$MAP2_p = \frac{c_3\,Ca}{c_4 + \delta_p} MAP2_b = \frac{c_3\,Ca}{(c_4 + \delta_p)} \frac{c_1 MAP2_u}{(c_2 + c_3 Ca - c_4(\frac{c_3\,Ca}{c_4+\delta_p}) + \delta_b)} \quad \text{(A.7)}$$

Equations A.6 and A.7 allow the concentration of $MAP2_b$ and $MAP2_p$ to be calculated in terms of $MAP2_u$ and Ca. Exactly the same process can be used to rearrange $MAP2_b$ and $MAP2_p$ in the non-linear model equations 7.16 and 7.17.